Doctoral Dissertation, 2017

Theoretical study on ordering of polarity and oscillation in cell populations

OCHANOMIZU UNIVERSITY

Advanced Science,

Graduate School of Humanities and Sciences

SUGIMURA Kaori

March, 2018

Contents

Abstract

Polarity and phase ordering are greatly important in biology. The former is essential, e.g., for alignment of hair follicles and oriented cell division. The latter is known as synchronization, which is required, e.g., for normal operation of the heart and circadian rhythms. In this thesis, the ordering dynamics of cellular polarity and oscillation phase is elucidated.

In Chapter 1, polarity and phase ordering and some mathematical models of ordering are introduced.

The first and second parts of this thesis deal with the polarity alignment process (Chapters 2 – 4) and the phase ordering process (Chapters 5 – 7), respectively.

In Chapter 2, first, the planar cell polarity (PCP) is explained. PCP refers to the coordinated alignment of cell polarity across a planar tissue, and many biological experiments have been performed on PCP in the wing epithelium of *Drosophila*. The present study is based on those experimental results. The previous mathematical models of PCP and general models describing ordering of spins and oscillators are introduced.

In Chapter 3, a reaction–diffusion model of cellular polarity alignment is constructed. Nonetheless, this model is costly for numerical analysis when many cells are considered. Therefore, in the second half of Chapter 3, a reduced model using the phase reduction theory for systems with a spatially translational mode is derived. The derived phase model is drastically simpler and easier to analyze than the reaction–diffusion model, yet it is a reasonable approximation. It contains the terms representing geometric information, such as cell shape and relative position of adjacent cells in addition to the terms similar to ferromagnetic spin models. In contrast to previously proposed phenomenological models, these terms are derived directly from the reaction–diffusion model.

In Chapter 4, the newly derived phase model is analyzed. As a result, it becomes clear that shapes of cells and anisotropy of a coupling strength distribution affect the global orientation of polarity. In fact, when the distribution of coupling strengths is uniform, the polarity is oriented perpendicular to the direction of

cell elongation, and in the case where the distribution of coupling strengths is heterogeneous, the polarity is ordered toward a strongly coupled adhesive side. These dynamical properties are elucidated numerically and theoretically. Moreover, other properties including the effects of the form of the system boundary, an external signal and noise, and defects of polarity are presented.

In Chapter 5 and the following chapters, the ordering dynamics of cellular phases are focused upon, by considering spiral chaos in which spirals repeat to generate and annihilate. This study is motivated by atrial fibrillation whose dynamics resemble spiral chaos. The atrium is supposed to show spiral chaos of electrical waves when the heart undergoes atrial fibrillation. Catheter ablation, by which the atrium is subdivided into several parts, is known to be effective at terminating chaotic dynamics. Hence, it is theoretically expected that there is a relation between the stability of a chaotic state and its system size. Indeed, it is known that the lifetime of transient spiral chaos grows exponentially as the system size increases.

In Chapter 6, a theoretical formula for predicting the lifetime of spiral chaos in excitable media is derived. The distribution of the number of defects approaches the Gaussian distribution according to central limit theorem as the system size increases. Using this fact, a general expression for the dependence of lifetime on system size is provided; this relation is valid for large system sizes, and the dependence is indeed exponential. It is confirmed that the expression of lifetime is in good agreement with numerically obtained lifetime values with parameter sets near the onset of transient chaos.

In Chapter 7, to verify generality of the argument in Chapter 6, a model of oscillatory media manifesting transient spiral chaos is numerically analyzed and consistency of the claims is confirmed.

In Chapter 8, after summarizing this research, possible applications are discussed.

Chapter 1

Introduction

1.1 Ordering

Ordering refers to a phenomenon in which a system consisting of multiple units forms an ordered structure via interactions among the units [1, 2, 3, 4]. Representative examples include magnetization [5, 6] and synchronization [7, 8], in which polarity orientations and oscillation phases form a coherent structure, respectively. These phenomena are widespread in nature [9, 10, 11]. If a system fails to order, various malfunctions may occur [12, 13].

The structure and dynamics of a population of cilia provides a striking example of ordering. Motile cilia cover many organs, such as the respiratory tract and semicircular canals. Beating of cilia mutually synchronizes through hydrodynamic interaction among the cilia, thus causing efficient directional fluid flow for transport of materials [11]. Moreover, directions of cilia are aligned, and this situation is supposed to support synchronized dynamics of cilia [11]. Heart beat is a familiar example of synchronization. Heart beat is realized by synchronized dynamics within a population of cardiac cells through electric interactions between neighboring cells.

In many cases, a tissue level order is needed. How is such global ordering implemented in biological systems? Although the importance of ordering has been recognized, its mechanism has not yet been fully elucidated. Such a problem has been dealt with in physical and chemical systems, and several mathematical models have been proposed [5, 6, 14, 15]. Those models are expected to be useful for the understanding of ordering in biological systems. In the following sections, some important models describing an ordering process are introduced.

1.2 Mathematical models of ordering

Various models have been proposed for dissecting the mechanism of ordering. These mathematical models help us to understand the transition from a disordered phase to an ordered one and make it possible to describe concentric traveling waves or spiral waves, which are seen in chemical reactions. Here, the XY model, which describes a ferromagnetic interaction among spins, is introduced; Winfree model and Kuramoto model, which describe synchronization of oscillators; and reaction–diffusion models describing pattern ordering.

1.2.1 The XY model

The XY model is a well-known model describing ferromagnetic interaction among spins, and is used frequently in statistical physics. For example, Kosterlitz and Thouless predicted the existence of the order–disorder transition in a two-dimensional system by means of this model and won the Nobel Prize in Physics in 2016 [16, 17]. In the XY model, the spin state is described by a unit vector $\boldsymbol{s}_i = (\cos\theta_i, \sin\theta_i)$ where θ_i is the orientation of spin. θ_i is called the phase of unit i. A lattice system with nearest-neighbor coupling is considered, which is schematically depicted in Fig. 1.1. The Hamiltonian of this system is given by

$$\mathcal{H} = -J \sum_{j \in A(i)} \boldsymbol{s}_i \cdot \boldsymbol{s}_j = -J \sum_{j \in A(i)} \cos(\theta_j - \theta_i). \tag{1.1}$$

Here, $A(i)$ is the group of cells adjacent to cell i. In the case of zero temperature and overdamped limit, the dynamical equation for θ_i is given as

$$\frac{d\theta_i}{dt} = J \sum_{j \in A(i)} \sin(\theta_j - \theta_i). \tag{1.2}$$

In this thesis, we refer to this dynamical equation as the XY model. In this model, when all the spins have the same orientation, i.e., all the phases are in phase, and the energy reaches the minimum. Nevertheless, in a large system, such a globally ordered state is difficult to obtain from general initial conditions because many topological defects may appear.

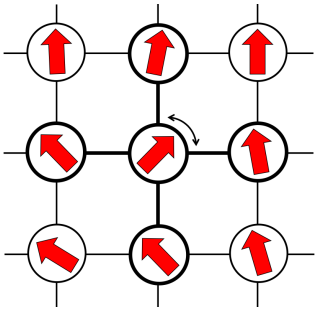

Figure 1.1: Illustration of the XY model on a two-dimensional plane. Each spin interacts with its nearest neighbors and varies its spin orientation to align with its neighbors.

1.2.2 The Winfree model and Kuramoto model

The Kuramoto model is similar to the XY model [7]. This model is based on the Winfree model of coupled oscillators [18] and enables us to deal with synchronization dynamics analytically. Winfree does not describe the mathematical model in his paper [18], but in the context, the Winfree model is expressed as

$$\frac{d\phi_i}{dt} = \omega_i + \frac{K}{N}\sum_{k=1}^{N} Z(\phi_i)P(\phi_k). \tag{1.3}$$

This model describes globally coupled oscillators with uniform coupling strength. ϕ_i and ω_i are the phase and the natural frequency of unit i $(1 \leq i \leq N)$, respectively. ω_i is distributed randomly. K denotes the coupling strength, and N is the number of oscillators. $Z(\phi_i)$ is the phase sensitivity of oscillator i, and $P(\phi_k)$ represents the signal from oscillator k. The distribution of ω_i and the interaction promotes descynchronization and synchronization, respectively. On the basis of numerical simulations of the Winfree model, Winfree predicted the existence of a phase transition from desynchronized to synchronized states. In other words, a critical value of K exists below and above which, oscillators desynchronize and synchronize, respectively.

To confirm this Winfree's prediction, Kuramoto proposed a model that can be dealt with analytically [7]. This model, which is called the Kuramoto model is given as

$$\frac{d\phi_i}{dt} = \omega_i - \frac{K}{N}\sum_{k=1}^{N} \sin(\phi_i - \phi_k), \tag{1.4}$$

and enables us to clarify the details of the phase transition.

Both the Winfree model and Kuramoto model are usually referred to as phase models or phase oscillator models, and phase models are known to be useful for understanding synchronization [7, 19]. The analytical method for deriving phase models, which was first proposed by Kuramoto, is used widely. This theory can be used to derive a phase model from a complicated reaction–diffusion model.

1.2.3 A reaction–diffusion system

A reaction–diffusion system describes local chemical reactions and diffusion of substances distributed in space. A reaction–diffusion system can generally be modeled as

$$\dot{\boldsymbol{X}} = \boldsymbol{F}(\boldsymbol{X}) + \hat{D}\nabla^2 \boldsymbol{X} \tag{1.5}$$

where vector $\boldsymbol{X}$ is a set of chemical concentrations, $\hat{D}$ is a diagonal matrix of diffusion coefficients, $\boldsymbol{F}(\boldsymbol{X})$ represents local reactions, and ∇^2 is Laplacian. This system is employed to describe various natural phenomena. In particular, the Turing model, which describes a system consistenting of two chemical substances called an activator and inhibitor, is expressed as [20]

$$\begin{aligned} \frac{\partial U}{\partial t} &= f(U,V) + D_U \nabla^2 U \\ \frac{\partial V}{\partial t} &= g(U,V) + D_V \nabla^2 V \end{aligned} \tag{1.6}$$

where U and V are the activator and inhibitor, respectively; f and g are functions describing local reactions; and D_U and D_V are diffusion coefficients. In this model, a steady uniform state is assumed to be stable in the absence of diffusion. Counterintuitively, Turing has demonstrated that this uniform state can be destabilized when the diffusion coefficient of inhibitor, D_V, is sufficiently greater than that of the activator, D_U. When the activator increases to some extent locally, the inhibitor also increases to suppress the activator. Because of the assumption $D_U \ll D_V$, the inhibitor diffuses much more quickly than the activator. Therefore, the inhibitor cannot suppress the activator completely. In contrast, in the region where the amount of the activator is sufficiently low, the diffused inhibitor suppresses the activator. In one-dimensional space, a stripe pattern may appear (Fig. 1.2). In the case of a two-dimensional system, various ordered patterns such as spiral waves, dots, and stripes can be seen. These patterns are similar to the epidermis of various animals including the zebra and tropical fish.

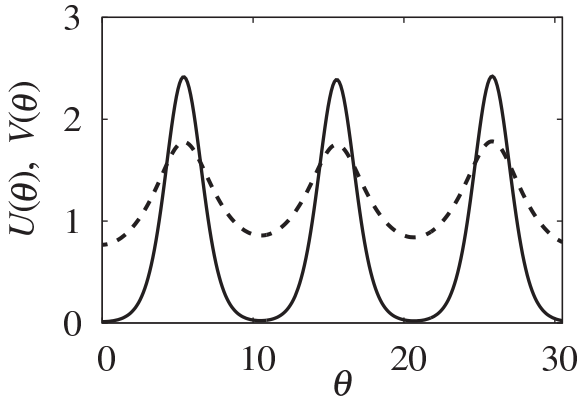

Figure 1.2: A one-dimensional periodic pattern derived from the Turing model [21]. The solid and dashed lines are the concentrations of activator U and inhibitor V, respectively.

The Turing model is known to be helpful for understanding biological pattern formation [21, 22].

1.3 Organization of the thesis

In this thesis, we focus on the ordering of polarity and of the oscillation phase of cell populations in the first part (Chapters 2–4) and in the second part (Chapters 5–7), respectively.

In the first half of this thesis, we deal with the ordering dynamics of cellular polarity and elucidate a mechanism underlying the formation of global order. Based on experiments with polarity of epithelial cells of *Drosophila*, many mathematical models are considered [5, 6, 14, 15]. One of the famous models of ordering belongs to Amonlirdviman [5], which is described via the reaction–diffusion model in Section 1.2.3. As other types of ordering model, the Akiyama model represents the polar dynamics by means of the XY model (Section 1.2.1) [14]. In these other studies, to understand the mechanism of the global polarity ordering, a global concentration gradient is included in the model, or a detailed model based on experiments is considered. Nonetheless, these models have merits and demerits as shown in Chapter 2, and we analyze them as follows to more easily investigate what realizes global polar ordering. We reduced the reaction–diffusion model via variables describing the concentration of chemical substances phenomenologically according to the phase reduction theory [7, 18, 23], which is the method first devised by Winfree and Kuramoto (Section 1.2.2), for a system with space translational symmetry, and we constructed a simple phase model. As a result, it becomes clear that the shapes of cells and the boundary of the

system affect the global orientation of polarity. These dynamical properties are elucidated numerically and theoretically. Moreover, other properties including the effects of coupling heterogeneity, an external signal and noise, and defects of polarity are presented.

In the second half of this thesis, we focus on the ordering dynamics of cellular oscillations by considering spiral chaos in which spirals repeat to generate and annihilate [1, 7]. Our aim is to provide a theoretical description for understanding the system size dependence of the lifetime of transient spiral chaos. This study was motivated by the atrial fibrillation whose dynamics resemble spiral chaos [12]. The atrium is supposed to exhibit spiral chaos of electrical waves when the heart causes atrial fibrillation, and it is known that the lifetime of transient spiral chaos grows exponentially as the system size increases [12]. To derive the theoretical equation for predicting this lifetime, we analyzed the number of defects corresponding to the number of waves with reaction–diffusion models. By considering central limit theorem [24], theoretical formula for predicting the lifetime of spiral chaos in excitable media is derived.

Chapter 2

Polarity ordering analysis of planar cell polarity (PCP)

In this chapter, we introduce planar cell polarity (PCP), which is one of the examples of ordered polarity, and a previous study on cell polarity.

2.1 Background and an aim

Although ordering phenomena are important in nature as mentioned in the previous chapter, the ordering mechanisms have not been fully understood. One of the phenomena, that has not been clarified in spite of many experiments is global ordering of the polarity of hair in epithelial cells. In epithelial tissues of multicellular organisms, i.e., the outer layer packed with many flattened cells, it is known that hairs grow along a specific axis. At the stage of morphogenesis of tissues and organs, PCP is one of the polarity-orientating phenomena whereby each cell's polarity is pointed in a specific direction at the cellular level. This phenomenon refers to the coordinated alignment of the cell polarity across the planar tissue, and detailed experiments on the molecular mechanism of their polarity formation have been performed on *Drosophila* wings and other tissues. In *Drosophila* wings, it is known that one hair grows from the center of a cell to a certain direction, which makes the cell polar. These hairs are in a part of epithelial cells containing abundant actin fibers. The wing is subdivided into two parts: a hinge and blade (Fig. 2.1). At pupal stages, almost until 20 h after puparium formation (hAPF) the wing hinge contracts in the proximal direction. On the other hand, the blade extends in the distal direction, which is the direction of the tip of the wing.

During this period, epithelial cells of the wing proliferate actively, migrate and divide, then the whole wing shape forms gradually. Regarding hair polarity

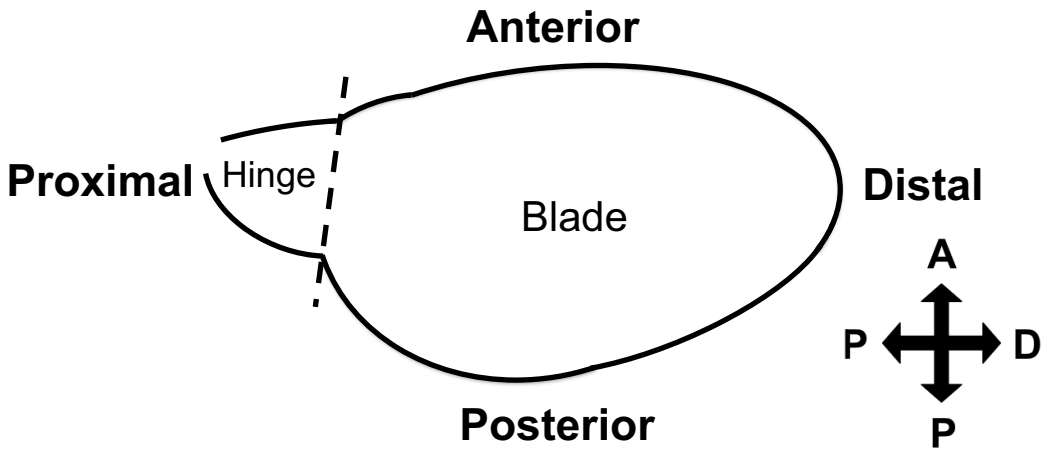

Figure 2.1: Illustration of the wing. The base of the wing is called a "hinge," and the wide part of the wing is called a "blade." The direction along the axis connecting the base and the tip of the wing is the proximal–distal (PD) axis. The axis in the direction perpendicular to the PD axis is the anterior–posterior (AP) axis.

determination, localization of the proteins that are important for PCP occurs up to 32 hAPF. These PCP proteins are called core PCP proteins, which include the seven-pass transmembrane receptor Frizzled (Fz), seven-pass transmembrane cadherin Flamingo (Fmi; aka Starry night), the four-pass transmembrane protein Strabismus (Stbm; aka Van Gogh, Vang), Dishevelled (Dsh), Diego (Dgo), and cytoplasmic component Prickle (Pk) [25, 26]. In the absence of any single PCP protein, cell polarity is misoriented. The complexes of proteins come into contact between proximal and distal cell boundaries, hence complexes of Fz, Dsh, and Dgo accumulate in the distal direction, and complexes of Vang and Pk accumulate in opposite directions (Fig. 2.2). In addition, complexes of Fz and Vang antagonize each other within the cell. Fmi can be localized on both sides of a cell. This localizing direction of Fz complexes coincides with polarity direction of epithelial cells' hairs.

In the wing of *Drosophila*, more than $10,000$ cells are packed. It is surprising and interesting that polarity is oriented globally in the same direction in the system with a large number of cells. How would they implement the global ordered polarity in such a huge system? XY model in Section 1.2.1, which orients the alignment of spins via cell–cell interaction between adjacent cells, can polarize locally but not globally as shown in Fig. 2.3.

Actually also in nature, it is still unclear how global ordering is realized. In recent experiments, the presence of a global concentration gradient distributed throughout the epithelial tissue, and the anisotropy of the system caused by a me-

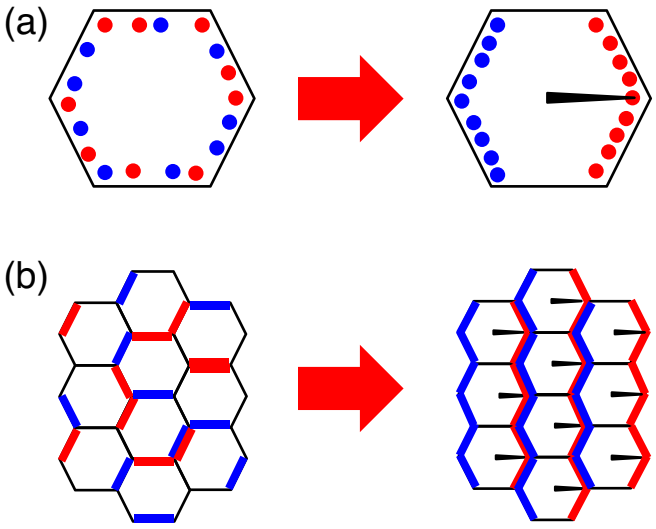

Figure 2.2: Illustration of interaction of PCP proteins. The red and blue points indicate the complexes of Fz and Vang, respectively. (a) Intracellular interaction. Uniformly distributed proteins antagonize each other and polarize. (b) Intercellular interaction. Different types of proteins attract each other. Hairs are oriented in the direction where Fz complexes localize.

chanical force is reported. These global concentration gradients and anisotropy of the system are thought to cause global polarity ordering. We shall introduce more details on these two factors. For the global concentration gradient in the wing of *Drosophila*, it has been confirmed that atypical cadherin Dachsous (Ds) has a distal–proximal gradient of the expression level from distal to proximal, and Fz and Vang are localized in a low- and high-expression region, respectively [27]. Hence, in that case, the global ordering scenario is as follows. Even if the polarity is oriented locally only by cell–cell interactions, it is difficult to identify the direction in which it is aligned. Then, via a global concentration gradient, Ds plays a role of an inducer to determine the direction of ordering. Protein conjugates of the PCP protein Fz, which senses Ds concentration, move in the direction of the low concentration of Ds in the cell. Thus, cell polarity is oriented globally along the Ds concentration gradient. In mathematical models, the model of Akiyama et al. [14], which we introduce later, takes into account the effect of a global concentration gradient added to the XY model. Nonetheless, it is not yet clear whether this global gradient is essential for the proximal–distal (PD) alignment during pupal stages because some experiments revealed that cell polarity can be oriented to some extent globally even in the absence of a global concentration gradient [28].

On the other hand, Aw and Devenport et al. proposed that the mechanical

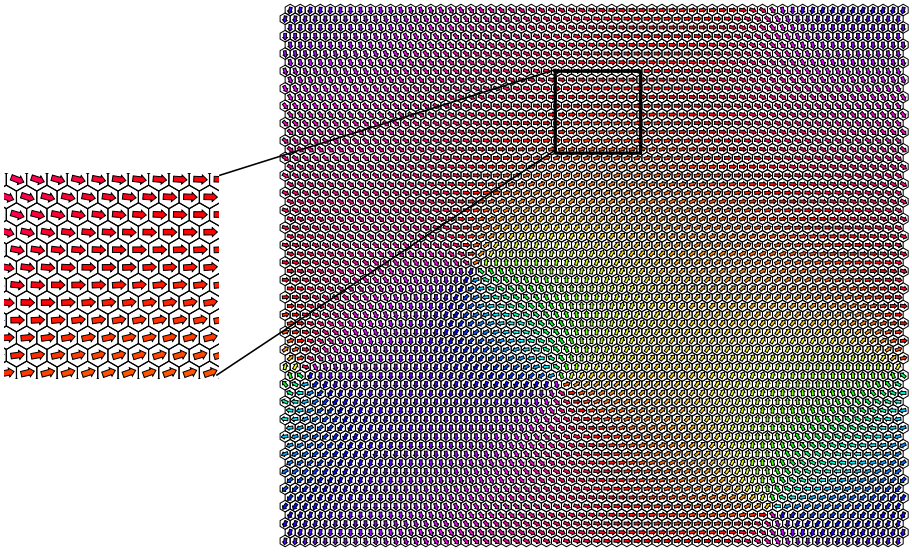

Figure 2.3: The XY model, which is a well-known spin model, can order cell polarity locally but it is difficult to order cell polarity globally when there are many cells in a system. In a 60×60 cells system, there are defects and we can see that global ordering is failed.

force affecting a wide range of organization types influences the implementation of global polarity formation [15, 27]. In the polarity experiments on the skin of mice by Aw and colleagues, a mechanical force is first applied to the tissue at an early stage of embryonic development, and the emergence of tissue anisotropy is confirmed. In such an anisotropic tissue, cells tend to divide in the direction perpendicular to the anterior–posterior (AP) axis. When the direction of cell division is oriented along the AP axis, the new side of the cell increases in along the AP axis accordingly. As a result, the generation and annihilation of sides of cells on the AP axis occur frequently, and many PCP proteins diffusing inside cells tend to accumulate near the side oriented in the direction of the PD axis, which has existed for a long time. The protein to be accumulated is atypical cadherin called Celsr 1, and hair grows in places where this protein accumulates in the case of mice. Similarly, in the case of a wing of *Drosophila*, anisotropy of cell division is generated by elongation of the tissue, thereby causing a bias in the direction in which the PCP protein accumulates, and polarity is oriented in the same direction across a long distance. The well-known mathematical model that is intended to reproduce such anisotropy of tissues is the model of Aigouy et al. [6]. Even though their model will be introduced in detail later, they made it possible to consider cell deformation and elongation during polarity formation using the cell vertex model, and global oriented polarity is also represented.

These simple phenomenological models including Akiyama and Aigouy model are similar to models of magnetization or synchronization, which are observed in a population of spins or oscillatory units [7, 17, 18, 19, 29], though some of these are somewhat artificial.

Therefore, our aim is to propose a theoretical framework to understand the generic dynamical properties of polarity alignment and to reveal what drives global polarity ordering. To clarify the ordering mechanism, we derive a phase model by applying the phase reduction theory to a reaction–diffusion model that describes PCP dynamics [30]. Using our model, essential dynamical properties including the effects of cell shape, of coupling heterogeneity, and an external signal and noise can be elucidated analytically. In Chapter 4, which is the last chapter for polarity ordering, we show that axial asymmetry in the system, such as oriented cell elongation and asymmetric distribution of coupling strength, can be a global cue for the orientation of cell polarity across the entire tissue.

2.2 Previous mathematical studies

In this section, we introduce previous models of polarity ordering. These models are based on experimental results from *Drosophila* wings and mouse embryos.

2.2.1 The PCP model proposed by Aigouy et al.

The mathematical model of cell polarity proposed by Aigouy et al. is based on the vertex model [6]. This model includes terms that express cell–cell interaction, intracellular interactions and cell extension. The mechanisms of intercellular and intracellular interactions conform to the mechanisms described in Section 2.1. The cell extension term is based on one study in [31]. In their experiments, they found that microtubules in the cell align along the cell elongation direction when cells are deformed. PCP protein Fz accumulates at the edge of the microtubules, then the direction of cell polarity is determined. Therefore, from the results of experiments, they assume that microtubules are aligned in the direction of elongation of cells during cell deformation, and the cell extension term has an effect that makes it easy for cell polarity to be ordered along the cell elongation direction. However, a potential function is employed so that the cell polarity is ordered in the direction of cell elongation, and this function is slightly artificial. Although this mathematical model is easy to calculate, it is unclear whether such potential function exists in nature.

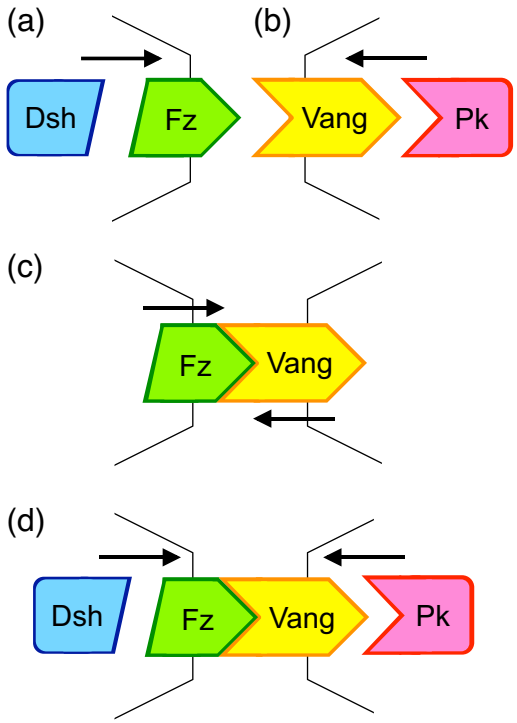

Figure 2.4: (a,b) Intracellular (c,d) and intercellular interactions. (a,b) Fz and Vang on the cell membrane attract Dsh and Pk, respectively. (c) Fz and Vang attract each other and form a complex through the membrane. (d) Dsh and Pk are attracted to the FzVang complex too.

2.2.2 The PCP model proposed by Amonlirdviman et al.

As a more phenomenological description for concentrations of proteins in each cell, some models are described by a reaction–diffusion system in detail [5, 10]. Cells in these models are coupled with adjacent cells via contacting surfaces. Amonlirdviman also describes cell polarity formation using a reaction–diffusion model (Eq. (2.1)). This mathematical model of PCP includes four proteins: Dsh, Fz, Pk, and Vang. The coupling scenario for each protein is as follows. Fz interacts with Dsh to create the DshFz complex, and Vang interacts with Pk to create VangPk (Fig. 2.4).

For the intercellular interaction, Fz interacts with Vang on an adjacent cell membrane to form the FzVang complex. This complex is restricted in its localization (and movements) to the adhesion surface where the complex was formed, and becomes a larger complex by interacting with Dsh and Pk there. Via such intracellular and intercellular interactions, complexes DshFz, VangPk, FzVang, FzVangPk, and DshFzVangPk are formed. These complexes may also disssociate. FzVang, FzVangPk, and DshFzVangPk can exist only at the adhesion junction,

which is shared with adjacent cells. Therefore, Fz, Vang, and their complexes only diffuse on cell membrane. In contrast, Dsh and Pk can diffuse freely within the cell. In the Amonlirdviman model, this complicated molecular behaviour is described in detail. Actually, their model is formulated as follows. Cell shapes are set to a regular hexagon. Each variable in the model (2.1) represents the concentration of the PCP protein complex at each time point.

$$
\begin{aligned}
\frac{\partial[\mathrm{Dsh}]}{\partial t} &= -P_1 - P_5^{\dagger} - P_8^{\dagger} + \mu_{\mathrm{Dsh}}\nabla^2[\mathrm{Dsh}] \\
\frac{\partial[\mathrm{Pk}]}{\partial t} &= -P_3 - P_7 - P_{10} + \mu_{\mathrm{Pk}}\nabla^2[\mathrm{Pk}] \\
\frac{\partial[\mathrm{Fz}]}{\partial t} &= -P_1 - P_2^{\dagger} - P_6^{\dagger} + \mu_{\mathrm{Fz}}\nabla^2[\mathrm{Fz}]_{\mathrm{D}} \\
\frac{\partial[\mathrm{Vang}]}{\partial t} &= -P_2 - P_3 - P_4 + \mu_{\mathrm{Vang}}\nabla^2[\mathrm{Vang}] \\
\frac{\partial[\mathrm{DshFz}]}{\partial t} &= P_1 - P_4^{\dagger} - P_9^{\dagger} + \mu_{\mathrm{DshFz}}\nabla^2[\mathrm{DshFz}]_{\mathrm{D}} \\
\frac{\partial[\mathrm{VangPk}]}{\partial t} &= P_3 - P_6 - P_9 + \mu_{\mathrm{VangPk}}\nabla^2[\mathrm{VangPk}] \\
\frac{\partial[\mathrm{FzVang}]}{\partial t} &= P_2 - P_5 - P_7 + \mu_{\mathrm{FzVang}}\nabla_s^2[\mathrm{FzVang}]_{\mathrm{D}} \\
\frac{\partial[\mathrm{DshFzVang}]}{\partial t} &= P_4 + P_5 - P_{10} + \mu_{\mathrm{DshFzVang}}\nabla_s^2[\mathrm{DshFzVang}]_{\mathrm{D}} \\
\frac{\partial[\mathrm{FzVangPk}]}{\partial t} &= P_6 + P_7 - P_8 + \mu_{\mathrm{FzVangPk}}\nabla_s^2[\mathrm{FzVangPk}]_{\mathrm{D}} \\
\frac{\partial[\mathrm{DshFzVangPk}]}{\partial t} &= P_8 + P_9 + P_{10} + \mu_{\mathrm{DshFzVangPk}}\nabla_s^2[\mathrm{DshFzVangPk}]_{\mathrm{D}}
\end{aligned}
\tag{2.1}
$$

where $\mu_{\boldsymbol{X}}$ is the diffusion rate of $\boldsymbol{X}$, and functions $P_1 \sim P_{10}$ represent complex chemical reaction equations for PCP proteins. A global bias signal is applied to the diffusion terms $\nabla_s^2[*]_{\mathrm{D}}$ so that substances are accumulate in a certain direction. The global bias signal is set to be stronger in the direction toward the proximal side of the wing. The variable labeled with † indicates that the reaction can proceed only on the membrane, and is shared with an adjacent cell. The subscript "s" under the Laplacian indicates that the diffusion term acts only on the membrane.

Using this mathematical model, they analyzed the orientation of cell polarity and compared the results with experimental data. They also investigated how cell polarity changes when there is a region with defective cells in an epithelial sheet. In the experiments, when there are Fz-deficient cells in the sheet, hairs are oriented in the direction toward the defective-cell region. On the contrary, when the protein that antagonizes Fz is lost in some region on the sheet, hairs

align in the direction opposite to the location of defective cells. These experimental results can be considered in detail in their model. Although the model is unsuitable for numerical calculations that require a large number of cells, and it is difficult to understand the mechanism of PCP because the model involves many equations, it is one of the famous PCP models that can reproduce cell polarity as seen in experiments.

2.2.3 The PCP model proposed by Akiyama et al.

Akiyama et al. proposed a model based on XY model, which is easier to deal with than other phenomenological models [14]. In their model, they focus on the dynamics of PCP proteins Fz and Vang. Because hairs grow in the direction of Fz proteins' localization, variable ϕ_i of cell i is set to the orientation angle of Fz localization, and the model is described as follows:

$$\dot{\phi}_i = \sum_{j \in A(i)} \sin(\phi_j - \phi_i). \tag{2.2}$$

Here, $A(i)$ is a set of adjacent cells j of cell i. In this case, cell polarity can get oriented in a certain direction though it depends on initial conditions. The model is very simple, but still there is a problem because as the number of cells increases, defects tend to be generated in the system. Therefore, they added a global gradient term of concentration to the model.

$$\dot{\phi}_i = a \sum_{j \in A(i)} \sin(\phi_j - \phi_i) + b \sin(\Psi_i - \phi_i), \tag{2.3}$$

where Ψ_i follows the von Mises distribution, and a and b are the parameters. Because the model is equipped with the new gradient term, the direction of the cell polarity is ordered naturally depending on distribution Ψ_i. Actually, PCP proteins with such global concentration gradients have been found, and it is known that the direction of cell polarity is aligned against the gradient of the global concentration (i.e., in the direction of the decrease). Nevertheless, even in the absence of a global concentration gradient, the polarity is aligned in the correct direction [28], and the effect of global gradient on PCP is unclear.

Chapter 3

The phase model of polarity ordering in spatially extended dynamical units

In this chapter, we first construct a reaction–diffusion model of PCP similar to the dynamical process of global cell alignment. Our newly constructed model can show alignment of cell polarity, but its numerical simulation is difficult for a large system with many cells, and it is not easy to understand polarity dynamics. Therefore, we apply the phase reduction theory to our reaction–diffusion model. With this theory, it is possible to approximate the multidimensional dynamical system that has a limit cycle or a spatially translational solution involving phase models with only one variable. In Section 3.2.3, we apply this method to the reaction–diffusion model to derive the phase model describing the polarity ordering.

3.1 The reaction–diffusion model of polarity ordering

In this section, we introduce a reaction–diffusion model with cell–cell interaction for global alignments of cell polarity to make the model more suitable for experimental results by proposing a phenomenological model [30]. In actual cell sheets, PCP proteins, which perform an important function in polarity ordering, are present in the two-dimensional plane at the apical membrane of epithelial cells and diffuse only in the epithelial tissue. Hence, we assume that planar cells are spread in two-dimensional space in our model. As shown in Section 2.1, PCP protein complexes accumulate on the cell membrane and interact with adjacent

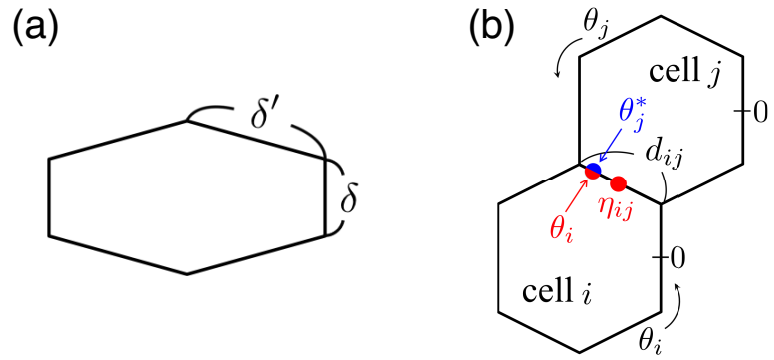

Figure 3.1: A schematic of (a) cell shape and (b) cell alignment. We consider regular or elongated hexagonal cells with perimeter 2π, thus $2\delta + 4\delta' = 2\pi$. η_{ij} and d_{ij} denote the midpoint and the length of the contacting surface between cell i and j, respectively. $\theta_j^* = \theta_j^*(\theta_i)$ denotes a point of θ_j at which cell j faces point θ_i of cell i. Note that η_{ij} can be regarded as the cell-to-cell direction from cell i to cell j.

cells via contacting surfaces. Therefore, we consider that reaction–diffusion dynamics of each cell take place on the one-dimensional surface on cell membrane and assume that localization of PCP proteins within individual cells has already finished. Although we will extend the model to arbitrary polygonal cells in the following chapter, we assume that the shape of a cell is an axially symmetrical hexagon with perimeter $L_i = 2\pi$ as shown in Fig. 3.1 for the sake of simplicity here. The system is filled with cells of the same shape.

In the *Drosophila* wing, it is known that cells with an arbitrary shape at the early pupal stage divide and are eliminated repeatedly, and the epithelial sheet is eventually packed with regular hexagonal cells.

Now we consider a reaction–diffusion system with an interaction term implying that the cell interacts with adjacent cells only at an adhesion surface. Each cell obeys the following equation

$$\frac{\partial}{\partial t}\boldsymbol{X}_i = \boldsymbol{F}(\boldsymbol{X}_i) + \hat{D}\frac{\partial^2 \boldsymbol{X}_i}{\partial \theta_i^2} + \varepsilon \sum_{j \in A(i)} \boldsymbol{H}_{ij}, \tag{3.1}$$

where $\boldsymbol{X}_i = \boldsymbol{X}_i(\theta_i, t)$ $(i = 1, \ldots, N)$ denotes the concentration of a chemical species at time point t and at the position θ_i $(0 \le \theta_i < L_i)$ on the surface of cell i. $\boldsymbol{F}(\boldsymbol{X}_i)$ describes the local reaction dynamics. $\hat{D}$ is the diagonal matrix consisting of diffusion coefficients. $A(i)$ is the set of cells adjacent to cell i. $\boldsymbol{H}_{ij} = \boldsymbol{H}_{ij}(\theta_i, t)$ describes intercellular interactions, and ε is the coupling strength. Note that $\boldsymbol{F}$ and $\hat{D}$ describe intracellular dynamics. An interaction occurs at every contact

point and is dependent on the state at the contact point, i.e.,

$$\boldsymbol{H}_{ij}(\theta_i, t) = \boldsymbol{H}_{ij}(\boldsymbol{X}_i(\theta_i, t), \boldsymbol{X}_j(\theta_j^*, t)), \tag{3.2}$$

where $\theta_j^* = \theta_j^*(\theta_i)$ is a point of θ_j at which cell j faces point θ_i of cell i, as illustrated in Fig. 3.1(b), and $\boldsymbol{H}_{ij}(\theta_i, t)$ vanishes if cell i does not come into contact with cell j at θ_i. In addition to this interaction term, we can consider and add various effects such as an external signal and noise as shown in Section 4.4. In each cell, $\boldsymbol{X}_i(\theta_i, t)$ is assumed to be a unimodal distribution for $\varepsilon = 0$; i.e., polarity is spontaneously formed. This is because the concentration distribution of a chemical substance, which is assumed as a variable of this model, has a peak as a result of accumulation on the membrane. A hair in each cell grows from the center in the direction where the concentration of the diffusing chemical substance is maximal. Therefore, the position of the concentration peak of the first component of $\boldsymbol{X}_i(\theta_i, t)$ at time t of cell i determined by $U_i(\theta_i, t)$ can be defined as the polarity direction of cell i. We analyzed two models: (a) the real Ginzburg–Landau equation (GLE) [32] in Eq. (3.3) and (b) the activator–inhibitor model [21] in Eq. (3.4). For the GLE model, we can get steady state solutions and functions required for phase model derivation by hand with ease. In general, however, for many other activator–inhibitor models such as the model of [21], it is difficult to derive steady state solutions and other functions analytically.

Both models have two variables, denoted by $\boldsymbol{X}_i = (U_i, V_i)$, and $\boldsymbol{F}$ and $\hat{D}$ read

$$\boldsymbol{F} = \begin{pmatrix} U_i - ({U_i}^2 + {V_i}^2)U_i \\ V_i - ({U_i}^2 + {V_i}^2)V_i \end{pmatrix}, \quad \hat{D} = \begin{pmatrix} D_0 & 0 \\ 0 & D_0 \end{pmatrix}, \tag{3.3}$$

where D_0 is set to 0.3 where a stable unimodal distribution is obtained, and

$$\boldsymbol{F} = \begin{pmatrix} \frac{\rho_U U_i^2}{(1+\kappa U_i^2)V_i} - \mu_U U_i + \sigma_U \\ \rho_V U_i^2 - \mu_V V_i, \end{pmatrix}, \quad \hat{D} = \begin{pmatrix} D_U & 0 \\ 0 & D_V \end{pmatrix}, \tag{3.4}$$

where $\rho_U = 0.01, \rho_V = 0.02, \mu_U = 0.01, \mu_V = 0.02, \sigma_U = 0.0, \kappa = 0.0, D_U = 0.005$, and $D_V = 0.2$, respectively. For simplicity, these examples are two-variable models, but any number of variables can be used. The former is a long-wave amplitude equation, which is widely used to describe various systems near the onset of instability. The parameter values for the latter model are taken from Ref. [21], and these are set so that the steady state solution is time-independent. The latter is a reaction–diffusion model describing biological pattern formation. In these models, given appropriate initial conditions, $\boldsymbol{X}_i$ shows a stationary unimodal distribution for $\varepsilon = 0$; thus, they are suitable as dynamical models

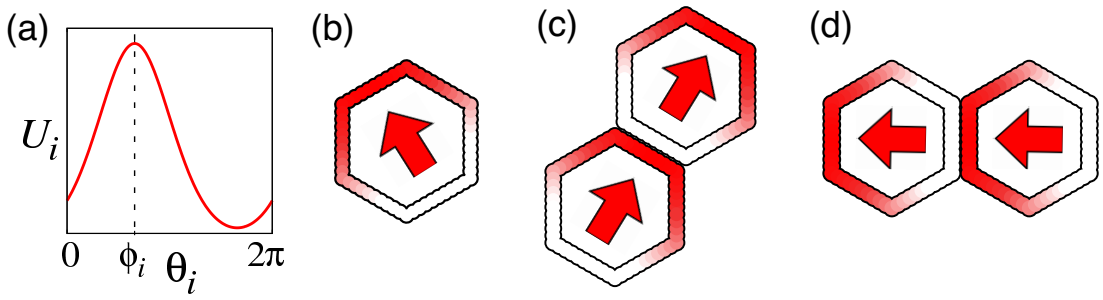

Figure 3.2: The polarity pattern of (a,b) a single cell and (c,d) two coupled cells. In (a) and (b), a steady state profile of U_i and its color scale representation are displayed, respectively. The arrow in panel (b) indicates polarity orientation. In panels (c) and (d), typical examples of polarity patterns of two coupled cells with different cell alignments are dipicted.

describing cell polarity. Fig. 3.2 (a,b) presents a steady state profile of $U_i(\theta_i, t)$ for $\varepsilon = 0$ numerically obtained via the activator–inhibitor model formulated in Eq. (3.4).

As a simple example of intercellular interaction, we consider linear coupling given by

$$\boldsymbol{H}_{ij}(\theta_i, t) = S_{ij}(\theta_i) \begin{pmatrix} U_i(\theta_i, t) - U_j(\theta_j^*, t) \\ 0 \end{pmatrix}, \tag{3.5}$$

where $S_{ij} = 1$ if cell i faces cell j at θ_i and $S_{ij} = 0$ otherwise; i.e.,

$$S_{ij}(\theta_i) = \begin{cases} 1 & \text{for } |\theta_i - \eta_{ij}| < \frac{d_{ij}}{2} \\ 0 & \text{otherwise.} \end{cases}, \tag{3.6}$$

This cell–cell interactions are set up taking into account that the PCP proteins of adjacent cells move away from the adhesion surface if the same protein exists at the contacting point. The coupling given by Eq. (3.5) acts as mutual inhibition between neighboring cells through the U-component for $\varepsilon > 0$, and thereby polarity ordering takes place as shown in Fig. 3.2(c,d). It can be seen that the direction of cell polarity is ordered toward the area where many cells adhere. Later, another type of linear coupling $-U_j(\theta_j^*, t)$ instead of $U_i(\theta_i, t) - U_j(\theta_j^*, t)$ is considered to demonstrate the robustness of the present results. It can be confirmed that the reaction–diffusion model with such an interaction term shows a cell polarity. Nevertheless, to calculate numerically and analytically by using partial differential equation models of a system with many cells is difficult. Therefore, we attempted to rederive a mathematical model as a simpler model

by using the perturbation theory. The model reduced by that theory is called a phase model. In the following chapter, we explain the way to derive of the phase model.

3.1.1 Linear stability analysis of a reaction–diffusion model

As described in Section 3.1, the distribution of a chemical substance concentration has a peak on a cell membrane. Thus, we need to set the diffusion coefficient so that the solution of the model forms a unimodal distribution at $\varepsilon = 0$. In the text below, we derive the range of diffusion coefficients to form the unimodal distribution by linear stability analysis for a reaction–diffusion model of the GLE.

For the GLE model (Eq. (3.3)), if the equation is set to:

$$\begin{aligned} &\boldsymbol{F}(\boldsymbol{X}^{\mathrm{S}}) + \hat{D}\frac{\partial^2}{\partial\theta^2}\boldsymbol{X}^{\mathrm{S}} = 0, \\ &\hat{D} = \begin{pmatrix} D_0 & 0 \\ 0 & D_0 \end{pmatrix}, \end{aligned} \tag{3.7}$$

where $\boldsymbol{X}^{\mathrm{S}}$ is a steady state solution of the model with $\varepsilon = 0$, the following solution is obtained.

$$\boldsymbol{X}^{\mathrm{S}} = \begin{pmatrix} U^{\mathrm{S}} \\ V^{\mathrm{S}} \end{pmatrix} = \sqrt{1 - D_0}\begin{pmatrix} \cos\theta \\ \sin\theta \end{pmatrix} = \sqrt{1 - D_0}\exp(i\theta). \tag{3.8}$$

Suppose $\delta w(\theta, t)$ is a perturbation, and $\boldsymbol{X}(\theta, t) = \{\sqrt{1 - D_0} + \delta w(\theta, t)\}\exp(i\theta)$. If this is substituted into Eq. (3.3),

$$\begin{aligned} (\mathrm{L.H.S}) &= \frac{\partial \delta w(\theta, t)}{\partial t}\exp(i\theta) \\ (\mathrm{R.H.S}) &\simeq \left\{\sqrt{1 - D_0} + \delta w(\theta, t)\right\}\exp(i\theta) - D_0\sqrt{1 - D_0}\exp(i\theta) \\ &\quad + D_0\left\{\nabla^2\delta w(\theta, t)\exp(i\theta) - i\nabla\delta w(\theta, t)\exp(i\theta)\right. \\ &\quad \left. -i\nabla\delta w(\theta, t)\exp(i\theta) - \delta w(\theta, t)\exp(i\theta)\right\} \\ &\quad - \left[(1 - D_0)\left\{\sqrt{1 - D_0} + \overline{\delta w}(\theta, t)\right\} + 2\,(1 - D_0)\,\delta w(\theta, t)\right]\exp(i\theta), \end{aligned} \tag{3.9}$$

where $\overline{\delta w}$ denotes a complex conjugate of δw. Therefore,

$$\begin{aligned}\frac{\partial \delta w(\theta,t)}{\partial t} &\simeq -(1-D_0)\,\delta w(\theta,t) - 2D_0 i\nabla \delta w(\theta,t) + D_0\nabla^2 \delta w(\theta,t) - (1-D_0)\,\overline{\delta w}(\theta,t),\\ \frac{\partial \overline{\delta w}(\theta,t)}{\partial t} &\simeq -(1-D_0)\,\overline{\delta w}(\theta,t) + 2D_0 i\nabla \overline{\delta w}(\theta,t) + D_0\nabla^2 \overline{\delta w}(\theta,t) - (1-D_0)\,\delta w(\theta,t).\end{aligned} \tag{3.10}$$

Here, let k be the wave number, and let $w_k(t)$ be determined as

$$w_k(t) = \int_0^{2\pi} \delta w(\theta,t) e^{ik\theta} d\theta. \tag{3.11}$$

Applying it to Eqs. (3.10), the following is obtained.

$$\begin{pmatrix} \frac{\partial w_k}{\partial t} \\ \frac{\partial \overline{w_{-k}}}{\partial t} \end{pmatrix} = \begin{pmatrix} -D_0k^2 + 2D_0k - (1-D_0) & -(1-D_0) \\ -(1-D_0) & -D_0k^2 - 2D_0k - (1-D_0) \end{pmatrix} \begin{pmatrix} w_k \\ \overline{w_{-k}} \end{pmatrix}. \tag{3.12}$$

To obtain eigenvalues λ, the determinant is calculated

$$\begin{vmatrix} A + 2D_0k - \lambda & B \\ B & A - 2D_0k - \lambda \end{vmatrix} = \lambda^2 - 2A\lambda + A^2 - 4D_0^2k^2 - B^2 = 0 \tag{3.13}$$

where $A = -D_0k^2 - (1-D_0),\ B = -(1-D_0)$, then

$$\begin{aligned}\lambda &= A \pm \sqrt{4D_0^2k^2 + B^2} \\ &= -D_0k^2 + D_0 - 1 \pm \sqrt{4D_0^2k^2 + (1-D_0)^2}.\end{aligned} \tag{3.14}$$

If $D_0(>0)$ is assumed to be small enough,

$$\sqrt{4D_0^2k^2 + (1-D_0)^2} = \sqrt{1 + (4D_0^2k^2 + D_0^2 - 2D_0)} \tag{3.15}$$

$$\approx 1 + \frac{1}{2}(4D_0^2k^2 + D_0^2 - 2D_0), \tag{3.16}$$

the eigenvalues are approximated as follows.

$$\begin{aligned}\lambda &\approx -D_0k^2 + D_0 - 1 \pm \{1 + 2D_0^2k^2 + \frac{1}{2}D_0^2 - D_0\} \\ &= D_0(2D_0-1)k^2 + \frac{1}{2}D_0^2, \quad -D_0(2D_0+1)k^2 - \frac{1}{2}D_0^2 + 2D_0 - 2.\end{aligned} \tag{3.17}$$

Here, to stabilize only the solution with a unimodal distribution, the case where

$k = 1$ is stable is considered.

$$\lambda = D_0(\frac{5}{2}D_0 - 1) < 0,$$
$$-\frac{5}{2}D_0^2 + D_0 - 2 < 0. \tag{3.18}$$

Finally, the range of diffusion coefficient D_0 is obtained as

$$D_0 < 0.4. \tag{3.19}$$

In this study, the diffusion coefficient is set so that it satisfies the diffusion range, and we assume that the steady state solution forms a unimodal distribution.

3.2 Phase reduction

In the previous section, the reaction–diffusion model was considered. This model given by Eq. (3.1) requires for $N \times M$ partial differential equations when there are N cells in the tissue, and M variables are necessary to describe the interior of the cell. It was clarified that polarity is oriented in a direction in which many cells are aligned if inhibition of interaction of the same proteins between adjacent cells is considered. Although it is not impossible to analyze the dynamics of polarity using the reaction–diffusion model, both analytical and numerical procedures are not easy when we try to investigate the polar dynamics of tissues containing many cells.

Therefore, in this section, we introduce a method called perturbation theory, which derives a very simple ordinary differential equation like Aigouy's [6] or Akiyama's [14] from a phenomenological mathematical model (3.1) to facilitate the analysis. Perturbation theory has a long history, and the fundamental part was established in the 1970s by Winfree [18] and Kuramoto [7]. In general, this theory is described as a method for analyzing the rhythmic systems with limit cycle oscillators. In our reaction–diffusion model, the steady state solution is not a limit cycle solution, hence perturbation theory is not applicable to our model.

Nonetheless, the method was extended, and this improvement enabled analysis of the systems with space translational symmetry by Kawamura and Nakao (Refs. [23, 33]) in 2014. Hence, it became possible to reduce the mathematical model even if the steady state solution does not oscillate. By this extended reduction method devised by Kawamura and Nakao, the phase model is expressed in the spatial integration of the inner product of the phase sensitive function, which is a normalized phase response curve (PRC), and the external perturbation such

as noise and cell interaction. Here, the phase response function describes how much the phase shifts in response to a perturbation when an external stimulus is applied.

In the sections that follow, we consider two cases: the rare case where this phase response function can be obtained analytically, and the case where it is formulated by numerical calculation. By using a kind of perturbation theory called phase reduction, our model of $N \times M$ partial differential equations can be redescribed as a simplified phase model with N ordinary differential equations under the assumption of weak coupling and a unimodal distribution of chemical substances. The derived phase model is extremely easy to handle in both analytical and numerical analysis.

3.2.1 Derivation of the PRC: a direct stimulation method

The PRC is the function that shows how much the phase shifts in response to a weak perturbation. It is important to obtain the PRC when deriving the phase model using perturbation theory; but, in general, analytical derivation of PRC is difficult. PRC is given by the adjoint methods in Section 3.2.2 and by the direct stimulation method measuring the phase shift when direct stimulation is received. Here, the latter method, which is easy to understand intuitively, is considered. Suppose weak stimulus ε is administered at a certain point, $\theta^{'}$, in space at time T to a reaction–diffusion system as shown in Eq. (3.20). Note that the steady state solution of the system does not oscillate when there is no external perturbation.

$$\frac{\partial \boldsymbol{X}}{\partial t} = \boldsymbol{F}(\boldsymbol{X}) + \hat{D}\frac{\partial^2 \boldsymbol{X}}{\partial \theta^2} + \varepsilon \boldsymbol{q}(\theta, \theta^{'}, t, T) \tag{3.20}$$

Vector function $\boldsymbol{q}$ takes $\delta(t-T)\delta(\theta-\theta^{'})$ as the first component of $\boldsymbol{X}$ and 0 for other components. The following figure is the result of numerical calculation (Fig. 3.3). The dotted lines are steady state solutions at $\varepsilon = 0$. We choose the solution where the maximum is taken at $\theta = 0$. While the perturbation is not applied, i.e., $\varepsilon = 0$, the steady state pattern continues to maximize at $\theta = 0$, and the pattern does not move slightly. The red dots represent $U(\theta^{'})$ and indicate the position to which perturbation is applied. The solid lines are the steady state solution shifted after the system receives the perturbation.

We can see that the phase shifts to the right or left when an element of the system is stimulated.

As depicted in Fig. 3.3(a), the pattern shifts left because the right-hand side of the distribution was stimulated. On the contrary, the pattern shifts right when

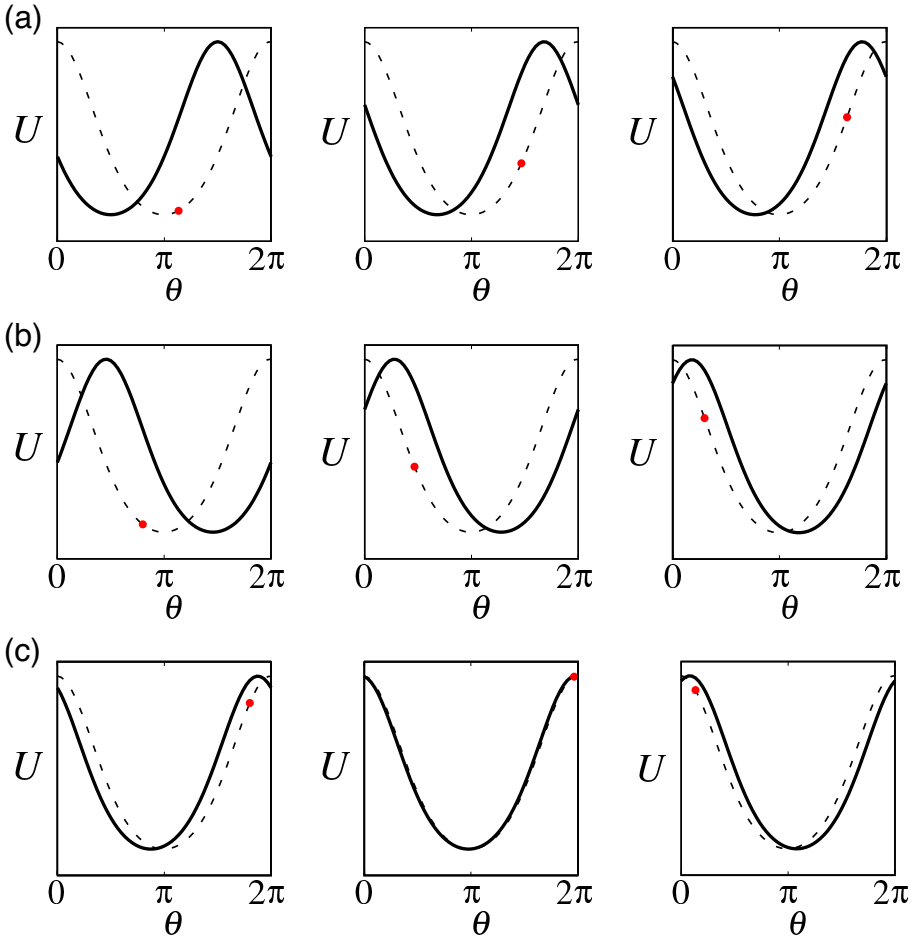

Figure 3.3: The results of the shift when a certain point of the steady state solution of the reaction–diffusion system is stimulated. Red dots indicate where the stimulation was given. The direction and range of shift depend on which element receives the perturbation.

the left-hand side of the distribution was stimulated as shown in Fig. 3.3(b). In addition, we can see that the phase hardly shifts when the stimulation is applied near the peak of the distribution (Fig. 3.3(c)). As described above, the direction and range of the phase shift vary depending on where the external stimulus is applied. In the case when the PRC is constructed by the direct stimulation method, a stimulus of certain strength is applied to each point, and the shift of the pattern is measured each time. Thus, the PRC is illustrated by plotting the deviation of pattern as a function of perturbation strength ε corresponding to each spatial x-coordinate. Nonetheless, the direct stimulation method needs to administer a large perturbation to the model, and it should be noted that an accurate result of the analysis may not be obtained in some cases. Therefore, it is better to employ the mathematical derivation method as in the following

section where a PRC is derived.

3.2.2 Derivation of the PRC: the adjoint method

Following the previous section, we introduce a method to derive a PRC more analytically. This method is analogous to the Malkin theorem [34] using the adjoint method proposed for a limit cycle oscillation system. Now, we consider based on reaction–diffusion model because our aim in this chapter is to apply phase reduction to the reaction–diffusion model with spatially translational symmetry. We regard the right side of Eq. (3.1) with $\varepsilon = 0$ when the model is linearized as operator $\mathcal{L}$. This operator can be subdivided into two parts: the part of Jacobian $\mathcal{L}_1$ and of diffusion $\mathcal{L}_2$. Adjoint operator $\mathcal{L}^\dagger$ is defined according to the following equations with arbitrary functions $\boldsymbol{f}(\theta) = (f_1(\theta), f_2(\theta), \cdots, f_n(\theta))^{\mathrm{T}}$, $\boldsymbol{g}(\theta) = (g_1(\theta), g_2(\theta), \cdots, g_n(\theta))^{\mathrm{T}}$.

$$\langle \boldsymbol{f}, \mathcal{L}\boldsymbol{g} \rangle = \langle \mathcal{L}^\dagger \boldsymbol{f}, \boldsymbol{g} \rangle. \tag{3.21}$$

Here, $\boldsymbol{f}$ and $\boldsymbol{g}$ are assumed to be two-dimensional vectors for the sake of simplicity, and the inner product of 2π-periodic functions $\boldsymbol{f}$ and $\boldsymbol{g}$ is considered. The inner product of the 2π-periodic functions, $\boldsymbol{A}(\theta)$ and $\boldsymbol{B}(\theta)$, is defined by

$$\langle \boldsymbol{A}, \boldsymbol{B} \rangle = \int_0^{2\pi} \boldsymbol{A} \cdot \boldsymbol{B} d\theta. \tag{3.22}$$

Hence, the inner product of $\boldsymbol{f}$ and $\mathcal{L}\boldsymbol{g}$ is obtained as follows.

$$
\begin{aligned}
\langle \boldsymbol{f}, \mathcal{L}\boldsymbol{g} \rangle &= \int_0^{2\pi} \boldsymbol{f}(\theta) \cdot \mathcal{L}\boldsymbol{g}(\theta) d\theta \\
&= \int_0^{2\pi} \boldsymbol{f}(\theta) \cdot \mathcal{L}_1\boldsymbol{g}(\theta) d\theta + \int_0^{2\pi} \boldsymbol{f}(\theta) \cdot \mathcal{L}_2\boldsymbol{g}(\theta) d\theta \\
&= \int_0^{2\pi} \mathcal{L}_1^{\mathrm{T}}\boldsymbol{f}(\theta) \cdot \boldsymbol{g}(\theta) d\theta + \int_0^{2\pi} \begin{pmatrix} f_1(\theta) \\ f_2(\theta) \end{pmatrix} \cdot \begin{pmatrix} D_1\nabla^2 & 0 \\ 0 & D_2\nabla^2 \end{pmatrix} \boldsymbol{g}(\theta) d\theta \\
&= \int_0^{2\pi} \mathcal{L}_1^{\mathrm{T}}\boldsymbol{f}(\theta) \cdot \boldsymbol{g}(\theta) d\theta + \int_0^{2\pi} (f_1(\theta) D_1\nabla^2 g_1(\theta) + f_2(\theta) D_2\nabla^2 g_2(\theta)) d\theta \\
&= \int_0^{2\pi} \mathcal{L}_1^{\mathrm{T}}\boldsymbol{f}(\theta) \cdot \boldsymbol{g}(\theta) d\theta + \sum_i D_i \left\{ \left[f_i \frac{\partial g_i}{\partial \theta} \right]_0^{2\pi} - \int_0^{2\pi} \frac{\partial f_i}{\partial \theta} \frac{\partial g_i}{\partial \theta} d\theta \right\} \\
&= \int_0^{2\pi} \mathcal{L}_1^{\mathrm{T}}\boldsymbol{f}(\theta) \cdot \boldsymbol{g}(\theta) d\theta - \sum_i D_i \left\{ \left[\frac{\partial f_i}{\partial \theta} g_i \right]_0^{2\pi} - \int_0^{2\pi} \frac{\partial^2 f_i}{\partial \theta^2} g_i d\theta \right\} \\
&= \int_0^{2\pi} \mathcal{L}_1^{\mathrm{T}}\boldsymbol{f}(\theta) \cdot \boldsymbol{g}(\theta) d\theta + \sum_i \int_0^{2\pi} (D_i\nabla^2 f_i) \cdot g_i(\theta) d\theta \\
&= \int_0^{2\pi} \left(\mathcal{L}_1^{\mathrm{T}}\boldsymbol{f}(\theta) \cdot \boldsymbol{g}(\theta) + \mathcal{L}_2\boldsymbol{f}(\theta) \cdot \boldsymbol{g}(\theta) \right) \, d\theta
\end{aligned} \tag{3.23}
$$

where $\mathcal{L}^{\mathrm{T}}$ is the transposed matrix of $\mathcal{L}$. Thus,

$$
\mathcal{L}^{\dagger} = \mathcal{L}_1^{\mathrm{T}} + \mathcal{L}_2. \tag{3.24}
$$

From this result, the phase sensitivity function $\boldsymbol{u}^*$ can be obtained.

$$
\begin{aligned}
\frac{\partial \boldsymbol{u}^*}{\partial t} &= \mathcal{L}^{\dagger}\boldsymbol{u}^* \\
&= (\mathcal{L}_1^{\mathrm{T}} + \mathcal{L}_2)\boldsymbol{u}^*
\end{aligned} \tag{3.25}
$$

Phase sensitivity function $\boldsymbol{u}$ required for perturbation theory is a normalized the PRC and is given by

$$
\boldsymbol{u} = \begin{pmatrix} \frac{\partial U_0}{\partial \theta} \\ \frac{\partial V_0}{\partial \theta} \end{pmatrix} \tag{3.26}
$$

on the condition

$$
\int_0^{2\pi} \boldsymbol{u}^* \cdot \boldsymbol{u} \, d\theta = 1.
$$

3.2.3 A phase reduction for the system with spatially translational symmetry

The PRC is given, and finally we can derive the phase equation according to the phase reduction theory for the system with spatially translational symmetry [30]. We assume that the perturbation is sufficiently small, and the solution of the reaction–diffusion model spontaneously forms a single distribution. First, the phase is defined. We define the steady state distribution $\boldsymbol{X}^{\mathrm{S}}(\theta)$ that has a peak at $\theta = 0$ as the steady state solution when $\varepsilon = 0$ in the reaction–diffusion system. Because of the translational symmetry, $\boldsymbol{X}^{\mathrm{S}}(\theta - \theta_0)$ with any constant θ_0 is also a steady state solution. These steady state solutions do not depend on time. When a small perturbation is added, $\boldsymbol{X}_i(\theta_i, t)$ approaches a steady state solution with infinite time, and this distribution of the solution is slightly deviates from $\boldsymbol{X}^{\mathrm{S}}(\theta_i)$. The deviation of this pattern from $\boldsymbol{X}^{\mathrm{S}}(\theta_i)$ is regarded as phase $\phi_i(t)$, and $\phi_i(t)$ is defined such that $\boldsymbol{X}_i(\theta_i, t)$ converges to $\boldsymbol{X}^{\mathrm{S}}(\theta_i - \phi_i)$ as $t \to \infty$. We define the deviation as $\boldsymbol{y}(\theta_i, t)$,

$$\boldsymbol{X}_i(\theta_i, t) = \boldsymbol{X}^{\mathrm{S}}(\theta_i - \phi_i) + \boldsymbol{y}_i(\theta_i, t), \tag{3.27}$$

with $\phi_i(t)$ being the phase of state $\boldsymbol{X}_i(\theta_i, t)$. Hence, $\boldsymbol{y}_i(\theta_i, t) \to 0$ as $t \to \infty$ for $\varepsilon = 0$. Without loss of generality, we assume that $U^{\mathrm{S}}(\theta)$, which is the U component of $\boldsymbol{X}^{\mathrm{S}}(\theta)$, takes its maximum at $\theta = 0$. Then, for sufficiently small $\boldsymbol{y}_i(\theta_i, t)$, $\phi_i(t)$ of $\boldsymbol{X}_i(\theta_i, t)$ is well approximated by the maximum of $U_i(\theta_i, t)$, i.e.,

$$\phi_i(t) \approx \mathrm{argmax}_{\theta_i} U_i(\theta_i, t). \tag{3.28}$$

Thus, ϕ_i may be regarded as the polarity orientation of cell i. Now, the phase equation is derived by calculating the phase sensitive function according to the previous section. Linear operator $\mathcal{L}$ is defined by

$$\mathcal{L} = J + \hat{D}\frac{\partial^2}{\partial\theta^2} \tag{3.29}$$

with Jacobian $J = \partial \boldsymbol{F}(\boldsymbol{X})/\partial \boldsymbol{X}$ estimated at $\boldsymbol{X} = \boldsymbol{X}^{\mathrm{S}}(\theta)$. For Eq. (3.1), we can show that

$$\mathcal{L}^\dagger = J^{\mathrm{T}} + \hat{D}\frac{\partial^2}{\partial\theta^2}, \tag{3.30}$$

where J^{T} is the transpose of J. The eigenfunctions of $\mathcal{L}$ and $\mathcal{L}^\dagger$ are denoted by $\boldsymbol{Y}_\ell(\theta)$ and $\boldsymbol{Z}_\ell(\theta)$ ($\ell = 0, 1, \ldots$), respectively. In particular, the zero-eigenfunctions

are represented by $\boldsymbol{Y}_0$ and $\boldsymbol{Z}_0$, i.e., $\mathcal{L}\boldsymbol{Y}_0 = \mathcal{L}^\dagger \boldsymbol{Z}_0 = 0$. Here, we choose

$$\boldsymbol{Y}_0 = -\frac{\partial \boldsymbol{X}^{\mathrm{S}}}{\partial \theta}. \tag{3.31}$$

These eigenfunctions are assumed to form a complete orthonormal system and are normalized as

$$\langle \boldsymbol{Z}_\ell, \boldsymbol{Y}_m \rangle = \delta_{\ell m}. \tag{3.32}$$

Deviation $\boldsymbol{y}_i$ can be expanded as

$$\boldsymbol{y}_i(\theta_i, t) = \sum_{\ell=1}^{\infty} \boldsymbol{C}_\ell(t) \boldsymbol{Y}_\ell(\theta_i - \phi_i), \tag{3.33}$$

where ϕ_i is the phase of state $\boldsymbol{X}_i(\theta_i, t)$. Note that $\boldsymbol{Y}_0(\theta_i - \phi_i)$ is absent in this expansion because $\boldsymbol{y}_i(\theta_i, t) \to 0$ as $t \to \infty$ for $\varepsilon = 0$.

Substituting Eq. (3.27) into Eq. (3.1), the following is obtained:

$$\boldsymbol{Y}_0(\theta_i - \phi_i)\dot{\phi}_i + \dot{\boldsymbol{y}}_i = \mathcal{L}\boldsymbol{y}_i + \varepsilon \sum_{j \in A(i)} \boldsymbol{H}_{ij} + O(\varepsilon^2). \tag{3.34}$$

Taking the inner product with $\boldsymbol{Z}_0(\theta_i - \phi_i)$ and dropping $O(\varepsilon^2)$, we finally obtain the phase model given as

$$\dot{\phi}_i = \varepsilon \sum_{j \in A(i)} \Gamma_{ij}(\phi_i, \phi_j), \tag{3.35}$$

$$\Gamma_{ij} = \langle \boldsymbol{Z}_0(\theta_i - \phi_i), \boldsymbol{H}_{ij}^{\mathrm{S}} \rangle, \tag{3.36}$$

where $\boldsymbol{H}_{ij}^{\mathrm{S}} = \boldsymbol{H}_{ij}\left\{\boldsymbol{X}^{\mathrm{S}}(\theta_i - \phi_i), \boldsymbol{X}^{\mathrm{S}}(\theta_j - \phi_j)\right\}$. Given the functional forms of $\boldsymbol{X}^{\mathrm{S}}(\theta)$ and $\boldsymbol{Z}_0(\theta)$, Eq. (3.35) serves as a closed equation for phases ϕ_i ($i = 1, \ldots, N$).

3.3 The phase model of a general reaction–diffusion model

We introduced that a reaction–diffusion model with translational symmetry can be reduced to a phase model by means of its steady state solution, phase sensitivity function, and the function of a weak perturbation. Here, we expand these variables and functions derived from the general form of the reaction–diffusion system to a Fourier series and analyze the phase model.

The phase equation is given by Eq. (3.36),

$$\dot{\phi}_i = \varepsilon \sum_{j \in A(i)} \Gamma_{ij}(\phi_i, \phi_j) \tag{3.37}$$

$$\Gamma_{ij} = \left\langle \boldsymbol{Z}_0(\theta_i - \phi_i), \boldsymbol{H}_{ij}^{\mathrm{S}} \right\rangle . \tag{3.38}$$

where $\boldsymbol{H}_{ij}^{\mathrm{S}} = \boldsymbol{H}_{ij}\{\boldsymbol{X}^{\mathrm{S}}(\theta_i - \phi_i), \boldsymbol{X}^{\mathrm{S}}(\theta_j^* - \phi_j)\}$ and θ_j^* is a contacting point with θ_i.

The solution, phase sensitivity function, and cell–cell interaction function are expanded to a Fourier series. Solution $U^{\mathrm{S}}(\theta)$ is an even function because we assume that the steady state solution conforms to a unimodal distribution and the peak of the distribution corresponds to $\theta = 0$. Therefore,

$$U^{\mathrm{S}}(\theta) = \sum_{k=-\infty}^{\infty} u_k \cos k\theta. \tag{3.39}$$

In the following calculations, $U_0^{(i)}(\theta_i)$ as $U^{\mathrm{S}}(\theta)$ of cell i are determined. Next, the phase sensitivity is expanded. The Fourier series is given by

$$Z_0^{(U)}(\theta) = \sum_{k=-\infty}^{\infty} -z_k \sin k\theta. \tag{3.40}$$

At last, function $S_{ij}(\theta + \eta_{ij})$ describing cell–cell interaction is symmetrical with $\theta = 0$, then

$$S_{ij}(\theta + \eta_{ij}) = \sum_{k=-\infty}^{\infty} s_k^{(ij)} \cos k\theta. \tag{3.41}$$

Substituting these series into the phase model,

$$\begin{aligned}
\dot{\phi}_i &= \varepsilon \sum_{j \in A(i)} \left\langle Z_0^{(U)}(\theta_i - \phi_i), S(\theta_i - \eta_{ij}) \cdot \left(U_0^{(j)}(\theta_j^* - \phi_j) - U_0^{(i)}(\theta_i - \phi_i) \right) \right\rangle \\
&= \varepsilon \sum_{j \in A(i)} \int_0^{2\pi} \sum_{k=-\infty}^{\infty} -z_k \sin k(\theta_i - \phi_i) \cdot \sum_{l=-\infty}^{\infty} s_l^{(ij)} \cos l\theta_i \cdot \\
&\quad \left(\sum_{m=-\infty}^{\infty} u_m \cos m(\pi + 2\eta_{ij} - \theta_i - \phi_j) - \sum_{m=-\infty}^{\infty} u_m \cos m(\theta_i - \phi_i) \right) d\theta_i.
\end{aligned} \tag{3.42}$$

From this equation, the following is obtained:

$$\Gamma_{ij} = 2\pi \sum_{k,l} z_k u_l \left[(-1)^l s_{l-k}^{(ij)} \sin\{(k+l)\eta_{ij} - k\phi_i - l\phi_j\} - s_{k+l}^{(ij)} \sin\{(k+l)(\eta_{ij} - \phi_i)\} \right]. \tag{3.43}$$

For the regular and elongated hexagonal cell shapes, it can be seen

$$s_k^{(ij)} = \frac{1}{k\pi} \sin \frac{k d_{ij}}{2} \ (k \neq 0), \tag{3.44}$$

$$s_0^{(ij)} = \frac{d_{ij}}{2\pi}. \tag{3.45}$$

Coefficients u_k and z_k are obtained for a given model.
For the GLE, the phase reduction is performed analytically. In Section 3.1.1, the solution of GLE is given by

$$\boldsymbol{X}^{\mathrm{S}} = (U^{\mathrm{S}}, V^{\mathrm{S}}) = \sqrt{1 - D_0} \begin{pmatrix} \cos\theta \\ \sin\theta \end{pmatrix} \tag{3.46}$$

and thus

$$\boldsymbol{Y}_0 = \left(-\frac{dU^{\mathrm{S}}}{d\theta}, -\frac{dV^{\mathrm{S}}}{d\theta} \right) = \sqrt{1 - D_0} \begin{pmatrix} \sin\theta \\ -\cos\theta \end{pmatrix}. \tag{3.47}$$

Furthermore, by solving $\mathcal{L}^\dagger \boldsymbol{Z}_0 = 0$ with normalization $\langle \boldsymbol{Z}_0, \boldsymbol{Y}_0 \rangle = 1$, where $\mathcal{L}^\dagger = \mathcal{L}$ in the GLE, the following is obtained:

$$\boldsymbol{Z}_0 = \begin{pmatrix} Z_0^{(U)} \\ Z_0^{(V)} \end{pmatrix} = \frac{1}{2\pi\sqrt{1 - D_0}} \begin{pmatrix} \sin\theta \\ -\cos\theta \end{pmatrix} \tag{3.48}$$

Functions $\boldsymbol{X}^{\mathrm{S}}$ and $\boldsymbol{Z}_0$ are displayed in Fig. 3.4. If the U variable is perturbed upward at $\theta = \pi/2$, ϕ will increase because $Z_0^{(U)}(\pi/2) > 0$, i.e., the pattern will eventually shift right.

Note that $\boldsymbol{Z}_0$ is proportional to $\boldsymbol{Y}_0$ in the GLE because the linear operator is self-adjoint, i.e., $\mathcal{L}^\dagger = \mathcal{L}$, in this particular model. Note also that the expressions for all the other eigenfunctions are known [35] although only the expressions for $\boldsymbol{Z}_0$ and $\boldsymbol{Y}_0$ are required here.

Therefore, Eq. (3.35) with Eq. (3.43) is reduced to

$$\dot{\phi}_i = \varepsilon \sum_{j \in A(i)} \left\{ a_{ij} \sin(\phi_j - \phi_i) + b_{ij} \sin 2(\eta_{ij} - \phi_i) + c_{ij} \sin(2\eta_{ij} - \phi_i - \phi_j) \right\}, \tag{3.49}$$

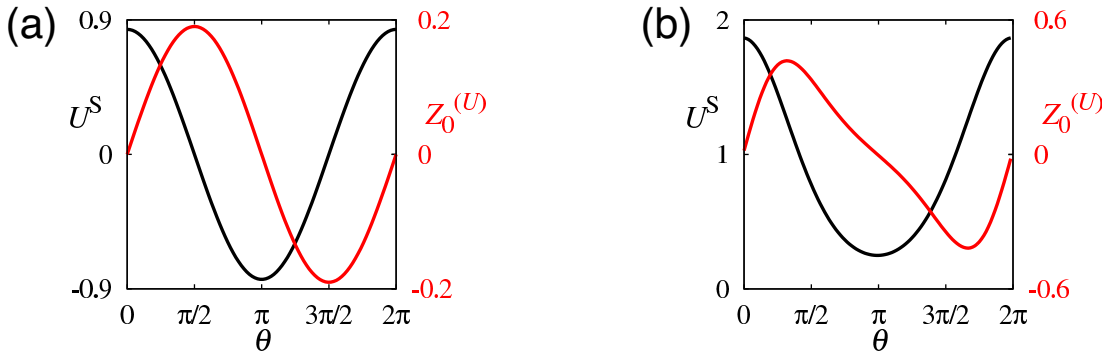

Figure 3.4: The profile of steady state $U^{\mathrm{S}}(\theta)$ (black lines) and phase sensitivity function $Z_0^{(U)}(\theta)$ (red lines) for (a) the GLE and (b) the activator–inhibitor model.

where

$$a_{ij} = b_{ij} = \frac{\sin d_{ij}}{4\pi}, c_{ij} = \frac{d_{ij}}{4\pi}. \tag{3.50}$$

Nevertheless, for most models, the phase reduction is performed numerically by solving Eq. (3.1) for $\varepsilon = 0$ and its adjoint equation $\dot{\boldsymbol{Z}}_0 = \mathcal{L}^\dagger \boldsymbol{Z}_0$ with $\langle \boldsymbol{Z}_0, \boldsymbol{Y}_0 \rangle = 1$ [23]. For the activator–inhibitor model, U^{S} and $Z_0^{(U)}$ are obtained, as presented in Fig. 3.4(b).

If the solution of the model is assumed to have a simple unimodal distribution, the Fourier series expansion of a steady state solution and the phase sensitivity function only up to mode 1 satisfy the phase model. We also derive the phase model via the general activator–inhibitor model. The model in Eq. (3.4) serves as an example. Fourier coefficients are approximately formulated as $u_0 = 0.925, u_1 = 0.397, u_2 = 0.065, z_1 = -0.180$, and $z_2 = -0.062$, and the rest of the coefficients are negligibly small if we expand the solution and phase sensitivity function of the Meinhardt model to a Fourier series. We obtain Γ_{ij} by substituting these values into Eq. (3.43). If we replace each function with a Fourier series and expand it, then this phase model becomes

$$\begin{aligned}
\dot{\phi}_i = -4\pi\varepsilon\{ & z_1 u_1 s_2^{(ij)} \sin(\phi_j - \phi_i) + z_1 u_1 s_2^{(ij)} \sin 2(\eta_{ij} - \phi_i) + z_1 u_1 s_0^{(ij)} \sin(2\eta_{ij} - \phi_i - \phi_j) \\
& + z_2 u_1 s_1^{(ij)} \sin(3\eta_{ij} - 2\phi_i - \phi_j) + z_2 u_1 s_1^{(ij)} \sin(\eta_{ij} - \phi_i) + z_2 u_1 s_3^{(ij)} \sin(\eta_{ij} - 2\phi_i + \phi_j) \\
& + z_2 u_1 s_3^{(ij)} \sin 3(\eta_{ij} - \phi_i) - z_1 u_2 s_1^{(ij)} \sin(3\eta_{ij} - \phi_i - 2\phi_j) - z_1 u_2 s_1^{(ij)} \sin(\eta_{ij} - \phi_i) \\
& + z_1 u_2 s_3^{(ij)} \sin(\eta_{ij} + \phi_i - 2\phi_j) + z_1 u_2 s_3^{(ij)} \sin 3(\eta_{ij} - \phi_i) \\
& - z_2 u_2 s_0^{(ij)} \sin(4\eta_{ij} - 2\phi_i - 2\phi_j) - z_2 u_2 s_4^{(ij)} \sin 2(\phi_j - \phi_i) - z_2 u_2 s_4^{(ij)} \sin 4(\eta_{ij} - \phi_i) \ \cdots \}.
\end{aligned} \tag{3.51}$$

Next, the phase equation is obtained as follows when we calculate only the lower order.

$$\begin{aligned}
\dot{\phi}_i \simeq \varepsilon \{ & \, 0.124 \sin(\phi_j - \phi_i) + 0.124 \sin 2(\eta_{ij} - \phi_i) + 0.150 \sin(2\eta_{ij} - \phi_i - \phi_j) \\
& + 0.049 \sin(3\eta_{ij} - 2\phi_i - \phi_j) + 0.049 \sin(\eta_{ij} - \phi_i) + 0.033 \sin(\eta_{ij} - 2\phi_i + \phi_j) \\
& + 0.033 \sin 3(\eta_{ij} - \phi_i) - 0.0234 \sin(3\eta_{ij} - \phi_i - 2\phi_j) - 0.0234 \sin(\eta_{ij} - \phi_i) \\
& + 0.0156 \sin(\eta_{ij} + \phi_i - 2\phi_j) + 0.0156 \sin 3(\eta_{ij} - \phi_i) \\
& - 0.008 \sin(4\eta_{ij} - 2\phi_i - 2\phi_j) - 0.003 \sin 2(\phi_j - \phi_i) - 0.003 \sin 4(\eta_{ij} - \phi_i) \, \} . \quad (3.52)
\end{aligned}$$

As we can see in the above equation, the coefficients of up to mode 1 are greater than the others. Therefore, if coefficients with small values are ignored, then there is little or no effect on the behavior of the system.

In that case, the phase equation is given by

$$\begin{aligned}
\Gamma_{ij} &= 2\pi \sum_{k,l=-1}^{1} z_k u_l \left[(-1)^l s_{l-k}^{(ij)} \sin\{(k+l)\eta_{ij} - k\phi_i - l\phi_j\} - s_{k+l}^{(ij)} \sin\{(k+l)(\eta_{ij} - \phi_i)\} \right] \\
&= -4\pi z_1 u_1 \left\{ s_2^{(ij)} \sin(\phi_j - \phi_i) + s_2^{(ij)} \sin 2(\eta_{ij} - \phi_i) + s_0^{(ij)} \sin(2\eta_{ij} - \phi_i - \phi_j) \right\} . \quad (3.53)
\end{aligned}$$

Fig. 3.5 shows the result of comparing the reaction–diffusion model and phase model. Symbols were obtained from the reaction–diffusion models described by Eqs. (3.1), (3.3), and (3.4). Solid lines were obtained from the phase models given by Eqs. (3.35) with correspondence to Γ_{ij}. We confirmed the accuracy of the reduction theory for both the GLE and the activator–inhibitor models even when we consider a phase model only by multiplying low-order terms. Here, for the reaction–diffusion models, phase $\phi_i(t)$ was numerically determined as follows. First, the first Fourier component of $U_i(\theta, t)$ was calculated as

$$\hat{U}_i(t) = \frac{1}{2\pi} \int_0^{2\pi} U_i(\theta, t) e^{-\mathrm{i}\theta} d\theta. \quad (3.54)$$

After that, phase $\phi_i(t)$ was expressed as the solution to

$$\hat{U}_i(t) = C(t) e^{-\mathrm{i}\phi_i(t)}, \quad (3.55)$$

where $C(t) \geq 0$ and $\phi_i(t)$ are real. In this way, $\theta_i = \phi_i(t)$ approximately coincides with the maximum of $U_i(\theta_i)$ when $U_i(\theta_i)$ is nearly harmonic because

$$U_i(\theta_i, t) \approx C(t) \cos(\theta_i - \phi_i(t)). \quad (3.56)$$

At the end of this section, we interpret the characteristics of each term of

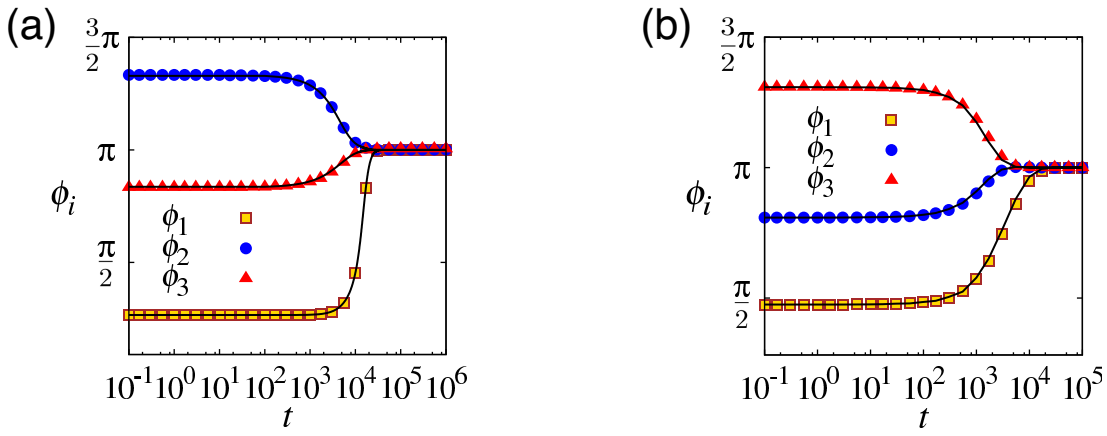

Figure 3.5: A comparison between the time series obtained from the reaction–diffusion models (symbols) and the corresponding phase models (lines). (a) The GLE. (b) An activator–inhibitor model. In this case, three regular hexagonal cells are aligned in a row, i.e., $\eta_{12} = \eta_{23} = 0$, $\eta_{21} = \eta_{32} = \pi$, $a_{ij} = b_{ij} = \frac{\sin d_{ij}}{4\pi} = \frac{\sqrt{3}}{8\pi}$, $c_{ij} = \frac{d_{ij}}{4\pi} = \frac{1}{12}$ and $\varepsilon = 0.001$ in Eq. (3.49).

Eq. (3.53). In our phase model, the first term resembles a spin model such as the XY model, and other terms include the information on positional relation η_{ij} between cell i and adjacent cell j. In the first term, the model tends to simply align the phase with that of adjacent cells. If it is assumed that the system is in phase between adjacent cells, i.e., $\phi_i, \phi_j = \phi^*$, then this ϕ^* depends on the initial condition, and ϕ^* takes values from 0 to 2π. In the second term, the phase is aligned to the direction of the adjacent cells. In the third term, there is an attempt to align the phase to the average of own phase and phases of adjacent cells to be oriented in cell-to-cell direction η_{ij}. Therefore, in our model, the cell phase not only can align to the adjacent cells' phase simply but also determines the direction of the alignment. Note that if either of b_{ij} or c_{ij} is nonvanishing, then the in-phase state even with a particular ϕ^* value does not exist except for special networks such as a straight chain. Our phase model Eq. (3.49) can surprisingly not only align to the adjacent cells' phase just as the XY model can but also determine the direction of the alignment. In another study, various functions such as the global concentration gradient or artificial energy function were added into the model so that polarity of all cells can be aligned in a certain direction. Fortunately, we succeeded in deriving the phase model that includes terms that determine the direction of the cell alignment naturally according to the phase reduction theory applied to the reaction–diffusion model with a cell–cell interaction term. In the text that follows, we investigate the dynamics of polarity using the phase model that is calculated up to mode 1 of a Fourier series.

Chapter 4

The dynamical properties of the polar model

Although the phase model derived from the reaction–diffusion model with a cell–cell interaction is much simpler than the original model, it well describes the polarity dynamics. In this chapter, we use the phase model derived from the GLE (Eq. (3.49)) and introduce the dynamical properties of cell polarity. The reason this model was chosen is that it enables us to analytically obtain the solution and phase sensitivity function of the reaction–diffusion model of the GLE. Basically, the polarity dynamics introduced here do not depend on the models under consideration.

While studying the phase model, we found that the direction of cell polarity varies depending on the cell deformation, system shape of the boundary, and interaction strength on each side shared by adjacent cells [30]. Additionally, more noise and effects of a global concentration gradient can be added to the reaction–diffusion model and can also suppose the case where there is a defective region in the system. Even though our model is very simple, complicated phenomena that are reproduced in the model of Amonlirdviman et al. can be easily reproduced by the new phase model.

4.1 Oriented polarity of two cells

Now we analyze by using the newly derived phase model. First, as the simplest system, we consider a system where two cells adhered to each other. The phase model to be applied is Eq. (3.49) derived from the GLE, and cells are regular hexagons with perimeter 2π. Please note that the results of the subsequent analysis are consistent with any model. Please also keep in mind that the results

of subsequent analyses are consistent with the models.

$$\dot{\phi}_i = \varepsilon \sum_{j \in A(i)} \{a_{ij} \sin(\phi_j - \phi_i) + b_{ij} \sin 2(\eta_{ij} - \phi_i) + c_{ij} \sin(2\eta_{ij} - \phi_i - \phi_j)\}$$

where

$$a_{ij} = b_{ij} = \frac{\sin d_{ij}}{4\pi}, \quad c_{ij} = \frac{d_{ij}}{4\pi}. \tag{4.1}$$

The directions of polarity of two cells are shown in Fig. 3.2(c)(d). In that case, cell arrangements of both Fig. 3.2(c) and (d) satisfy

$$\eta_{12} = \eta,\ \eta_{21} = \eta + \pi,\ a_{12} = a_{21} = a,\ b_{12} = b_{21} = b,\ c_{12} = c_{21} = c, \tag{4.2}$$

hence, the phase equations obey

$$\dot{\phi}_1 = \varepsilon \{a \sin(\phi_2 - \phi_1) + b \sin 2(\eta - \phi_1) + c \sin(2\eta - \phi_1 - \phi_2)\}, \tag{4.3}$$
$$\dot{\phi}_2 = \varepsilon \{a \sin(\phi_1 - \phi_2) + b \sin 2(\eta + \pi - \phi_2) + c \sin(2\eta - \phi_2 - \phi_1)\}. \tag{4.4}$$

If the in-phase solution is set to $(\phi_1, \phi_2) = (\phi^*, \phi^*)$,

$$\dot{\phi}^* = \varepsilon(b + c) \sin 2(\eta - \phi^*). \tag{4.5}$$

Therefore, the steady state in-phase solution is given by

$$\phi^* = \eta + n\pi, \quad \eta + \frac{n\pi}{2} \quad (n \in \mathbb{Z}). \tag{4.6}$$

According to these results, the cell polarity is ordered in the direction parallel or perpendicular to the direction in which the cells are arranged. To find out whether it is a stable solution, we take $\xi = \phi_1 + \phi_2$ and $\zeta = \phi_1 - \phi_2$ and apply linear stability analysis. From Eqs. (4.3) and (4.4), we obtain

$$\dot{\xi} = -2\varepsilon(b \cos\zeta + c) \sin\xi, \tag{4.7}$$
$$\dot{\zeta} = -2\varepsilon(a + b \cos\xi) \sin\zeta. \tag{4.8}$$

Introducing $\Delta\xi = \xi - 2\phi^*$ and linearizing Eqs. (4.7) and (4.8) for small $\Delta\xi$ and ζ, we obtain

$$\dot{\Delta\xi} = -2\varepsilon(b + c)(\cos 2\phi^*)\Delta\xi, \tag{4.9}$$
$$\dot{\zeta} = -2\varepsilon(a + b \cos 2\phi^*)\zeta. \tag{4.10}$$

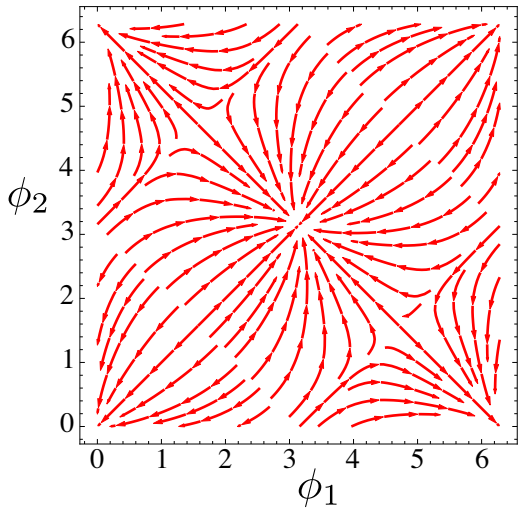

Figure 4.1: A phase diagram of ϕ_1 and ϕ_2 of the case in Fig. 3.2(d). We can see that the stable in-phase solutions are $\phi^* = 0, \pi$.

The solution

$$(\phi_1, \phi_2) = (\eta + n\pi, \eta + n\pi) \quad (n \in \mathbb{Z}) \tag{4.11}$$

is thus linearly stable when

$$\varepsilon(a + b) > 0 \text{ and } \varepsilon(b + c) > 0. \tag{4.12}$$

The GLE also satisfies this condition. In this case, solution $\phi^* = \frac{n\pi}{2}$ $(n \in \mathbb{Z})$ is unstable. Therefore, it was confirmed easily that the case where the polarity oriented in the direction of cell alignment is stable. In addition, the following diagram Fig. 4.1 helps us to understand the relation of solutions of ϕ_1 and ϕ_2.

Similarly, when N cells are aligned in a certain direction, it is possible to analytically calculate the direction in which polarity is oriented. If it is assumed that all cells are in phase in the system, that is to say, the system satisfies $\phi_i = \phi^*$ $(i = 1, \cdots, N)$, we can confirm that the polarity is oriented toward the direction of cell alignment by applying the Gershgorin circle theorem to the corresponding stability matrix of the phase model.

In addition to the first term like the XY model in the phase model described by Eq. (3.49), it is a characteristic feature of the proposed model that it includes the second and third terms expressing the positional information for adjacent cells. Due to these terms, the cell polarity can be aligned in a certain direction without a global concentration gradient or any other conditions.

4.2 Dependence on the shape of cells and the system boundary

In the previous section, we found that the direction of cell polarity is aligned in the direction of the cell adhesion surface when the cells are aligned in a line, according to the numerical calculation and analysis. We next discuss the dynamics of a two-dimensional system packed with cells. How is the polarity aligned when cells are arranged as a two-dimensional sheet? Moreover, is there any effect on the direction of polarity if the cells are elongated? As answers to these questions, it was found that the direction of polarity varies depending on the shape of cells and the system boundary. The cell polarity is aligned in the direction of the boundary of the system when cells interact isotropically, and it is aligned vertically in the cell elongation direction when the length of the contact surface with adjacent cells varies depending on the site.

At this point, a calculation is performed. We consider the case where the polarity is ordered. The case is assumed where the phase of each cell takes close values in the whole system, and the condition $\phi_i = \phi_j$ (i.e., the in-phase state) between adjacent cells is satisfied. In Eq. (3.49), the term corresponding to the XY model (the term where a_{ij} is a coefficient) vanishes, and the model can be reduced to only terms related to the positional information η when $\phi_i = \phi_j$. Hence,

$$\dot{\phi}_i = \varepsilon R_i \sin 2(\overline{\eta_i} - \phi_i), \tag{4.13}$$

where $R_i > 0$ and $\overline{\eta_i} \in \mathbb{R}$ are determined by

$$R_i e^{\mathrm{i}2\overline{\eta_i}} = \sum_{j \in A(i)} (b_{ij} + c_{ij}) e^{\mathrm{i}2\eta_{ij}}. \tag{4.14}$$

This measuring method is similar to Kuramoto's order parameter. R_i and η_i can be interpreted as effective strength and preferred direction of the net interactions of cell i, respectively. The larger the value of R_i, the more readily is the polarity aligned in the direction of η_i. For hexagonal lattices with each cell shape being regular hexagonal, R_i vanishes for cell i not facing boundaries of the lattice because b_{ij} and c_{ij} are not i, j-dependent and η_{ij} takes the values $0, 2\pi/n, 4\pi/n, \cdots, 2(n-1)\pi/n$ at $n = 6$. As shown in the first row in Fig. 4.2, cells inside the system are adhere to adjacent cells in all directions. In this situation, the phase equations for the interior of cells are $\dot{\phi}_i = 0$ if the cell shape has axial symmetry. Even if the shape is not a regular hexagon, the relation holds for polygonal cells with a symmetrical shape. When the cell shape is a square,

similar results can be obtained by putting in parameters $\eta_{ij} = 0, \pi/2, \pi, 3\pi/2$ and $d_{ij} = \pi/2$. When such $R_i = 0$, the phase equation vanishes and the polarity direction cannot be determined in a specific direction, which is similar to the case of the XY model. In the case of open boundary, cells on the boundary define the direction of polarity. They do not adhere to another cell on some side, and R_i is nonvanishing; thus, $\overline{\eta_i}$ is approximately parallel to the boundary line as depicted in Fig. 4.2. As an exception, in the case of a special cell arrangement, R_i vanishes even if the cell is on the boundary. The phase equation when $\eta_{ij} = \eta$ is identical to the equation when $\eta_{ij} = \eta + \pi$. Then, the cell shape is a regular hexagon, the sum of equations whose η_{ij} is 0, $\pi/3$ and $2\pi/3$ or π, $4\pi/3$, $5\pi/3$ becomes zero. Therefore, the various patterns of cell arrangement are replaced with a simple cell arrangement.

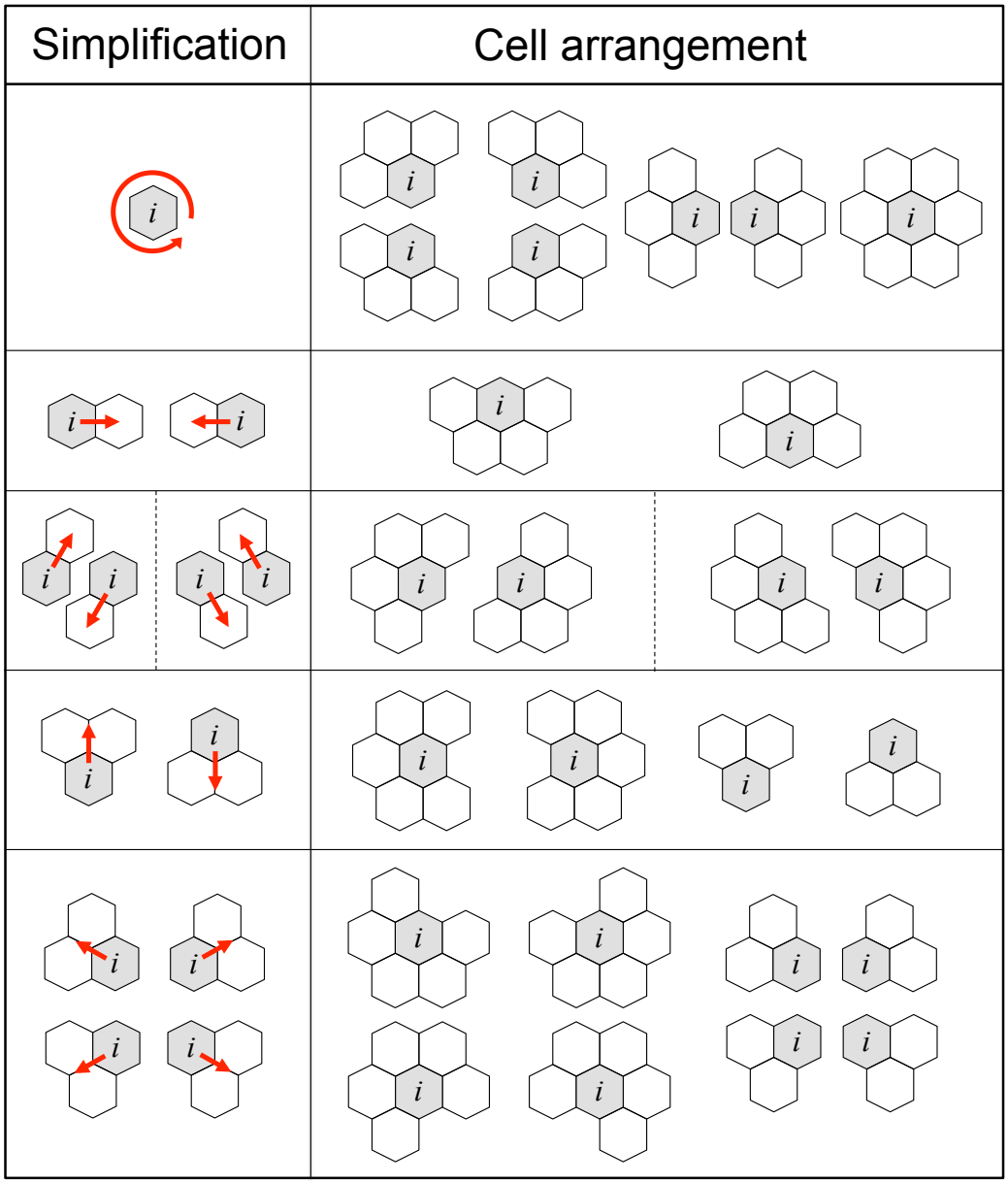

Figure 4.2: Illustration of the arrangement pattern of cell i and its adjacent cells. The "Cell arrangement" column shows the pattern of the main cell arrangement. The "Simplification" column represents a simple cell arrangement that shows the same result as the steady state solution of the phase equation for cell i. The red arrows indicate the direction in which the polarities are oriented.

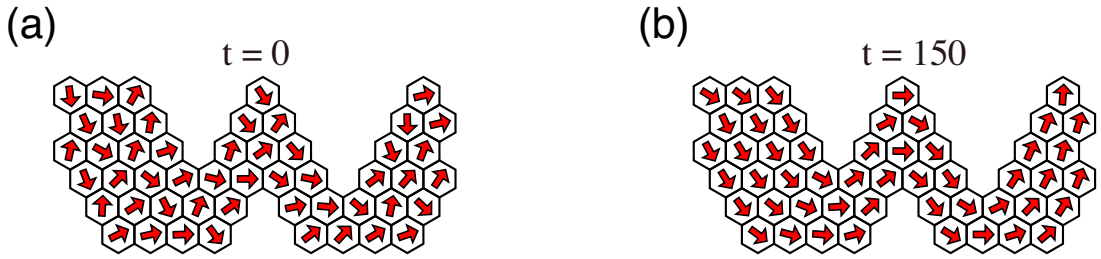

Figure 4.3: The polarity pattern for winding cell alignment with a regular hexagonal shape, obtained numerically with the phase model given by equation (3.49). (a) Initial and (b) final patterns. Each arrow indicates the phase of each cell.

Therefore, the first polarity of cells on the boundary tends to be ordered in the direction of the rows adhering to adjacent cells, and then the information about the polar direction determined by the cells on the boundary is transmitted sequentially to the cells inside the system. Fig. 4.3 shows how cell polarity is aligned in a winding system. Initial conditions were taken randomly from uniform distribution $\left(-\frac{\pi}{2}, \frac{\pi}{2}\right)$ so that no topological defects appeared. It can be seen that the polarity is aligned along the boundary shape.

When the cell shape is elongated, R_i is nonvanishing even in the case of cells inside the system. This is because the length of each side of the hexagon changes with the deformation of cell shape, and the values of b_{ij}, c_{ij} and η_{ij} vary depending on the site. In this case, $\overline{\eta_i}$ tends to get oriented toward the direction of a contact surface with greater width. When the number of bulk units is much greater than that of boundary units, polarity orientation is predominantly dependent on the cell shape. In particular, when the cell shape is uniformly elongated as that depicted in Fig. 3.1(a), stability analysis is straightforward. In this scenario, Eq. (4.13) is reduced to

$$\dot{\phi}_i = -2\varepsilon\lambda \sin 2\phi_i, \tag{4.15}$$

where

$$\lambda = \frac{\sin\delta}{4\pi} + \frac{\delta}{4\pi} - 2\left(\frac{\sin(\frac{\pi-\delta}{2})}{4\pi} + \frac{\pi-\delta}{8\pi}\right)\sin\frac{\delta}{2}. \tag{4.16}$$

Thus, the stability depends on the sign of λ. For $\lambda > 0$ ($\lambda < 0$), which is the case for $d > \frac{\pi}{3}$ ($d < \frac{\pi}{3}$), the states $\phi_i = 0$ or $\phi_i = \pi$ ($\phi_i = \frac{\pi}{2}$ or $\phi_i = -\frac{\pi}{2}$) for all i are stable. Hence, the polarities of vertically and horizontally elongated cells are aligned in the lateral and longitudinal direction, respectively, because $d = \frac{\pi}{3}$ when the cell is a regular hexagon. For $\lambda = 0$, which is true for $d = \frac{\pi}{3}$, ϕ_i dynamics becomes neutral, and the steady state is determined by initial conditions.

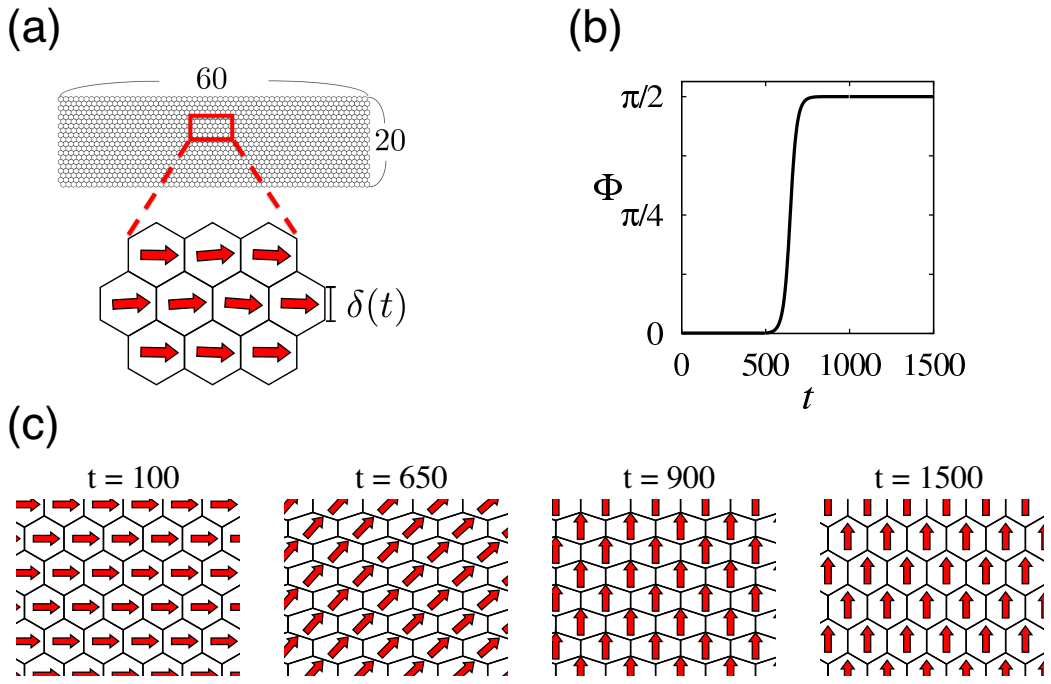

Figure 4.4: The polarity pattern for a planar alignment in a periodic system of 60×20 cells, obtained numerically via the phase model described by Eq. (3.49). In panel (a), the initial cell shape (regular hexagonal, $\delta(0) = \frac{\pi}{3}$) and initial phases are displayed. In panel (b), the time series of the mean phase $\Phi(t)$ are depicted. When cells are elongated at $t = 500$, the direction of cell polarity changes immediately. After the polarity is oriented vertically in the direction of cell elongation, $\Phi(t)$ does not change even if we reset the cell shape to a regular hexagon. In panel (c), snapshots are presented. Initial conditions were taken randomly from a uniform distribution $(-0.5, 0.5)$ so that no topological defects appear in the patterns.

To clearly demonstrate the effect of cell elongation, we consider a two-dimensional periodic system shown in Fig. 4.4. Initially, we set the cell shapes to regular hexagons. Because the boundary effects are negligibly small for the periodic boundary condition under consideration, phases can be aligned with arbitrary values determined by initial conditions. Here we employ a random initial condition, where phases are chosen from a uniform distribution within the range $(-0.5, 0.5)$. Mean phase $\Phi(t)$ of $N = 60 \times 20$ cells in the system and order parameter $Q(t)$ at time t are expressed as follows:

$$Q(t)e^{\mathrm{i}\Phi(t)} = \frac{1}{N}\sum_{j} e^{\mathrm{i}\phi_j(t)} \tag{4.17}$$

where $\Phi \in \mathbb{R}$. Here, $Q \geq 0$ vanishes when the system is disordered, and $Q = 1$ when the system is completely ordered. Cells are elongated only for

$500 \leq t < 1000$ when $\delta(t) = \frac{\pi}{3} - \frac{\pi}{10}$; otherwise $\delta(t) = \frac{\pi}{3}$. At $t = 100$, phases are almost perfectly aligned at $\phi_i \approx 0$, which is approximately the average of the initial phases. At $t = 500$, the cell shape to be elongated is changed. Then, cell polarity is aligned upward, pointing in the direction of a contact surface with greater width, as predicted above. According to this result, the cells are aligned towards a larger bonded surface with adjacent cells when the interaction intensity is isotropic. This polarity pattern is maintained even when the cell shape is returned to regular hexagonal ($t > 1000$). The reason why the direction of polarity does not change when cell shape is returned to regular hexagonal is that R_i approaches zero as the length of the adherent surface becomes isotropic, and the polarity can be oriented in an arbitrary direction. This phenomenon, i.e., when the polar direction changes due to cell elongation and keeps the direction even if cell shape returns to regular hexagonal is actually obtained in the polarity experiment on *Drosophila* wings. When actual cells are elongated, some cells divide, and new bonded edges perpendicular to the direction of cell elongation are generated. While the cell division is repeated, the sides that have existed for a long time become distributed more along the direction parallel to the cell elongation, and the intercellular binding strengthens in this region as well. Therefore, a PCP protein accumulates on this long-standing side with strong bond strength, and it is expected that polarity forms along the strong bond direction. Actually, also in our model, we can obtain the similar results in the case where we change the intensity of cell–cell interaction on each side, and the anisotropy toward the cell adhesion surface is given. We discuss this situation in detail in the subsequent sections.

4.3 Dependence on the change in coupling strength

In the previous section, when the strength of a cell–cell interaction was isotropic, the polarity was aligned toward the long side of the cell adhesion surface. How is the polar direction oriented when the cell shape remains regular hexagonal and the strength of cell–cell interaction is changed by each side? We consider the situation in which coupling strength ε in our reaction–diffusion model described by Eq. (3.1) is i, j-dependent by replacing ε with $\varepsilon(1 + \alpha_{ij})$. The shapes of all cells in the system are fixed: regular hexagonal. Then, the corresponding phase

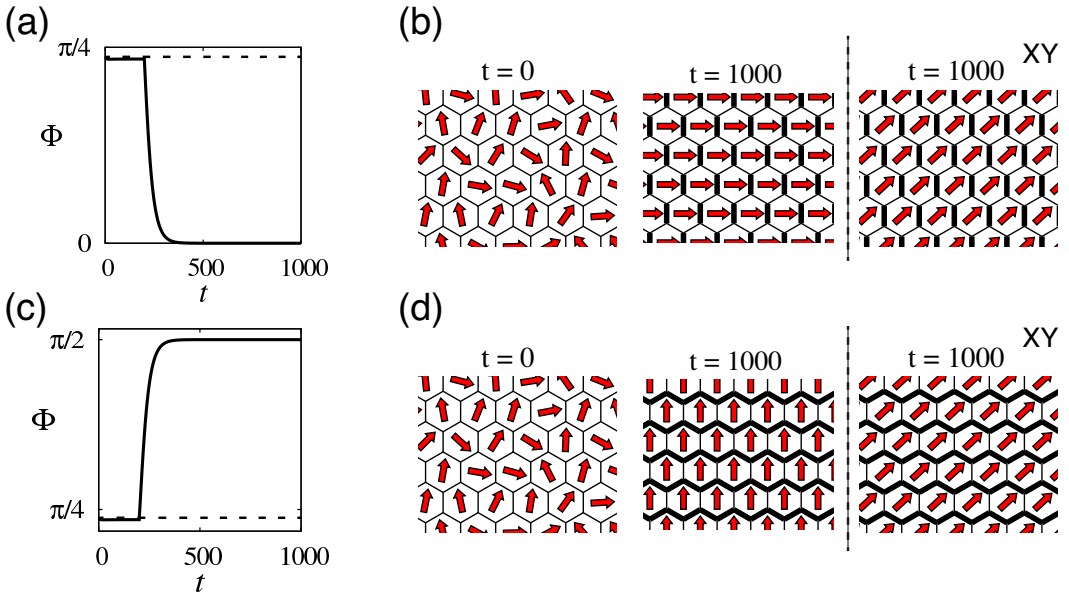

Figure 4.5: The polarity pattern in the system with diverse coupling strengths. The cell alignment is the same as that in Fig. 4.4 while cell shape is fixed: regular hexagonal. Coupling strengths are initially the same, i.e., $\alpha_{ij} = 0$ for $0 \leq t < 200$. For $t \geq 200$, we set $\alpha_{ij} = 0.1$ and -0.1 for the surfaces with $\eta_{ij} = 0, \pi$ in panels (a) and (b) and in panels (c) and (d), respectively; and $\alpha_{ij} = 0$ otherwise. Thus, the contacting surfaces depicted as thick lines have greater coupling strength. (a, c) A time series of mean phase $\Phi(t)$ obtained with the phase model formulated as Eqs. (3.49) (solid lines) and with its XY-model variant (dashed lines) in which b_{ij} and c_{ij} values are set to zero while $a_{ij} = \frac{\sqrt{3}}{8\pi}$ is unchanged. (b, d) Snapshots are displayed. The rightmost panels depict snapshots obtained with the XY-model variant. The same initial conditions were employed in all the cases.

model reads

$$\dot{\phi}_i = \varepsilon \sum_{j \in A(i)} (1 + \alpha_{ij}) \left\{ a \sin(\phi_j - \phi_i) + b \sin 2(\eta_{ij} - \phi_i) + c \sin(2\eta_{ij} - \phi_i - \phi_j) \right\}, \tag{4.18}$$

where $a = b = \frac{\sqrt{3}}{8\pi}$ and $c = \frac{1}{12}$. Under the assumption of an in-phase state, this equation is reduced to

$$\dot{\phi}_i = \varepsilon(b + c) \sum_{j \in A(i)} (1 + \alpha_{ij}) \sin 2(\eta_{ij} - \phi_i). \tag{4.19}$$

Now we introduce axial asymmetry such that only the surfaces along the vertical axis, which are depicted as thick lines in Fig. 4.5, have $\alpha_{ij} = \alpha$, and $\alpha_{ij} = 0$ for other surfaces. The coupling strength is greater in the lateral and zigzag vertical

direction when $\alpha > 0$ and $\alpha < 0$, respectively, as shown in Fig. 4.5 (b) and (d). In this case, we next obtain

$$\dot{\phi}_i = -2\varepsilon\alpha(b+c)\sin 2\phi_i. \tag{4.20}$$

Accordingly, the sign of α plays exactly the same role as that of λ in Eq. (4.15); the polarity pattern is aligned along the axis with stronger coupling. Numerical results are obtained by means of the phase model (Eq. (4.18)) with coupling diversity in Fig. 4.5. To highlight the effect of geometry-dependent terms, we also show results obtained using Eq. (4.18) with b and c being set to zero, corresponding to the XY model. Although cell polarity is reoriented by changes in the properties of individual cells in the phase model, the direction of polarity once aligned does not change even if the interaction strength between cells varies in the XY model. Therefore, the system's axial asymmetry under consideration affects dynamics only in the presence of geometry-dependent terms. Even when the cell shape is isotropic, we can easily confirm that the polarity is aligned toward the side with a strong interaction if the interaction strength with adjacent cells is different.

4.4 Noise and global concentration gradient

One of the advantages of our model is that one can analyze the ordering phenomena exemplified by actual *Drosophila* wings and mouse embryos by simply changing the functional form of the model slightly. Next, we set various interaction terms of the reaction–diffusion model and derive the phase model to investigate the dynamics of polarity. We first consider the presence of a global concentration gradient (as explained in another study [14]) and noise. The presence of a PCP protein distributed throughout the region where the concentration increases in a specific direction is known. Besides, the system is affected by noise such as cell division and generation and annihilation of cells. In our phase model, how is polarity aligned when such noise and global concentration gradient are added? If we take into account a global concentration gradient and noise, the reaction–diffusion model can be described as

$$\frac{\partial}{\partial t}\boldsymbol{X}_i = \boldsymbol{F}(\boldsymbol{X}_i) + \hat{D}\frac{\partial^2}{\partial\theta_i^2}\boldsymbol{X}_i + \varepsilon\sum_{j\in A(i)}\boldsymbol{H}_{ij} + \varepsilon_{\mathrm{e}}\boldsymbol{G}_i + \boldsymbol{p}_i, \tag{4.21}$$

where $\boldsymbol{G}_i = \boldsymbol{G}_i(\theta_i, t)$ is the external signal, ε_{e} is its strength, and $\boldsymbol{p}_i = (p_i^{(1)}(\theta,t), p_i^{(2)}(\theta,t), \ldots)$ is white Gaussian noise that satisfies $\mathrm{E}[p_i^{(m)}(\theta,t)] =$

0 and $\mathrm{E}[p_i^{(m)}(\theta,t)p_j^{(n)}(\theta',t')] = \nu_m\delta_{ij}\delta_{mn}\delta(\theta-\theta')\delta(t-t')$, with $\mathrm{E}[\cdot]$ representing the expected value, and ν_m is the noise intensity. For sufficiently small ε_e and ν_m, we carry on the same procedure as that for Eq. (3.1) to obtain

$$\dot{\phi}_i = \varepsilon \sum_{j\in A(i)} \Gamma_{ij}(\phi_i,\phi_j) + \varepsilon_\mathrm{e}\Pi_i(\phi_i,t) + q_i(t) \tag{4.22}$$

where

$$\Pi_i(\phi_i) = \langle \boldsymbol{Z}_0(\theta_i-\phi_i), \boldsymbol{G}_i(\theta_i,t)\rangle, \tag{4.23}$$

$$q_i(t) = \langle \boldsymbol{Z}_0(\theta_i-\phi_i), \boldsymbol{p}_i(\theta_i,t)\rangle. \tag{4.24}$$

Note that $q_i(t)$ is Gaussian white noise that satisfies

$$\mathrm{E}[q_i(t)] = 0, \quad \mathrm{E}[q_i(t)q_j(t')] = \nu\delta_{ij}\delta(t-t'), \tag{4.25}$$

where $\nu = \sum_m \nu_m \int_0^{2\pi} \left\{ Z_0^{(m)}(\theta) \right\}^2 d\theta$. Because

$$\mathrm{E}[q_i(t)] = \mathrm{E}\left[\int_0^{2\pi} \boldsymbol{Z}_0(\theta-\phi_i)\cdot\boldsymbol{p}_i(t)d\theta \right] \tag{4.26}$$

$$= \mathrm{E}\left[\int_0^{2\pi} \sum_m Z_0^{(m)}(\theta-\phi_i)p_i^{(m)}d\theta \right] \tag{4.27}$$

$$= \int_0^{2\pi} \sum_m Z_0^{(m)}(\theta-\phi_i)\mathrm{E}[p_i^{(m)}]d\theta \tag{4.28}$$

$$= 0, \tag{4.29}$$

and

$$\mathrm{E}[q_i(t)q_j(t')] = \mathrm{E}\left[\iint_0^{2\pi} \{\boldsymbol{Z}_0(\theta-\phi_i(t))\cdot\boldsymbol{p}_i(t)\}\{\boldsymbol{Z}_0(\theta'-\phi_j(t'))\cdot\boldsymbol{p}_j(t')\}d\theta d\theta'\right] \quad (4.30)$$

$$= \mathrm{E}\left[\iint_0^{2\pi} \left\{\sum_m Z_0^{(m)}(\theta-\phi_i(t))p_i^{(m)}(t)\right\}\left\{\sum_{m'} Z_0^{(m')}(\theta'-\phi_j(t'))p_j^{(m')}(t')\right\} d\theta d\theta'\right] \quad (4.31)$$

$$= \mathrm{E}\left[\iint_0^{2\pi} \sum_{m,m'} Z_0^{(m)}(\theta-\phi_i(t))p_i^{(m)} Z_0^{(m')}(\theta'-\phi_j(t'))p_j^{(m')}(t')d\theta d\theta'\right] \quad (4.32)$$

$$= \iint_0^{2\pi} \sum_{m,m'} Z_0^{(m)}(\theta-\phi_i(t))Z_0^{(m')}(\theta'-\phi_j(t'))\mathrm{E}\left[p_i^{(m)}(t)p_j^{(m')}(t')\right] d\theta d\theta' \quad (4.33)$$

$$= \iint_0^{2\pi} \sum_{m,m'} Z_0^{(m)}(\theta-\phi_i(t))Z_0^{(m')}(\theta'-\phi_j(t'))\nu_m\delta_{ij}\delta_{mm'}\delta(\theta-\theta')\delta(t-t')d\theta d\theta' \quad (4.34)$$

$$= \int_0^{2\pi} \sum_m \nu_m \left\{Z_0^{(m)}(\theta-\phi_i(t))\right\}^2 d\theta \quad (4.35)$$

$$= \sum_m \nu_m \int_0^{2\pi} \left\{Z_0^{(m)}(\theta)\right\}^2 d\theta. \quad (4.36)$$

In the case of the GLE, any generic choice of external signal $\boldsymbol{G}_i(\theta_i, t)$ yields

$$\Pi_i = c_i(t)\sin(\psi_i(t)-\theta_i) \quad (4.37)$$

because $\boldsymbol{Z}_0(\theta)$ contains only the first harmonics. As a simple example, we consider a unimodal distribution where the peak is at $\theta_i = \psi(t)$. Thus,

$$\boldsymbol{G}_i(\theta_i) = (\cos(\psi(t)-\theta_i), 0), \quad (4.38)$$

the following is obtained:

$$\Pi_i = \frac{1}{2\sqrt{1-D_0}}\sin(\psi-\theta_i). \quad (4.39)$$

The phase model in question is actually a gradient system, i.e.,

$$\dot{\phi}_i = -\frac{\partial}{\partial\phi_i}\mathcal{H} + q_i \quad (4.40)$$

with potential function $\mathcal{H} = \mathcal{H}(\{\phi_i\})$ given by

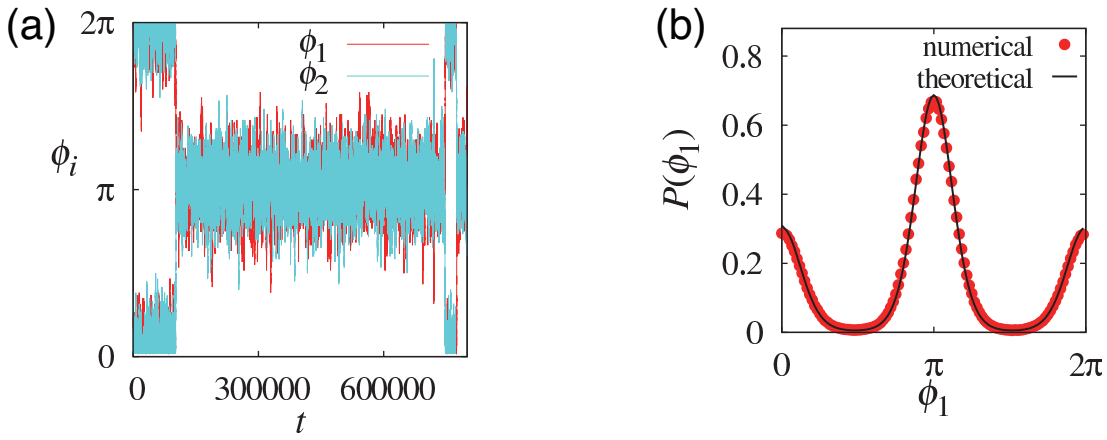

Figure 4.6: Polarity orientation for two coupled cells in the presence of an external signal and noise. (a) A time series. (b) The probability density function obtained numerically and theoretically.

$$\begin{aligned}\mathcal{H} &= -\frac{\varepsilon}{2}\sum_i \sum_{j\in A(i)} \{a_{ij}\cos(\phi_j-\phi_i) + b_{ij}\cos 2(\eta_{ij}-\phi_i) + c_{ij}\cos(2\eta_{ij}-\phi_i-\phi_j)\} \\ &\quad -\varepsilon_{\mathrm{e}}\sum_i \frac{1}{2\sqrt{1-D_0}}\cos(\psi-\theta_i). \end{aligned} \tag{4.41}$$

A probability distribution is obtained by solving the Fokker–Planck equation corresponding to the phase equation:

$$P(\{\phi_i\}) = C\exp\left[-\frac{2\mathcal{H}(\{\phi_i\})}{\nu}\right], \tag{4.42}$$

where C is the normalization constant. The dynamics of ordering when two cells are lined up are shown in Fig. 4.6. From analysis results so far, the polar direction is oriented at 0 or π when the cells line up, but when noise is applied, cell polarity is distributed in other directions too as depicted in Fig. 4.6(a). The red dots in Fig. 4.6(b) denote the probability distribution obtained numerically from the GLE, given by Eqs. (4.21) and (3.3). The solid line in Fig. 4.6(b) corresponds to the distribution function (Eq. (4.42)) obtained theoretically. We can see that this phase model can reproduce the dynamics of polarity well.

4.5 The effect of microtubules

Although the mechanism of global cell polarity formation has not been understood yet, some previous studies claim that the existence of microtubules is

related to polarity formation. In the study by Shimada et al. [31], they suggest that microtubules in cells are aligned in a certain direction, and PCP protein Fz is transported along them. Experiments have revealed that these microtubules align along the axis of cell elongation [36, 37, 38, 39]. Thus, the polar direction changes during deformation and elongation of the cell shape. In fact, cells in an epithelial sheet of *Drosophila* elongate along the PD axis, and it has been confirmed that microtubules are aligned toward that direction [31]. PCP proteins that are transported along the microtubules accumulate at the end of the microtubules. As a result, the polarity is aligned in the direction of microtubule alignment. Although few studies on the relation between microtubules and determination of polarity have been conducted since 2007, we analyzed how the polarity changes when the presence of microtubules in our model is assumed.

Assuming that microtubules are present in the cell, it is expected that the velocity of protein diffusion on a cell membrane varies depending on the site. In accordance with this consideration, we add to this model a perturbation term, $\boldsymbol{G}$, which is described by spatially dependent diffusion function $D(\theta)$. We use the Meinhardt model [21]. In Eq. (3.4), we set $\boldsymbol{X} = (U, V)$.

$$\boldsymbol{F} = \begin{pmatrix} \frac{\rho_U U^2}{(1+\kappa U^2)V_i} - \mu_U U + \sigma_U \\ \rho_V U^2 - \mu_V V, \end{pmatrix}, \ \hat{D} = \begin{pmatrix} D_U & 0 \\ 0 & D_V \end{pmatrix}, \ \boldsymbol{G} = \begin{pmatrix} \varepsilon_S \frac{\partial}{\partial \theta}\left(D(\theta)\frac{\partial U}{\partial \theta}\right) \\ 0 \end{pmatrix}. \tag{4.43}$$

where $\rho_U = 0.01, \rho_V = 0.02, \mu_U = 0.01, \mu_V = 0.02, \sigma_U = 0.0, \kappa = 0.0, D_U = 0.005$, and $D_V = 0.2$, respectively. We determine the diffusion function so that it has a fast and slow diffusion site with π symmetry,

$$D(\theta) = \sin^2(\theta - \Psi) + C$$

where $C > 0$ is constant. The phase equation is given by

$$\dot{\phi} = \varepsilon_S \left\langle Z_0^{(U)}(\theta;\phi), \frac{\partial}{\partial \theta}\left(D(\theta)\frac{\partial U}{\partial \theta}\right)\right\rangle. \tag{4.44}$$

Next, we expand this equation into a Fourier series as follows.

$$Z_0^{(U)}(\theta) = \sum_{n=-\infty}^{\infty} -z_n \sin n\theta, \tag{4.45}$$

$$U^S(\theta) = \sum_{n=-\infty}^{\infty} u_n \cos n\theta, \tag{4.46}$$

$$D(\theta;\Psi) = \frac{1}{2} - \frac{1}{2}\cos 2(\theta - \Psi) + C, \tag{4.47}$$

$$\frac{\partial U^S}{\partial \theta} = \sum_{n=-\infty}^{\infty} -n u_n \sin n\theta. \tag{4.48}$$

Hence,

$$\dot{\phi}_i = -\varepsilon_S \pi \sum_{n=-\infty}^{\infty} n(n+2) z_n u_{n+2} \sin 2(\phi_i - \Psi). \tag{4.49}$$

Consequently, the steady state solution of ϕ is

$$\phi^* = \Psi \pm \frac{\pi}{2} \tag{4.50}$$

when $\varepsilon_S > 0, u_k > 0, z_k < 0$. After this analysis, we found that the direction of the cell polarity gets aligned in the direction where the diffusion is fast because $D(\theta)$ takes its maximum at $\Psi \pm \frac{\pi}{2}$.

It is not clear how the speed of diffusion changes due to the presence of microtubules in actual cells. If it is assumed that flow is generated to absorb floating proteins at the tip of microtubules, the direction of cell polarity is aligned parallel to the microtubule alignment.

In addition to the above effect of the diffusion function, we insert a cell–cell interaction term into the model. The interaction function

$$\boldsymbol{H}_{ij}(\theta_i, t) = S_{ij}(\theta_i) \begin{pmatrix} U_i(\theta_i, t) - U_j(\theta_j^*, t) \\ 0 \end{pmatrix} \tag{4.51}$$

is added, then the phase model with variables expanded in the Fourier series is

expressed as follows.

$$\begin{aligned}
\dot{\phi}_i &= -\varepsilon_S \pi \sum_{n=-\infty}^{\infty} n(n+2) z_n u_{n+2} \sin 2(\phi_i - \Psi) \\
&\quad + 2\pi\varepsilon \sum_{j \in A(i)} \sum_{n=-\infty}^{\infty} \sum_{l=-\infty}^{\infty} z_n u_l \Big[\cos(l\pi) s_{l-n} \sin\{(n+l)\eta_{ij} - n\phi_i - l\phi_j\} \\
&\qquad\qquad - s_{n+l} \sin\{(n+l)(\eta_{ij} - \phi_i)\} \Big] \qquad (4.52) \\
&\simeq -\varepsilon_S \pi z_1 (u_1 + 3u_3) \sin 2(\phi_i - \Psi) \\
&\quad - 4\pi\varepsilon z_1 u_1 \sum_{j \in A(i)} \{ s_0 \sin(2\eta_{ij} - \phi_i - \phi_j) + s_2 \sin 2(\eta_{ij} - \phi_i) + s_2 \sin(\phi_j - \phi_i) \} \\
&\qquad\qquad (4.53)
\end{aligned}$$

where $u_k > 0,\ z_k < 0,\ s_k > 0,\ \varepsilon_S > 0,\ \varepsilon > 0$. Therefore, we found that the polarity is aligned in the direction where diffusion within the cell adhesion surface is fast.

4.6 Cell polarity of the system with defective cells

In epithelial tissue where cell polarity is formed, defective cells are sometimes detected. Amonlirdviman et al. analyzed cell polarity when some cells have a knockout of a certain PCP protein (Fz, Vang, or Dsh) in experimental and numerical analyses [5]. Fz localizes in the final hair growth direction, and Vang antagonizes Fz within the cell. Dsh is a transmembrane protein that binds to both Fz and Vang. When there are some Fz knockout cells in an epithelial sheet, it is reported that the final direction of cell alignment is the region of defective cells. In contrast, polarity is aligned away from defective cells when some region of the wing contains Vang knockout cells.

In their experiment on the *Drosophila* wing [5], they reported that when there are some Fz knockout cells in an epithelial sheet, the final direction of alignment of wild-type cells is the region of defective cells. On the other hand, the wild-type cells align away from the region where defective cells are present when Vang knockout cells are there. They not only conducted an experiment but also were able to reproduce those results by means of more than 10 reaction–diffusion equations that explain the behavior of each PCP protein in detail.

To reproduce the behavior of the system with defective cells as well as their model can, we add to a cell–cell interaction a term for the interaction between a

wild-type cell and a PCP protein knockout cell into the phase model. The derivation method is as follows. In the reaction–diffusion model (Eq. (3.1)) before application of the phase reduction method, variable U is the protein corresponding to Fz that localizes in the direction of hair growth. Because the variables U and V represent the concentration of a PCP protein, $U = 0$ in all the regions on cell membrane when Fz is knocked out. If Vang is knocked out in the cell, Fz is not inhibited by Vang hence the concentration of U on cell membrane increases. If Dsh is knocked out, Fz does not localize and instead is distributed uniformly; therefore, the concentration of U takes an average value everywhere. Here, we set C to the concentration of Fz in a defective cell in which a certain PCP protein was knocked out. The phase model is composed of two kinds of cell–cell interaction. One is cell–cell interaction of wild-type cells and the other is the interaction between wild-type and defective cells. Therefore, the equation becomes

$$\dot{\phi}_i = \varepsilon \left\langle Z_0^{(U)}(\theta_i - \phi_i), \sum_{j\in A(i)} S_{ij}\left(U_i^S(\theta_i - \phi_i) - U_j^S(\theta_j^* - \phi_j)\right) \right\rangle + \varepsilon \left\langle Z_0^{(U)}(\theta_i - \phi_i), \sum_{j\in K(i)} S_{ij}\left(U_i^S(\theta_i - \phi_i) - C\right) \right\rangle. \quad (4.54)$$

The first term of Eq. (4.54) represents the dynamics of interaction between two wild-type cells, and the second term represents the dynamics of interaction between a wild-type cell and defective cell. Suppose $A(i)$ and $K(i)$ denote the sets of wild-type and defective cells, respectively. As in Section 4.5, the model is expanded with a Fourier series.

$$\dot{\phi}_i = 2\pi\varepsilon \sum_{j\in A(i)} \sum_{k,l} z_k u_l \left[(-1)^l s_{l-k}^{(ij)} \sin\{(k+l)\eta_{ij} - k\phi_i - l\phi_j\} - s_{-k-l}^{(ij)} \sin\{(k+l)(\eta_{ij} - \phi_i)\}\right] + \varepsilon \sum_{j\in K(i)} \int_0^{2\pi} \sum_{k=-\infty}^{\infty} z_k e^{ik(\theta_i - \phi_i)} \sum_{n=-\infty}^{\infty} s_n e^{in(\theta_i - \eta_{ij})} \left(\sum_{l=-\infty}^{\infty} u_l e^{il(\theta_i - \phi_i)} - C\right) d\theta_i \quad (4.55)$$

$$\simeq -4\pi\varepsilon \sum_{j\in A(i)} \left[z_1 u_1 s_2^{(ij)} \sin(\phi_j - \phi_i) + 2 z_1 u_1 s_2^{(ij)} \sin 2(\eta_{ij} - \phi_i) + z_1 u_1 s_0^{(ij)} \sin(2\eta_{ij} - \phi_i - \phi_j)\right] -4\pi\varepsilon \sum_{j\in K(i)} z_1 s_1^{(ij)} (u_0 - C) \sin(\eta_{ij} - \phi_i). \quad (4.56)$$

Therefore, the stable solution ϕ_i^* is given as

$$\phi_i^* = \eta_{ij} \quad (\ u_0 > C\ ) \quad (4.57)$$

$$\phi_i^* = \eta_{ij} + \pi \quad (\ u_0 < C\ ) \quad (4.58)$$

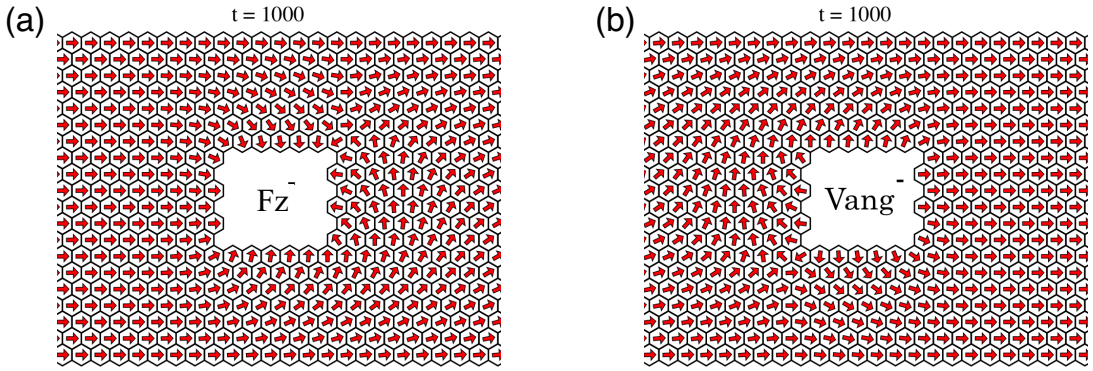

Figure 4.7: The results on cell polarity of a system with defective cells; the system is derived from Eq. (4.54). The original reaction–diffusion model involved the GLE. The phase was given randomly for the initial condition. The system is packed with 60×20 cells. In the area colored white, there are (a) Fz knockout cells and (b) Vang knockout cells.

because $-4\pi\varepsilon z_1 s_1^{(ij)} > 0$. The above result and Fig. 4.7 indicate that when the concentration of Fz in a defective cell is lower than that in a wild-type cell, the direction of alignment of wild-type cells is the region of defective cells; otherwise, the wild-type cells align away from the region containing defective cells. This conclusion is consistent with the experimental results, and the phase model makes it possible to reproduce the cell polarity as in the previous study even though a surprisingly simple model is compared with the previous one.

4.7 The robustness of cell polarity

We discuss the robustness of the results described above, i.e., their stability after changes in the model equations. The numerical simulations for regular hexagonal cell shapes were performed using Eq. (3.49) with $a_{ij} = b_{ij} = \frac{\sin d_{ij}}{4\pi}$ and $c_{ij} = \frac{d_{ij}}{4\pi}$ where $d_{ij} = \frac{\pi}{3}$. We have checked and confirmed that these results do not change qualitatively for small changes in a_{ij}, b_{ij}, c_{ij} values. A qualitative change is certainly expected when the stability condition described by Eq. (4.12) is violated.

We also noticed that there is no qualitative difference between the phase models reduced from the GLE and the activator–inhibitor model, as shown in Fig. 3.5. This observation suggests that higher harmonics in Γ_{ij} do not considerably affect the dynamics at least when they are small.

The types of coupling can also be considered in the reaction–diffusion model

that are different from those in Eq. (3.5). For example, we consider

$$\boldsymbol{H}_{ij}(\theta_i, t) = S_{ij}(\theta_i) \begin{pmatrix} -U_j(\theta_j^*, t) \\ 0 \end{pmatrix}, \tag{4.59}$$

which describes mutual inhibition as well as Eq. (3.5) does. By assuming that $U^{\mathrm{S}}(\theta)$ and $Z_0^{(U)}(\theta)$ are nearly harmonic, we approximately obtain

$$\dot{\phi}_i = \varepsilon \sum_{j \in A(i)} \left\{ a_{ij} \sin(\phi_j - \phi_i) + b'_{ij} \sin(\eta_{ij} - \phi_i) + c_{ij} \sin(2\eta_{ij} - \phi_i - \phi_j) \right\}, \tag{4.60}$$

where $a_{ij} = -4\pi z_1 u_1 s_2^{(ij)}$, $b'_{ij} = 4\pi z_1 u_0 s_1^{(ij)}$, $c_{ij} = -4\pi z_1 u_1 s_0^{(ij)}$. The phase model given by Eq. (4.60) is again a gradient system with the potential function given by

$$\mathcal{H} = -\frac{\varepsilon}{2} \sum_i \sum_{j \in A(i)} \left\{ a_{ij} \cos(\phi_j - \phi_i) + 2b'_{ij}(\eta_{ij} - \phi_i) + c_{ij} \cos(2\eta_{ij} - \phi_i - \phi_j) \right\}. \tag{4.61}$$

In the case of the GLE expressed as Eq. (3.3), we obtain $a_{ij} = \frac{\sin d_{ij}}{4\pi}$, $b'_{ij} = 0$, $c_{ij} = \frac{d_{ij}}{4\pi}$. Therefore, the only difference from the previous phase model given by Eq. (3.49) is the absence of the second term. It is straightforward to confirm that the absence of the second term in Eq. (3.49) does not change the presence and stability analysis performed above.

4.8 The phase model for any cell shape

Cell polarity dynamics was discussed under the assumption that the shape of cells is regular hexagonal or axially symmetrical. In the text below, we extend the model so that it is applicable to arbitrarily polygonal cells. From experiments, it is known that polygonal cells are distributed widely in the epithelial tissue space at an early stage of development, whereas hexagonal cells increase in number gradually by repeating cell division, disappearance, and migration; thus, eventually the epithelial sheet is packed with regular hexagonal cells [40].

Now we consider cell i with perimeter L_i and adjacent cell j with perimeter L_j (Fig. 4.8). The one-dimensional space coordinate along the circumference of cell i is set to l_i ($0 \leq l_i < L_i$). Cell i, j interacts with cell j, i at $l_i \in (a, b)$ and $l_j \in (c, d)$, respectively, as shown in Fig. 4.8. We determine the point that cell j

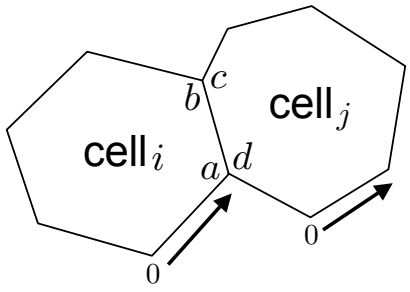

Figure 4.8: A schematic of various polygonal cell shapes.

contacts at l_i of cell i as l_j^* given by

$$l_j^* = b + c - l_i. \tag{4.62}$$

Here, we set the new phase for cell i to φ_i ($0 \leq \varphi_i < L_i$). Hence, the peak of U_i is present at $l_i = \varphi_i$.

If we define the phase sensitivity function as $Z_0^{(U)}(l_i; \varphi_i)$, then the phase model is formulated as follows.

$$\dot{\varphi}_i = \varepsilon \int_0^{L_i} Z_0^{(U)}(l_i - \varphi_i) \sum_{j \in A(i)} S\left(l_i - \frac{a+b}{2}\right) \left(U_j^{\mathrm{S}}(l_j - \varphi_j) - U_i^{\mathrm{S}}(l_i - \varphi_i)\right) dl_i. \tag{4.63}$$

For simplicity, we normalize these cells so that perimeter length is 2π.

$$\theta_i = 2\pi \frac{l_i}{L_i}, \quad \theta_j = 2\pi \frac{l_j}{L_j} \tag{4.64}$$

$$\phi_i = 2\pi \frac{\varphi_i}{L_i}, \quad \phi_j = 2\pi \frac{\varphi_j}{L_j}. \tag{4.65}$$

The normalized position corresponding to positions $a,\ b,\ c,\ d$ are given by

$$\theta_a = \frac{2\pi}{L_i} a, \quad \theta_b = \frac{2\pi}{L_i} b, \quad \theta_c = \frac{2\pi}{L_j} c, \quad \theta_d = \frac{2\pi}{L_j} d. \tag{4.66}$$

From these equations, Eq. (4.62) follows

$$\theta_j^* = 2\pi \frac{l_j^*}{L_j} = \frac{2\pi}{L_j}(b + c - l_i) = g - \frac{L_i}{L_j}\theta_i, \tag{4.67}$$

where

$$g = \frac{2\pi}{L_j}(b + c). \tag{4.68}$$

If the equations with a Fourier series is expanded as follows,

$$Z_0^{(U)}(\theta_i) = \sum_{n=1} -z_n \sin n\theta_i, \tag{4.69}$$

$$U_i^S(\theta_i) = \sum_{n=0} u_n \cos n\theta_i, \tag{4.70}$$

then the previous phase model becomes

$$\dot{\varphi}_i = \varepsilon \int_a^b Z_0^{(U)}(l_i - \varphi_i) \left(U_j^S(l_j^* - \varphi_j) - U_i^S(l_i - \varphi_i) \right) dl_i \tag{4.71}$$

$$= \frac{L_i}{2\pi} \varepsilon \int_{\theta_a}^{\theta_b} Z_0^{(U)}(\theta_i - \phi_i) \left(U_j^S(\theta_j^* - \phi_j) - U_i^S(\theta_i - \phi_i) \right) d\theta_i, \tag{4.72}$$

thus

$$\dot{\phi}_i = \varepsilon \int_{\theta_a}^{\theta_b} Z_0^{(U)}(\theta_i - \phi_i) \left(U_j^S(\theta_j^* - \phi_j) - U_i^S(\theta_i - \phi_i) \right) d\theta_i \tag{4.73}$$

$$= \varepsilon \int_{\theta_a}^{\theta_b} Z_0^{(U)}(\theta_i - \phi_i) \left(U_j^S \left(g - \frac{L_i}{L_j}\theta_i - \phi_j \right) - U_i^S(\theta_i - \phi_i) \right) d\theta_i \tag{4.74}$$

$$\begin{aligned} &= -\frac{\varepsilon}{2} \sum_{n,k} z_n u_k \left[\frac{\cos((n - k\frac{L_i}{L_j})\theta_i - n\phi_i + kg - k\phi_j)}{(n - k\frac{L_i}{L_j})} \right]_{\theta_a}^{\theta_b} \\ &- \frac{\varepsilon}{2} \sum_{n,k} z_n u_k \left[\frac{\cos((n + k\frac{L_i}{L_j})\theta_i - n\phi_i - kg + k\phi_j)}{(n + k\frac{L_i}{L_j})} \right]_{\theta_a}^{\theta_b} \\ &+ \frac{\varepsilon}{2} \sum_{n,m_{n\neq m}} z_n u_m \left[\frac{\cos(n+m)\theta_i}{n+m} \right]_{\theta_a}^{\theta_b} + \left[\frac{\cos(n-m)\theta_i}{n-m} \right]_{\theta_a}^{\theta_b}. \end{aligned} \tag{4.75}$$

Provided that we should calculate $n = k$ exceptionally in the case of $L_i = L_j$. Here, if we use only first Fourier mode of the function of U and Z, the case analysis is needed only when $n = k = 1$. The new phase model is similar to the dynamics of cell polarity when cell shape is regular hexagonal.

For a simple example, we derive the phase model with the GLE (Eq. (3.3)) for arbitrary polygonal cells.

The normalized functions U_i^S and $Z_0^{(U)}$ are given as

$$U_i^S(\theta_i) = \sqrt{1 - D} \cos\theta_i, \tag{4.76}$$

$$Z_0^{(U)}(\theta_i) = \frac{1}{2\pi\sqrt{1 - D}} \sin\theta_i, \tag{4.77}$$

when $L_i \neq L_j$.

$$\dot{\phi}_i = \varepsilon \sum_{j \in A(i)} \int_{\theta_a}^{\theta_b} \frac{1}{2\pi\sqrt{1-D}} \sin(\theta_i - \phi_i) \left(\sqrt{1-D}\cos(\theta_i - \phi_i) - \sqrt{1-D}\cos(\theta_j^* - \phi_j) \right) d\theta_i \tag{4.78}$$

$$\begin{aligned} &= \sum_{j \in A(i)} \Bigg[\frac{\varepsilon}{4\pi} \sin(\theta_b - \theta_a) \sin(\theta_a + \theta_b - 2\phi_i) \\ &- \frac{\varepsilon}{2\pi\left(1 - \frac{L_i}{L_j}\right)} \sin\left\{ \frac{1}{2}\left(1 - \frac{L_i}{L_j}\right)(\theta_b - \theta_a) \right\} \sin\left\{ \frac{1}{2}\left(1 - \frac{L_i}{L_j}\right)(\theta_a + \theta_b) + \frac{2\pi}{L_j}(b+c) - \phi_i - \phi_j \right\} \\ &- \frac{\varepsilon}{2\pi\left(1 + \frac{L_i}{L_j}\right)} \sin\left\{ \frac{1}{2}\left(1 + \frac{L_i}{L_j}\right)(\theta_b - \theta_a) \right\} \sin\left\{ \frac{1}{2}\left(1 + \frac{L_i}{L_j}\right)(\theta_a + \theta_b) - \frac{2\pi}{L_j}(b+c) - \phi_i + \phi_j \right\} \Bigg] \end{aligned} \tag{4.79}$$

where $\theta_b - \theta_a$ describes cell adhesion length corresponding to d_{ij} in the case the cell shape is regular hexagonal. Consequently, cell polarity is susceptible to a cell–cell interaction in a wide area of adhesion. Rewriting the parameters of the equation to those before normalization, the equation becomes

$$\begin{aligned} \dot{\phi}_i = \sum_{j \in A(i)} \Bigg[&\frac{\varepsilon}{4\pi} \sin\frac{2\pi}{L_i} d_{ij} \cdot \sin\left\{ \frac{2\pi}{L_i}(a+b) - 2\phi_i \right\} \\ &- \frac{\varepsilon}{2\pi\left(1 - \frac{L_i}{L_j}\right)} \sin\left(\frac{2\pi}{L_i} - \frac{2\pi}{L_j} \right) \frac{d_{ij}}{2} \cdot \sin\left\{ \frac{2\pi}{L_i}\left(a + \frac{d_{ij}}{2}\right) - \phi_i + \frac{2\pi}{L_j}\left(c + \frac{d_{ij}}{2}\right) - \phi_j \right\} \\ &- \frac{\varepsilon}{2\pi\left(1 + \frac{L_i}{L_j}\right)} \sin\left(\frac{2\pi}{L_i} + \frac{2\pi}{L_j} \right) \frac{d_{ij}}{2} \cdot \sin\left\{ \frac{2\pi}{L_i}\left(a + \frac{d_{ij}}{2}\right) - \phi_i - \frac{2\pi}{L_j}\left(c + \frac{d_{ij}}{2}\right) + \phi_j \right\} \Bigg]. \end{aligned} \tag{4.80}$$

Therefore, it is expected that cell polarity tends to be oriented toward the direction of the midpoint of the adhesion surface of the cell similarly to the previous phase model. Using this phase model derived from the GLE for any cell shape, various dynamics of cell polarity are investigated in the following sections.

4.9 Dependence on the shape of the system

In Section 4.2, the direction of the cell polarity varies depending on the boundary shape of the system in the case where cell shape is regular hexagonal. This is because the direction of polarity is aligned in any direction when a cell interacts isotropically, and when the cell–cell interaction is biased, the direction is aligned toward the wide cell adhesion area or the interface of a large cell–cell interaction.

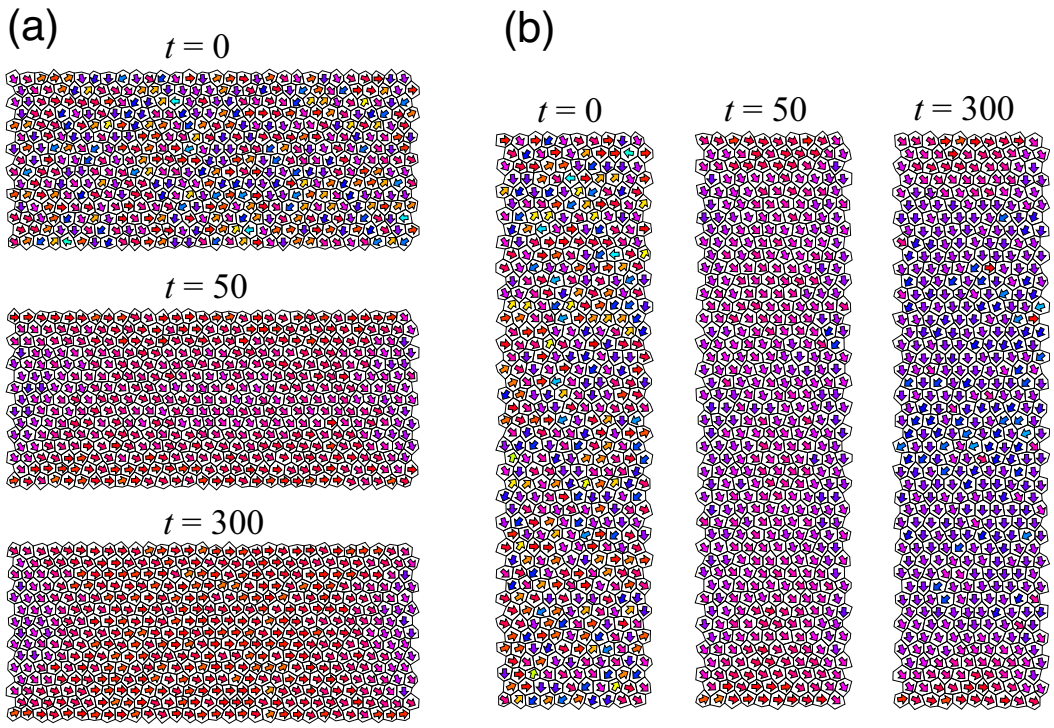

Figure 4.9: Numerical calculation with the system of (a) 10×45 and (b) 30×15 cells. The radius $r = 0.2$. The boundary condition is an open boundary. The direction of cell polarity is aligned along the boundary of the system.

In order to investigate the behaviour of cell polar dynamics for polygonal cells, we analyze numerically by using new phase model, which is similar to that in Section 4.2. In the numerical calculation, we first set six vertices of a regular hexagonal cell as

$$\left(C_x + \cos\frac{(2n+1)\pi}{6},\ C_y + \sin\frac{(2n+1)\pi}{6} \right) \quad (n = 0, 1, \cdots, 5) \tag{4.81}$$

where $(C_x,\ C_y)$ is a center point of a cell. Then we move each vertex within a radius r randomly. When $r = 0$, the cell shape is regular hexagonal, and the larger the radius r, the higher the degree of deformation of the cell. The shapes of cells are varied every 10 simulations. The simulation results are as follows.

As shown in the Fig. 4.9, it is confirmed that the phase polarity direction is aligned along the direction of the longest side of the system boundary. Therefore, we found that the same results are obtained with regular hexagonal cells.

4.10 The relation between nematic order and elongation direction

In the previous section, we found that the direction of cell polarity is aligned along the boundary of the system as in the results for cells that are hexagonal or axially symmetric. As another result, we also found that the cell polarity points to the direction of a contact surface with greater width, in other words, vertical direction corresponding to the cell elongation direction. To investigate whether the behaviour of the polar dynamics is the same as in the situation with any hexagonal cells, we studied the relation between the degree of cell shape change and the direction of cells.

In the numerical simulation, each vertex of regular hexagonal cells is set as

$$\left(C_x + \cos\frac{(2n+1)\pi}{6}\cdot e_x,\ C_y + \sin\frac{(2n+1)\pi}{6}\cdot e_y\right) \quad (n = 0, 1, \cdots, 5) \quad (4.82)$$

where e_x and e_y are elongation rates in the direction of the x- and y-axis, respectively. Other parameters are treated in the same way as in Eq. (4.81). The elongation rates e_x and e_y take values from 1 to 2 at $r < 0.2$. In order to lessen the effect of the boundary shape of the system, the boundary condition for the cell arrangement is set to a periodic boundary as depicted in Fig. 4.12. We adopted the method from Ref. [6] and the Kuramoto order parameter to quantify nematic and polar order.

Components $Q_i^{(x)}$ and $Q_i^{(y)}$ which denote the degree of elongation along the x-axis and y-axis of cell i are determined as integrals of a cell boundary. They are given by

$$Q_i^{(x)} = \int_0^{L_i} w(l_i)\cos(2\chi(l_i))dl_i, \quad (4.83)$$

$$Q_i^{(y)} = \int_0^{L_i} w(l_i)\sin(2\chi(l_i))dl_i \quad (4.84)$$

where L_i is the perimeter of cell i. $\chi(l_i)$ is the angle from the horizontal axis to l_i, and $w(l_i)$ is the distance from the geometric center of cell i to l_i on the cell boundary. These variables are explained in Fig. 4.10.

Q_i, the magnitude of nematic order for each cell i is given as

$$Q_i = \sqrt{\left\{Q_i^{(x)}\right\}^2 + \left\{Q_i^{(y)}\right\}^2}. \quad (4.85)$$

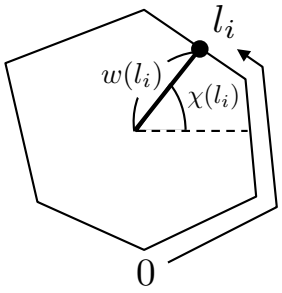

Figure 4.10: Illustration of the calculation of nematic order. $0 \leq l_i \leq L_i$.

The direction of nematic Φ_i is thus

$$\Phi_i = \frac{1}{2} \arctan \frac{Q_i^{(y)}}{Q_i^{(x)}} \tag{4.86}$$

if the following equations are derived

$$\cos 2\Phi_i = \frac{Q_i^{(x)}}{Q_i}, \tag{4.87}$$

$$\sin 2\Phi_i = \frac{Q_i^{(y)}}{Q_i}. \tag{4.88}$$

Here, the average nematic order for all N cells in system Q and the magnitude of deformation of the system are measured with the above-mentioned nematic orders. The average nematic order on each axis is

$$\langle Q_x \rangle = \frac{1}{N} \sum_{i=0}^{N} Q_i^{(x)}, \tag{4.89}$$

$$\langle Q_y \rangle = \frac{1}{N} \sum_{i=0}^{N} Q_i^{(y)}, \tag{4.90}$$

hence the magnitude of nematic Q is determined as

$$Q = \sqrt{\langle Q_x \rangle^2 + \langle Q_y \rangle^2} \tag{4.91}$$

and the direction of average nematic order Ψ is given by

$$\cos 2\Psi = \frac{\langle Q_x \rangle}{Q}, \tag{4.92}$$

$$\sin 2\Psi = \frac{\langle Q_y \rangle}{Q}. \tag{4.93}$$

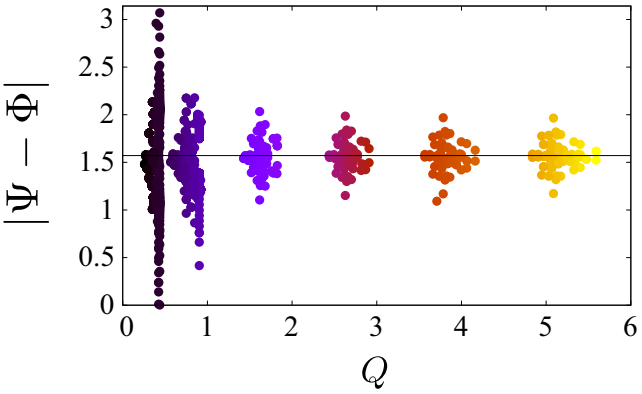

Figure 4.11: The relation between a change in cell shape and the direction of cell polar alignment. The larger the value of Q, the more drastic the deformation becomes. In the vicinity of $Q = 0$, the nematic direction is distributed randomly and aligns vertically, in the cell elongation direction, as the value of Q becomes large.

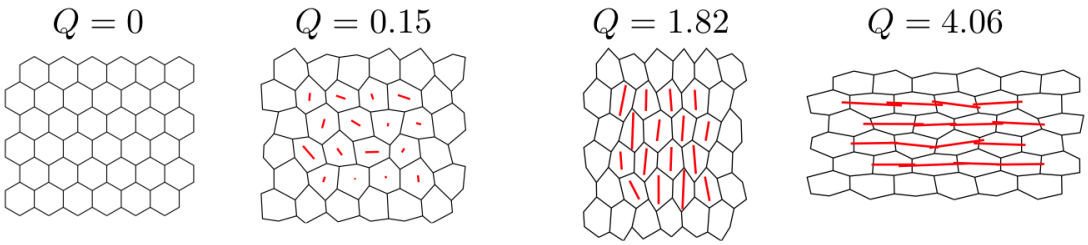

Figure 4.12: Cell shape examples for different degrees of Q. The red line represents the nematic direction, and the length of the line represents nematic order.

When $Q = 0$, the cell shape is regular hexagonal, and the degree of deformation is higher as the value of Q becomes large.

Now we show the results of the numerical simulation. We changed the cell shape from regular hexagonal to a deformed asymmetrical hexagon and analyzed the relation between cell deformation and the direction of the nematic (Fig. 4.11). In the following figure, the horizontal axis represents the degree of deformation of cells Q, whereas the vertical axis represents the difference in angle between the average elongation direction of all cells in the system and the nematic direction. The system is composed of 6×6 cells. In Fig. 4.12, we provide some examples of cell shape corresponding to each Q.

When cell shape is isotropic, in other words, the value of Q is nearly zero, the nematic direction tends to align the direction vertically, in the cell extension direction, because the deformation of the cell is drastic.

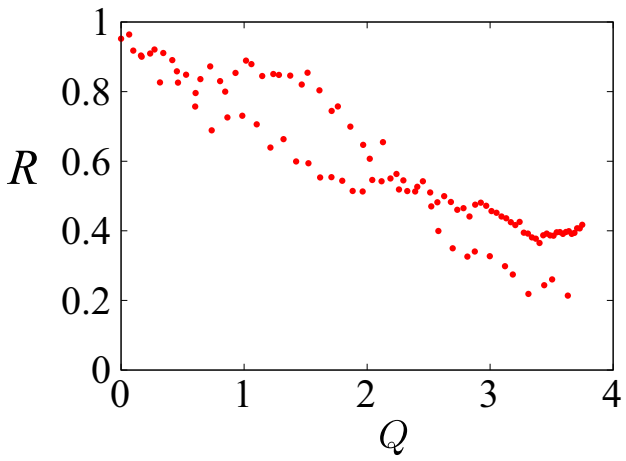

Figure 4.13: The relation between Kuramoto order parameter R and strength of deformation Q. Cell polarity shows good alignment when cell shape is regular hexagonal. As Q increases, R decreases monotonically.

4.11 The relation between cell shape and cell alignment

In the analysis of the dynamics of cell polarity, it is obvious that changes in the shape of the system boundary or individual cells affect cell polarity determination. In this section, we examine the relation between cell shape and the ease of aligning cell polarity.

To check this relation, we fixed cell perimeter at 2π and set the shape to axially symmetric. For quantification of the ease of cell alignment, the Kuramoto order parameter was chosen. We consider the system with 30×30 cells, and we set the boundary condition for the cell arrangement to a periodic boundary to lessen the effect of the boundary shape of the system. The phases are distributed randomly $\phi_i \in [0, 2\pi)$ under initial conditions. Fig. 4.13 is the result of this numerical analysis. The Kuramoto order parameter was obtained from the system at time $t = 10000$ when the system falls into the steady state. 100 sample data points were calculated at each value of Q.

As a result, it was found that polarity of the cell is most likely to be aligned when cell shape is regular hexagonal and the variance of the Kuramoto order parameter gradually increases as the shape is elongated, thereby making it difficult to align. These dynamics of polarity are also reported in Ref. [40] in experiments; the actual epithelial cell sheet prefers regular hexagonal cells for aligning the cell polarity.

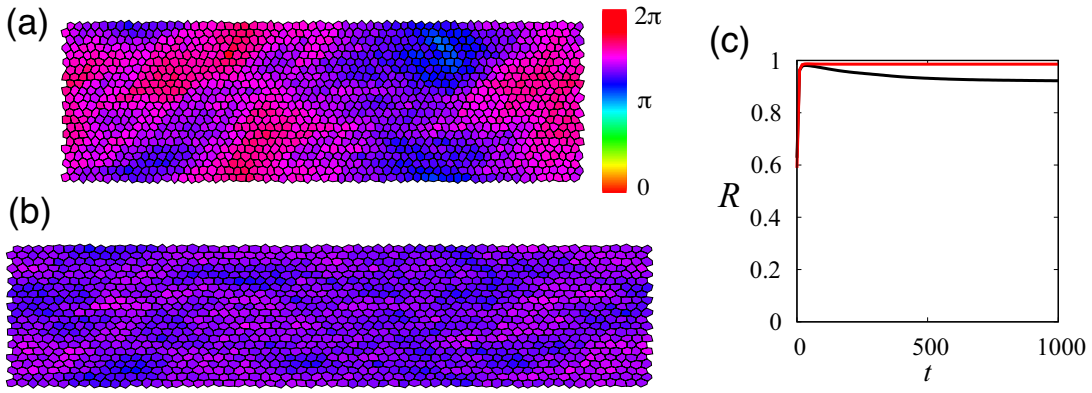

Figure 4.14: (a,b) Numerical simulation with the system of 20×60 cells. The polarity of each cell is represented by color. (a) An isotropic system. Parameters are $e_x = e_y = 1,\ r = 0.22$ in Eq. (4.81). (b) An anisotropic system. Parameters are $e_x = 2,\ e_y = 1,\ r = 0.22$. (c) Time series of the Kuramoto order parameter from panels (a) and (b). It is easier to orient the polarity more globally in the anisotropic system than in an isotropic system.

4.12 Orientation of polarity when the cell system is anisotropic

In the case where the shape of the cell is axially symmetric, the polarity is oriented in the direction in which the adhesive surface became longer during cell elongation. We analyze numerically whether similar results can be obtained when the cell shapes are extended to arbitrarily polygonal cells. The boundary condition of the system is the periodic boundary condition. That is, as shown in Figs. 4.14(a,b), the shapes of cells are set to be the same in two rows at both ends; please note that the actual system is inside the boundary.

The text below shows results of numerical calculation when arbitrary hexagonal cells are elongated in the x-axis direction.
Fig. 4.14 (a) is a system packed with isotropically deformed cells and Fig. 4.14 (b) represents a system containing cells strongly elongated in the direction along the x-axis. In other words, in the model shown in Fig. 4.14 (a), the system is isotropic even though the shape of the cells is not an regular hexagonal, and in the system presented in Fig. 4.14 (b), the system is anisotropic. In such a system, apparently, it is easier to orient the polarity more globally in the anisotropic system than in the isotropic system. As in the case of a regular hexagon, it is assumed that the cell strengthens a cell–cell interaction at a long attachment surface so that the polarity is oriented in that direction. Moreover, when the above numerical analysis was carried out in the XY model, the cell polarity is

oriented in the same direction under the same initial conditions regardless of the system anisotropy.

Then, if we set the shape of the cell to arbitrary hexagonal and set the distortion of the system to isotropic, how will the polarity change when we change the bond strength at the cell adhesion surface? We changed the bond strength in Eq. (4.80) from ε to $\varepsilon(1 + \alpha_{ij})$ as in Eq. (4.18) and calculated the change numerically. In Fig. 4.15, the coupling strength of the adhesive surface is stronger along AP and PD axes in panels (a,b) and (c,d), respectively. We can see that the polarity of cells is oriented globally in a direction in which the coupling strength is strong. According to these findings, when the cell shape is arbitrary, the anisotropy of the system makes it easy to align the polarity globally and tends to orient the polarity in the direction where the strong adhesion surfaces are present. During actual polarity formation in live organisms, anisotropy in a tissue occurs at the beginning of development, and polarity for the most part is aligned during this period. Therefore, it is likely that anisotropy of the tissue is deeply involved in global ordering.

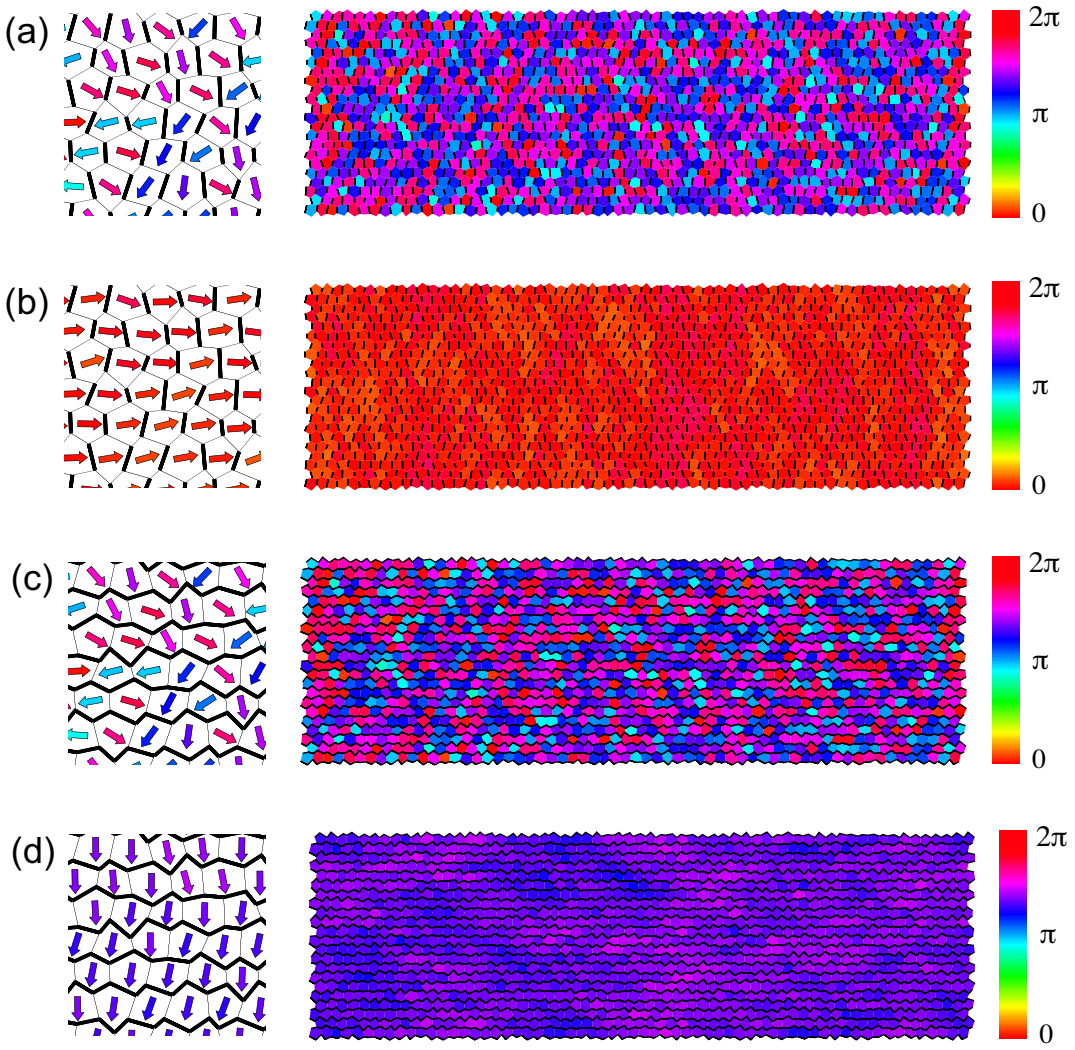

Figure 4.15: Numerical simulation with a system of 20×60 cells. The polarity of each cell is represented by color. The system shape is deformed isotropically. Coupling strength is $\alpha_{ij} = 0.1$ and -0.1 for the surfaces along the direction perpendicular to the PD axis in panels (a,b) and (c,d), respectively; and $\alpha_{ij} = 0$ otherwise. The coupling strength is high along the bold line. (a,c) Initial conditions. (b,d) The cell polarity of the system at time $t = 5000$.

4.13 How to orient cell polarity globally

In Section 4.12, if the cell shapes are arbitrary hexagons, it was confirmed that the cell polarity becomes easier to be oriented globally when the system is anisotropic than isotropic. However, in Section 4.11, we confirmed that when the cell shapes keep symmetry, the cell polarity is most easily oriented if the cell shape is regular hexagonal. Hence, we can assume that the influence of anisotropy of a tissue on

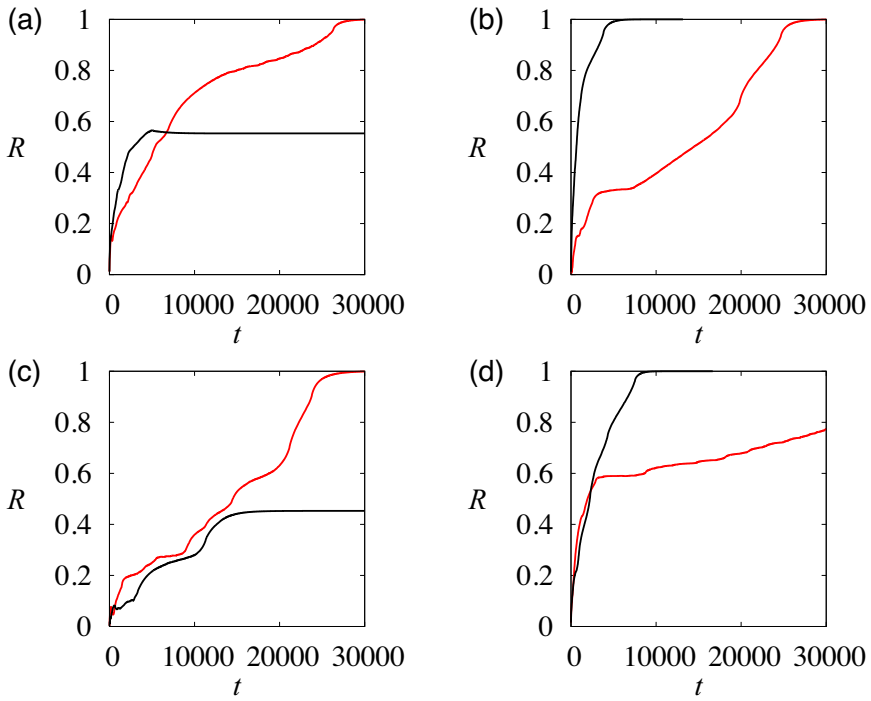

Figure 4.16: The time series of Kuramoto order parameter R under different initial conditions (a–d). The system consists of 80×80 cells. The boundary condition is periodic. The red line represents our phase model, and the black line represents of the XY model.

cell polarity changes depending on whether the cell shape is symmetrical or not. Indeed, in the epithelial tissues of *Drosophila*, it is reported that the tissues filled with regular hexagonal cells are more likely to orient polarity globally. In addition, it is known that polarity is oriented by imparting anisotropy to the isotropic tissues in the process of polarity formation. According to this finding, temporary tissue anisotropy has a positive effect on polarity. At the end of this chapter, we investigated the best timing to impart anisotropy to the system.

It is known that the number of *Drosophila* wing cells is ~ 1 million, and the system was filled with 80×80 cells for numerical calculations. For the initial conditions, the cell phase is randomly assigned to 0–2π, and the case where defects could be made in the system is also considered. The boundary condition is periodic, and cell shape is an arbitrary hexagon. Tissue anisotropy is taken into account by changes in the coupling strength of each cell. For comparison with our phase model, the same numerical calculation was carried out in the XY model. First, we deformed the cell shape isotropically while maintaining isotropic coupling strength, and calculated cell polarity numerically in the phase model and XY model. Although each case is different, we found that the XY

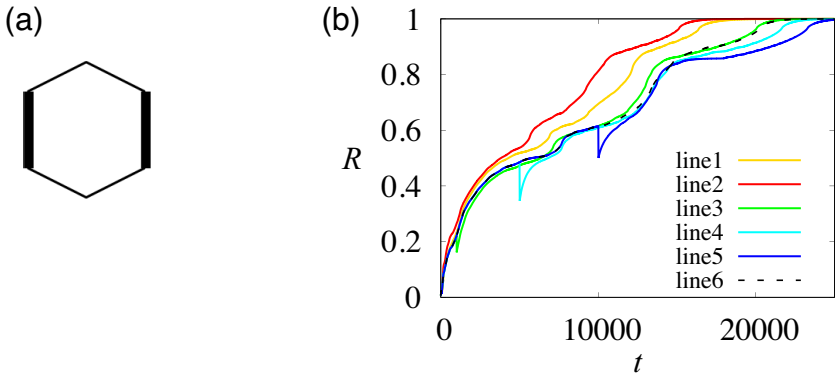

Figure 4.17: (a) Illustration of the adhesion side (bold line) that changes coupling strength. If $\alpha(t) = 0$, coupling strength has the same intensity on all six sides. If $\alpha(t) > 0$, then coupling strength of the black bold line is stronger. (b) Time series of the Kuramoto order parameter. The system consists of 80×80 cells. The boundary condition is periodic. From line 1 to 5 in that order, the results in the case of $t_{\text{start}} = 10,\ 100,\ 1000,\ 5000,\ 10000$. Line 6 shows the case of an isotropic system.

model tends to be more polarized than the phase model (Fig. 4.16). This means that in the XY model, polarity can be oriented isotropically with adjacent cells irrespective of the adhesion surface of the cell, and it is easy to change the cell polarity. Nonetheless, in our phase model, cells interact strongly with adjacent cells whose adhesion surface is wide, and once the polar direction is determined in the direction of that surface, it is difficult to redirect the polarity again in another direction. Next, we changed the coupling strength in the phase model for a short period and investigated the influence on global polarity formation. We defined $\alpha(t)$ as the coupling strength on the cell adhesion side oriented in the direction parallel to the AP axis at time t (Fig. 4.17 (a)). The function of $\alpha(t)$ is given by

$$\alpha(t) = \begin{cases} 0 & (t < t_{\text{start}},\ t_{\text{end}} < t) \\ 0.2 & (t_{\text{start}} \leq t \leq t_{\text{end}}). \end{cases} \tag{4.94}$$

In Fig. 4.17 (b), we compared the case of $t_{\text{start}} = 10,\ 100,\ 1000,\ 5000,\ 10000$, where $t_{\text{end}} = t_{\text{start}} + 10$. It was found that the anisotropy given at the initial stage of the polar formation influences polar orientation and accelerates its formation. By contrast, the anisotropy given later does not significantly affect the formation or even has a negative influence. In addition, because in the case of $t_{\text{start}} = 100$, the time to order polarity globally shortens relative to the case of $t_{\text{start}} = 10$, it is expected that proper timing (at which we operate coupling strength) exists.

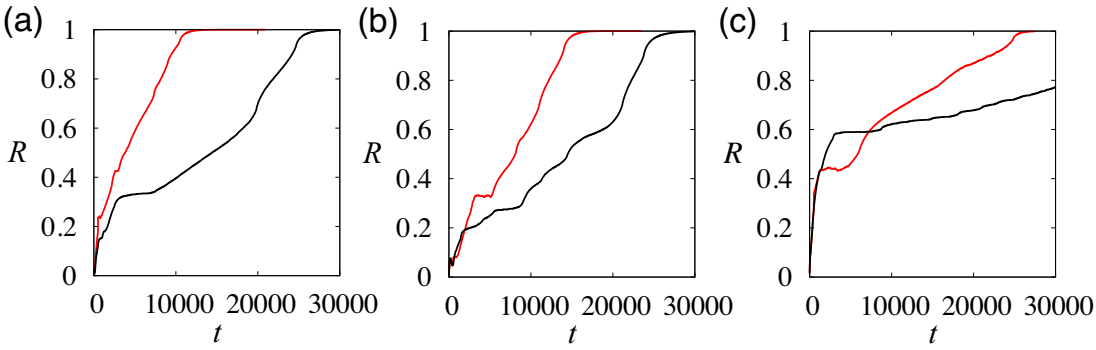

Figure 4.18: A comparison of a phase model whose coupling strength is time-dependent and a general isotropic phase model. The red line represents of the phase model with time-dependent cell coupling. The black line represents the general phase model. The differences among panels (a–c) are initial conditions.

Furthermore, when anisotropy is applied to the system continuously from the beginning ($t = 0$), the polarity is aligned earlier than the polarity formation in the isotropic system, but after a long period, the coupling anisotropy exerts a negative effect on polarity flow (Fig. 4.17).

Therefore, to facilitate realization of global polarity, the coupling anisotropy at the initial stage of polarity formation is given, and then the coupling strength is returned isotropically until a small cell polarity cluster is generated. Actually, by operating the coupling strength and applying the anisotropy to the tissue, we found that the polarity is oriented globally with a higher probability than usual (Fig. 4.18). Here, the time-dependent coupling strength function is given as follows.

$$\alpha(t) = \begin{cases} 0, & (2000 < t) \\ 0.2\left(1 - \frac{1}{1+t-2000}\right), & (2000 \leq t < 3500) \\ \frac{0.2}{1+t-3500}. & (\text{otherwise}) \end{cases} \tag{4.95}$$

Although the relevance of these numerical calculations to experimental results is not clear, it would be an interesting to study the proper timing for getting rid of the defects and aligning cell polarity quickly and globally.

4.14 Conclusions and discussion of polarity ordering

Polarity formation is an important topic in biology, and many mathematical models describing polarity have been considered. For well-known spin models

such as the XY model, a globally ordered state is difficult because many topological defects may appear in a large system, though polarity can be oriented locally. However, defects do not appear in a biological tissue composed of more than $10,000$ cells, and polarity is oriented globally. Although several mechanisms underlying global ordering have been proposed, the factors leading to the global ordering have not been well understood yet. Experiments have shown that such global polarity formation is caused by a global concentration gradient of proteins under the cell sheet and by the mechanical anisotropy of the system owing to cell elongation. Akiyama et al. proposed a model of cell polarity taking into account the global concentration gradient and a cell–cell interaction, but it is reported that cell polarity can be formed without the global concentration gradient in a biological tissue. Aigouy et al. proposed a model in which the polarity is oriented by the anisotropy of a system, but this is an artificial model in a sense that the energy function was set in advance so that the polarity is oriented in the direction of cell elongation. The model proposed by Amonlirdviman et al. is a phenomenological model describing PCP protein distributions in detail; however, it is difficult to obtain a general understanding from this model because of its complexity.

Therefore, using the phase reduction theory for a system with space translational symmetry, we derived a simple phase model from the reaction–diffusion model that phenomenologically describes the dynamics of concentrations of chemical substances. In this phase model, three terms appear when only the lower modes of the Fourier series expansion of $U^S(\theta)$, $Z_0^{(U)}(\theta)$, $S_{ij}(\theta+\eta_{ij})$ in Section 3.3 are considered. The first term describes an effect of phase ordering among the adjacent cells and is similar to the coupling term in the XY model. The second term plays a role in ordering the polarity in the direction of a surface adhered to an adjacent cell. As for the third term, the phase is oriented along the average of own phases of a cell and the phase of a neighboring cell. These latter two terms, which include the geometric information on cells, play a role similar to that of the coupling term describing the response to the global concentration gradient in Akiyama's model. Via these two terms, polarity orientations among adjacent cells are mutually aligned, and moreover, a preferred orientation emerges in response to geometric factors. That is, for the system where cells are aligned in a row and in a longitudinal direction, the polarity is ordered in the lateral and longitudinal direction, respectively. For a system composed of cells spreading on a two-dimensional plane under the open boundary condition, the direction of cell polarity is determined in the cells on the boundary at first, and then the direction of polarity determined by the cells on the boundary is transmitted to inner cells.

The phase model, which became very simple by adopting perturbation method, is easy to analyze, and it is possible to investigate dynamics in the system with many cells. The phase model enabled us to address the following issues: the effect of noise due to cell division and loss of cells, the effect of a global concentration gradient, the change of cell polarity when a hole is made in some part of the system, the role of microtubules, the case of changing cell shape and coupling strength depending on the adhesion surface, and how to set anisotropy in a system for global ordering.

Our phase model is a gradient system, and if we add Gaussian noise to the original reaction–diffusion model, we can obtain the distribution function of polarity by solving the corresponding to Fokker–Planck equation. In numerical calculations for the system with defective cells, even though our phase model is a simple ordinary differential equation, we were able to obtain results similar to those of Amonlirdviman's model, which requires more than 10 partial differential equations for each cell. It is the advantage of our model that it is possible to describe polarity formation without difficulty by means of as many simple ordinary differential equations as there are cells.

What is more, it is understood by experiments that not only the polarity but also the diffusion rate differs depending on the location of the cell adhesion surface owing to cell deformation [41]. As a research topic about a physical model showing polarity, it is interesting to examine the change in polar direction in a model with spatially dependent diffusion coefficients. In our phase model, the findings seem different from the intuitively expected result, i.e., that polarity is easy to align in the direction where PCP proteins diffuse quickly. It would be interesting to investigate whether such a phenomenon can be seen in experiments. Moreover, it was found that the cell polarity is oriented toward the long side of the adhesion surface when cell shapes are deformed. This is because cells interacts wider and stronger where the adhesive surface is relatively longer.

It was also found that even when the strength of the cell–cell interaction changes depending on the direction of the adhesion surface, the polarity is oriented in the direction of the surface where the coupling strength is high. Furthermore, it was clarified that polarity is more easily aligned when the anisotropy of the system is strong in the case where cell shape is arbitrary. This result is consistent with the results of polarity experiments on *Drosophila* wings and on mouse embryos. In actual experiments, a PCP protein tends to accumulate in the direction of the adhesion surface attached to the cell, when this surface is longer than the new adhesion surface generated by cell division. In our model, polarity can be oriented toward a contacting surface with strong coupling naturally. In the study on the implementation of global polarity formation, if the

system is isotropic, polarity can be aligned without generating the most defects when cell shape is regular hexagonal. In contrast, when cell shape is not axially symmetrical, polarity is aligned globally better when the system is more anisotropic.

On the basis of our study on polarity ordering in an anisotropic system so far, in order to orient cell polarity globally, we propose to manipulate the system anisotropy at the initial stage of polarity formation and make the system isotropic after that. In *Drosophila* wing, cells whose shapes are initially regular hexagonal are stretched by a mechanical force, and have anisotropy, but at the latter stage of polarity formation, they become regular hexagonal again and the system becomes isotropic. After that, global polar alignment without defects is realized. For our phase model, it is numerically confirmed that making the system anisotropic in a way similar to experiments also enables global polarity ordering without generating defects. Further studies are needed to investigate these relation between our numerical and experimental results.

In addition, polar alignment can be observed not only in nature but also in an artificial system in which a population of magnetic compasses is placed on a plane [42, 43]. It is only natural that an N-pole of a compass points toward the north, but when the number of compasses is sufficiently large, the direction in which N-poles are oriented depends on the arrangement of compasses. In experiments, it was observed that in the system composed of multiple compasses, N-poles of the compasses at the boundary are aligned along the system boundary, and for compasses inside the system boundary, the polarity of N-poles was ordered continuously. Such experimental results are very similar to those of our phase model when the boundary condition is set as the open boundary. It would be interesting to derive a governing equation of this compass system and compare it with our phase model.

Chapter 5

Phase ordering analysis of spiral chaos

In the previous chapter, we investigated the mechanism of phase ordering. In this chapter, we examine the phase ordering mechanism of focusing of spiral chaos. Such situations can be seen in atrial fibrillation.

5.1 Background and an aim

Excitable media play vital roles in various systems [1, 2, 44]. Excitable media in biological tissues support the propagation of signals, such as concentration waves in the heart and electrical impulses in nerve axons. Such waves are also employed for communication among cells of certain microorganisms (*Dictyostelium discoideum*).

Moreover, excitable media exhibit a particular type of spatiotemporal chaotic dynamics, in which spiral waves are spontaneously generated or annihilated (spiral chaos) [1, 7]. Spiral chaos is commonly observed in surface reaction systems [8, 45]. Similar chaotic dynamics are observed in the heart, causing fibrillation [12]. To date, several mathematical models of excitable media that show spiral chaos have been proposed [12, 45, 46]. Besides, it is known that spiral chaos may develop in oscillatory media, e.g., those obeying the complex Ginzburg–Landau equation (CGLE) [7, 46, 47, 48]. In such mathematical models, depending on the parameter values, spiral chaos persists permanently or terminates spontaneously (Fig. 5.1). In the latter case, the system eventually arrives at a steady state after a transient period, which we refer to as a lifetime. The dependence of the lifetime of spiral chaos on system size has received much attention in the context of treatment of cardiac fibrillation ([12] and the references therein). In Ref. [12], it is numerically demonstrated using both a variant of the FitzHugh–Nagumo

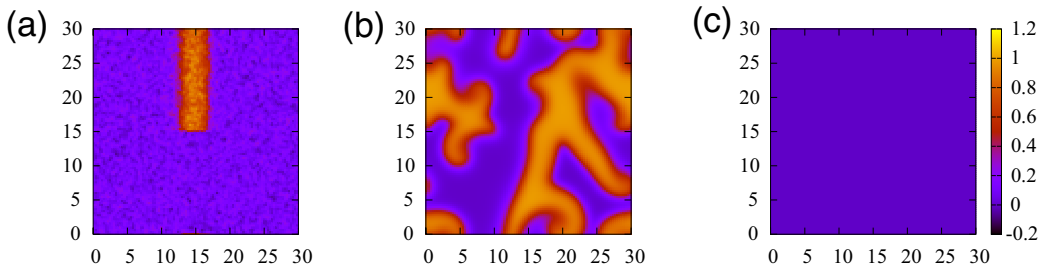

Figure 5.1: Snapshots of $u(x, y, t)$ in the Bär model. (a) The initial condition ($t = 0$) is set up as follows. First, we create a flat excitation wave, run a simulation for a while, and cut the wave in half. We then add random noise with a uniform probability distribution across $[-0.25, 0.25]$. (b) Transient spiral chaos ($t = 1000$). (c) The uniform steady state ($t = 15000$). The parameter values are $a = 0.84,\ b = 0.07,\ \varepsilon = 0.08$, and $N = 30^2$.

model (referred to as the Bär model [45]) and a more realistic model of cardiac electrical dynamics where lifetime increases exponentially with the system size. Such an exponential dependence as well as hyperexponential dependences in other types of transient chaos have already been reported [49, 50, 51, 52].

In the latter half of this thesis, the main focus of our study is to theoretically derive an expression for the dependence of the lifetime of spiral chaos in excitable media on the system size [53]. For this purpose, we first investigate statistical properties regarding the number of spiral cores (namely, defects). There is a large body of studies on such statistical properties [54, 55, 56, 57, 58]. In particular, it is known that as system size increases, the probability distribution of the number of defects during transient spiral chaos approaches a Gaussian distribution [24], as is naturally expected from the central limit theorem. Using this fact, we derive an expression for the system size dependence of lifetime on system size, and this relation is indeed exponential. We extensively investigate the system size dependence of lifetime using two models: the Bär model and the CGLE, with several parameter sets and different boundary conditions. We found that although lifetime increases exponentially with system size in all cases, our expression well fits the parameter sets near the onset of transient chaos, suggesting that some assumptions may be violated depending on parameter values.

5.2 Spatiotemporal chaos

Spatiotemporal chaos is known as mathematical dynamics similar to atrial fibrillation. Spatiotemporal chaos is a state whose behavior is chaotic both spatially and temporally. Because it is sensitive to the initial condition, a slight difference in initial states yields a large difference in the results. Therefore, the state of the

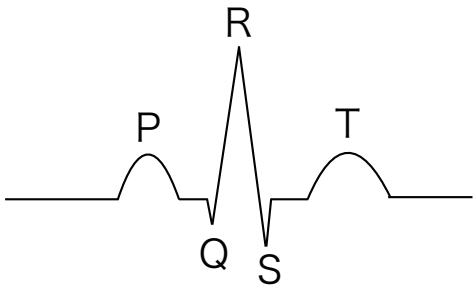

Figure 5.2: An electrocardiogram. The potential rises when the myocardium is excited.

system in the future cannot be predicted and is difficult to handle.

An excitable medium, that is a medium showing excitement when there is an input exceeding a certain threshold value, and an oscillating medium, which periodically shows excitement, are some of the known media that show such spatiotemporal chaos [1, 2, 44]. In this chaos, a pattern of excitable waves emerges by transmitting the excitation of a firing element to the surroundings, and this wave pattern can be seen in the human body, e.g., neuronal firing, the heart, or chemical systems such as the Belousov–Zhabotinsky (BZ) reaction and a starving Dictyostelium discoideum population as explained below.

5.2.1 The pulse of the heart

The electrical signal of the heart is also an exciting wave. The heart is composed of vertically elongated cardiomyocytes which propagate electrical signals transmitted from the sinoatrial node to the surrounding cells. The myocardium is excited when the electric signal is received, and after being excited, it falls into the state where it does not react for some time even if it receives any stimulus; this period is called a refractory period. After the refractory period, the cell is excited again by propagating electrical signals. The excitement of the myocardium is represented by the following electrocardiogram (Fig. 5.2). The place and time of excitation can be read in this cardiogram.

5.2.2 BZ reaction

The BZ reaction is the famous example of Turing instability. The mechanism of this reaction is the oxidation–reduction reaction involving malonic acid and a cerium ion as catalyst. The reaction substrate is oxidized, then spatial variation of ion concentration creates patterns of concentric circular waves and spiral

waves. In the experiments on the BZ reaction, it was found that the spiral wave spreads with time from the site that received the stimulus when the solution in a petri dish is stimulated with the tip of a toothpick.

5.2.3 Dictyostelium

Dictyostelium discoideum usually lives as an ameboid individual. Nevertheless, when the individuals starve, one dictyostelium cell sends a crisis signal to the surroundings, and others assemble forming a multicellular population toward the signal. It is known that the pattern made by dictyostelium in a starving state becomes spiral. It seems that the electric signal wave and chemical reaction wave grow as a spiral. These spatiotemporal spiral patterns created by an excitable and oscillating medium repeat generation and extinction [1, 7, 8, 59]. This pattern is also observed in a numerical simulation of arrhythmia [12]. In the text below, such spatiotemporal chaos is called spiral chaos. Here, we focused on the dynamics of chaos that can be seen during atrial fibrillation.

5.3 Atrial fibrillation

The human heart always contracts autonomously in a regular beat though humans are not aware of this process. This autonomous work is due to the electrical activity of the heart. Usually, the heart regularly delivers blood to parts of the body by receiving electrical signals with constant rhythm that are propagated from the sinoatrial node playing the role of a pacemaker. A schematic diagram of a part of a electrocardiogram is shown in Fig. 5.2. There is a P wave, QRS wave, and T wave [60]. P and QRS waves represent excitation of the myocardium and ventricular muscle, respectively, after receipt of an electrical signal from the sinoatrial node. The position of the P wave varies depending on the timing of the electrical signal from the sinoatrial node, and in abnormal cases, it is absent. The time between a P wave and Q wave corresponds to the period when an electrical signal from the sinoatrial node is transmitted from the atrium to the ventricle. R represents excitation when the heart contracts under the influence of the electrical signal, and at position S, the ventricle stops getting excited. The QRS wave corresponds to the time from the beginning of excitation of the ventricle to the end. If the duration of the QRS wave takes longer, the excitement time becomes longer. Therefore, it is assumed that the flow of the electric signals in the ventricle deteriorated. The T wave represents the period when the ventricular muscle contracted by excitation returns to its original state.

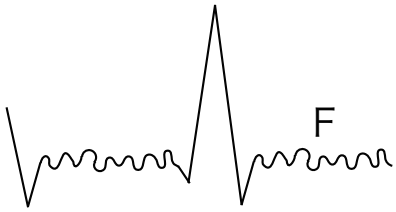

Figure 5.3: An electrocardiogram. The F wave appears instead of the P wave.

Now, the waveform as shown in Fig. 5.3 is rarely seen in electrocardiograms. The new wave, an F-like ripple wave appears instead of the P wave.

In that case, the heart does not show correct movements, and the electric signal from the sinoatrial node is not regularly propagated to the atrium and ventricle. This is a kind of arrhythmia, a symptom of atrial fibrillation frequently encountered clinically [61]. This symptom is not only accompanied by palpitations but also can cause cerebral infarction mediated by thrombosis in the heart (a thrombus peels off). According to the research by the Japanese Circulation Society, the prevalence of atrial fibrillation in Japan is expected to exceed one million in 2030; thus, it is a disorder that happens to almost everyone.

Catheter ablation is known as a typical operation for atrial fibrillation [62, 63]. When atrial fibrillation develops, the electric signals from the sinoatrial node form spirals. These spirals meander and repeat generation and extinction in the atrium [64].

In catheter ablation, a catheter, whose diameter is $1.3 \sim 2.6$mm, is inserted through the vein from the groin to the heart, and the closed region of the heart is cauterized by the electrode attached to the tip of the catheter. This way, tissues of the heart are warmed, and proteins are coagulated, which block the bad propagation of the electronic signal and can stop the fibrillation. In the case of atrial fibrillation, the success rate of surgery is from 60 to 95% and there are cases where more than two operations are needed for a full recovery. The Maze operation is known as another surgical method. In this operation, patients use a mechanical heart while their cardiac function is being repaired. The region where the abnormal signal in the heart occurs is incised and the myocardium is sewn up again, then the fibrillation is stopped. However, it is difficult to capture the electric spirals with these surgical methods. Moreover, it is unclear how large an area should be cauterized or incised [65].

Chapter 6

Analysis of transient spiral chaos

In this chapter, a theoretical formula for predicting the lifetime of spiral chaos in excitable media is derived. The distribution of the number of defects approaches the Gaussian distribution according to central limit theorem. On the basis of this fact, we provide a general expression for the dependence of lifetime on system size; this relation is valid for large system sizes.

6.1 The model and numerical settings

For most of our numerical analyses, we employ the Bär model [45], which is a modified FitzHugh–Nagumo model representing an excitable medium. This model has also been studied in [12]. The model gives

$$\frac{\partial u}{\partial t} = -\frac{1}{\varepsilon}u(u-1)\left(u - \frac{v+b}{a}\right) + D\nabla^2 u, \tag{6.1a}$$

$$\frac{\partial v}{\partial t} = f(u) - v, \tag{6.1b}$$

$$f(u) = \begin{cases} 0 \ , \ u < \frac{1}{3}, \\ 1 - 6.75u(u-1)^2 \ , \ \frac{1}{3} \leq u \leq 1, \\ 1 \ , \ u > 1, \end{cases} \tag{6.1c}$$

where parameters ε, a, b, and the diffusion coefficient D are positive. The system is two-dimensional with an area of $L \times L \equiv N$. Variables $u(x, y, t)$ and $v(x, y, t)$ are interpreted in the context of cell physiology as membrane potential and the recovery variable, respectively [44].

Numerical simulations are performed by the fourth–order Runge–Kutta method with a space step $h = 0.3$ and time step $s = 0.01$.

In Eq. (6.1), uniform steady state $u(x, y) = v(x, y) = 0$ is linearly stable

for any set of parameter values. By inserting the ansatz $u, v \sim e^{\lambda t - \mathrm{i}\boldsymbol{q}\cdot\boldsymbol{r}}$ with $\boldsymbol{r} = (x, y)$ and wave vector $\boldsymbol{q}$ of a perturbation, we obtain

$$\lambda = -1, -\frac{b}{a\varepsilon} - D|\boldsymbol{q}|^2, \tag{6.2}$$

which is always negative. See also the appendix for the linear stability analysis. Hence, the system should smoothly arrive at a uniform steady state if the initial state is close to it.

Nonetheless, at appropriate parameter values and initial conditions, spatiotemporal chaotic dynamics arise (referred to as spiral chaos) (Fig. 5.1). As reported in Ref. [45], for a broad range of b ($b < 0.18, a = 0.84$), the following behavior emerges. For small ε values ($0.01 < \varepsilon < 0.06$), spiral waves rigidly rotate. For $\varepsilon > 0.06$, spiral waves begin to meander. For $\varepsilon > 0.07$, spiral chaos arises. In this region, spirals begin to break up after some transient rotations, resulting in the formation of two free ends of a wave. From these free ends, a new pair of counter-rotating spirals arises. There is also a pair annihilation process, in which the cores of a pair of counter-rotating spirals collide and cancel each other out. Moreover, in the Neumann boundary condition, there is an additional case in which a defect is absorbed by the boundary. These processes are repeated chaotically.

Lifetime can be defined as the time that the system takes to settle down to the steady state after the start of a long excitement state as shown in Fig. 5.1(c). To measure the lifetime of the system, we used the Kuramoto order parameter, which helps to analyze whether each element is synchronous or not, and calculated the number of defects as described in Section. 6.3.1. The Kuramoto order parameter in two-dimensional space $L \times L$ is given by

$$R = \frac{1}{L^2} \int_0^L \int_0^L \mathrm{e}^{\mathrm{i}\phi(x,\ y)} dxdy \tag{6.3}$$

where $\phi(x,\ y)$ is the argument of concentration $u(x,\ y,\ t) - u^*$ and $v(x,\ y,\ t) - v^*$. The image of the Kuramoto order parameter can be explained using a circle with the radius of 1.0. Now we assume that there are N oscillating particles, and these particles are rotating on the circle. When the system is synchronized, particles that were moving apart initially, gather and move as clusters. At this time point, the Kuramoto order parameter R converges to 1.0 because the argument approaches zero. On the contrary, R takes a value close to zero when particles keep moving apart on the circle. For example, we illustrate a time series of the Kuramoto order parameter via a numerical simulation depicted in Fig. 5.1 (Fig. 6.1).

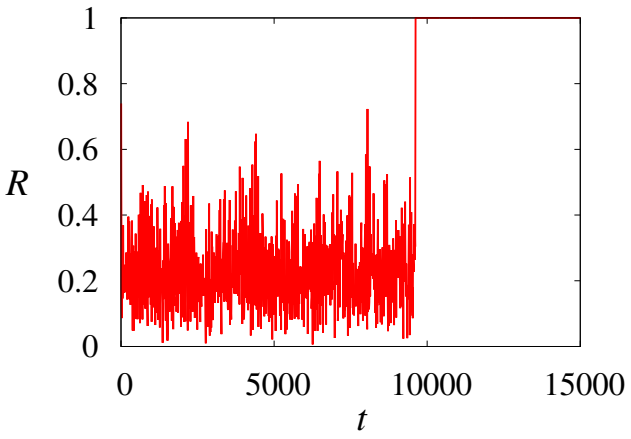

Figure 6.1: A time series of the Kuramoto order parameter. It fluctuates while $R < 1$ which corresponds to the state of Fig. 5.1(b). The system starts to synchronize gradually as shown in Fig. 5.1(c) and finally the value of R takes 1.0. The initial condition is the same as the case in Fig. 5.1.

In our numerical simulation, we determine lifetime as the time taken to reach $R > 0.99$ at first. Another way to measure lifetime is described later in Section 6.3.1.

As a convenient initial condition for implementing this chaotic state, we employ a flat broken wave (Fig. 5.1), in which initially there exists a defect in Neumann boundary conditions or a pair of defects in periodic boundary conditions. To obtain statistically independent results for each run of the simulations, we add independent random noise obeying a uniform probability distribution over $[-\eta, \eta]$ with $\eta = 0.25$ to u and v at all discretized points at $t = 0$. Note that the evolution is noise free for $t > 0$. In the preliminary numerical simulations, we have checked that the statistical results do no change quantitatively for $\eta = 0.1$ (results not shown). The results presented assume a periodic boundary condition and $a = 0.84,\ b = 0.07,\ \varepsilon = 0.08,\ D = 1$ unless otherwise noted. Some results are obtained with the Neumann boundary condition and/or other sets of b and ε values.

To check the generality of our argument, we also numerically studied the oscillatory media described by the CGLE, given by

$$\frac{\partial W}{\partial t} = W + (1 + \mathrm{i}c_1)\nabla^2 W - (1 + \mathrm{i}c_2)|W|^2 W, \tag{6.4}$$

where $W(x, y, t) \in \mathbb{C}$ and $c_1, c_2 \in \mathbb{R}$ are the parameters of this system [7].

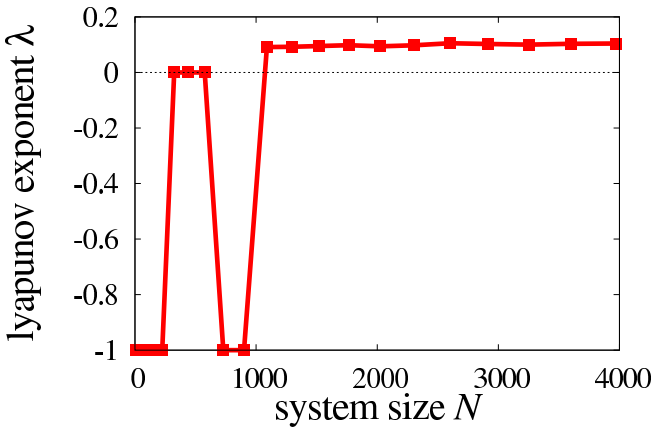

Figure 6.2: The Lyapunov exponent. We set $\boldsymbol{X}_0 = 10^{-5}$, $T = 2 \times 10^6$, $t_0 = 10^6$.

6.2 The Lyapunov exponent

Spatiotemporal chaos has initial-value sensitivity, hence a slight difference in initial conditions yields a large difference in states. To quantify the disturbance of the system's state, we adopted the Lyapunov exponent (Fig. 6.2).

For the Bär model, we defined the concentration that slightly deviated from u and v as u' and v'. Lyapunov exponent λ is given by

$$\lambda = \lim_{t\to\infty} \lim_{|\boldsymbol{X}_0|\to 0} \frac{1}{t} \log \frac{|\boldsymbol{X}(t)|}{|\boldsymbol{X}_0|} \tag{6.5}$$

where $\boldsymbol{X}(t)$ is the difference between two trajectories $(u - u',\ v - v')$, and $|\cdot|$ denotes the magnitude of the vector, and $\boldsymbol{X}(0) = \boldsymbol{X}_0$ corresponds to the difference between two initial trajectories.

Here, we can derive the equation

$$e^{\lambda t} \approx \frac{|\boldsymbol{X}(t)|}{|\boldsymbol{X}_0|}, \tag{6.6}$$

It can be determined that the solution of the system is stable when $\lambda < 0$, chaotic when $\lambda > 0$, and periodic when $\lambda = 0$ because the difference between two trajectories stays constant [19, 66]. Please note that we run calculations for an extended period, T, after initial transition time t_0 to obtain Lyapunov.

The horizontal axis represents system size, and the vertical axis denotes the value of the Lyapunov exponent after $t = 10000$ numerical simulations. The wavelength of this system is ~ 10 which is close to half the length of one side of the square in Fig. 6.3. Hence the changes in the behavior of the system can be seen when the length of one side of the square system is twice the wavelength. The

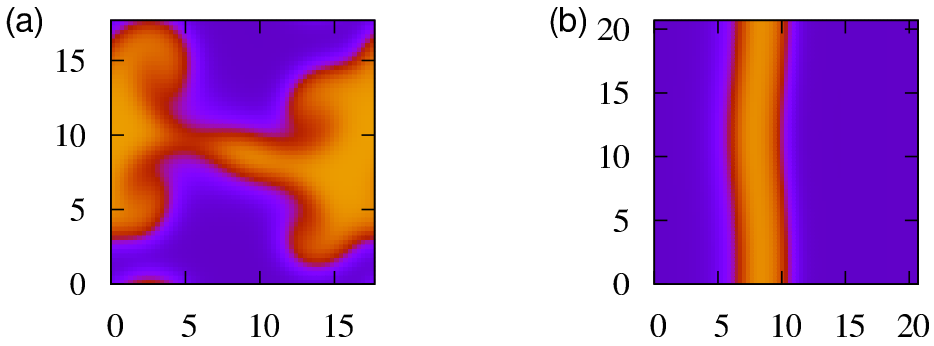

Figure 6.3: The behavior of the system at different system sizes. Each The system size is (a)$N = 18 \times 18$; and (b)$N = 21 \times 21$.

Lyapunov exponent is negative when the system size is smaller than $N = 15 \times 15$ for the periodic boundary condition; thus, the system falls into a steady state after long transition time. In the system with system size from $N = 18 \times 18$ to $N = 24 \times 24$, the Lyapunov exponent vanishes, and the solution of the system is oscillating. The state of oscillating varies depending on the system size. When the system size is $N = 18 \times 18$, there are four stable spirals in the region as shown in Fig. 6.3(a). These four spirals do not meander in the system and are pinned in a four split region. In the case when the system size is $N = 18 \times 18$ or more but less than 24×24, the plane wave whose velocity is $v = 2.1$ continues to flow (Fig. 6.3(b)). The value of the Kuramoto order parameter keeps $R < 1$ after the spiral diminishes.

If the system has size from $N = 27 \times 27$ to $N = 30 \times 30$, the system falls again into the steady state. As the system size increases more than $N = 33 \times 33$, the Lyapunov exponent is still positive, and the chaotic state lasts for a long time.

6.3 Time evolution and probability distribution of the number of defects

6.3.1 Defect counting

We first investigate the time evolution and probability distribution of the number of defects. All the results in this section are for periodic boundary conditions. We confirmed that qualitatively the same results were obtained with Neumann boundary conditions.

The number $m(t)$ of defects at time t in the system was counted as follows.

Phase $\phi(x, y)$ of the state is defined by

$$\phi(x, y) = \arg[(u(x, y) - u_0) + \mathrm{i}(v(x, y) - v_0)] \tag{6.7}$$

with $(u_0, v_0) = (0.5, 0.3)$. The topological charge $C(x, y, t)$ is defined by

$$C(x, y, t) = \frac{1}{2\pi} \oint \nabla\phi(x, y, t) \cdot d\boldsymbol{l}. \tag{6.8}$$

The defects with $C = 1$ and -1 are the core of counterclockwise and clockwise spirals, respectively. The topological charge is obtained numerically by calculating

$$C(x, y) = \frac{1}{2\pi}(\phi_{1,2} + \phi_{2,3} + \phi_{3,4} + \phi_{4,1}), \tag{6.9}$$

where

$$\phi_{i,j} = \phi_i - \phi_j \quad (-\pi \leq \phi_{i,j} < \pi), \tag{6.10}$$

with

$$\phi_1 = \phi(x,\ y), \quad \phi_2 = \phi(x + h,\ y), \quad \phi_3 = \phi(x + h,\ y + h), \quad \phi_4 = \phi(x,\ y + h),$$

and h is the space step employed in our numerical simulations. We then reset $C = \pm 1$ when a numerically obtained C value is in $[(\pm 2\pi - 0.1)/2\pi,\ (\pm 2\pi + 0.1)/2\pi]$ and $C = 0$ otherwise. Number $m(t)$ of defects is the sum of $|C|$ across the entire system. In the periodic boundary condition, defects meander in the system, collide with different rotation defects to annihilate or generate a pair of defects. In addition to these behaviour of defects, the latter are sometimes attracted to the boundary and vanish in the Neumann boundary condition.

6.3.2 A time series of defects

Now we investigate the system size dependence of lifetime by counting defects according to the above definition. As presented in Fig. 6.4, $m(t)$ fluctuates strongly with time, and this chaotic process appears to be stationary.

However, defects completely vanish after some time without any clear presage, and the system falls into a uniform steady state. As is the case in Figs. 6.4 (a) and (b), a larger system typically has a larger number of defects and a longer transient time.

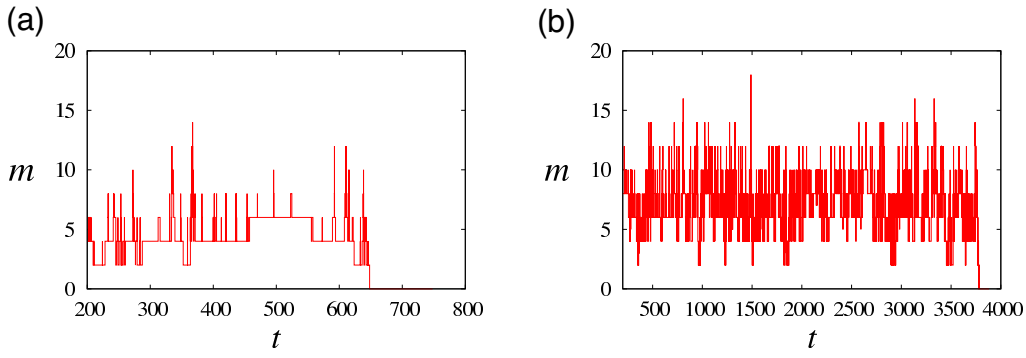

Figure 6.4: A time series of the number $m(t)$ of defects at system size (a) $N = 24^2$ and (b) $N = 30^2$.

6.3.3 A distribution of the number of defects

Here, statistical properties are analyzed in the time series of $m(t)$ during transient chaos after the initial transient process ($t > 100$) (Figs. 6.5 and 6.6). For each system size, we employ many different initial conditions and the number of defects is counted at each time step until the system arrives at the steady state. We find that both the mean μ and variance σ^2 of $m(t)$ are approximately proportional to the system size N (Fig. 6.5):

$$\mu = \alpha N, \tag{6.11}$$

$$\sigma^2 = \beta N. \tag{6.12}$$

The linear growth of μ has also been found in [67]. Next, we measure the probability distribution of the number of defects, which is the probability that there are m defects at each time point in the system during transient chaos.

As reported in Ref. [8], we confirmed that the probability distribution approaches the following Gaussian distribution as the system size increases (Fig. 6.6):

$$p(m) = \frac{\delta}{\sqrt{2\pi\sigma^2}} \exp\left[-\frac{(m-\mu)^2}{2\sigma^2}\right], \tag{6.13}$$

$$= \frac{\delta}{\sqrt{2\pi\beta N}} \exp\left[-\frac{(m-\alpha N)^2}{2\beta N}\right], \tag{6.14}$$

where $\delta = 1$ for the Neumann boundary condition and $\delta = 2$ for the periodic boundary condition because m takes only even numbers in the latter case.

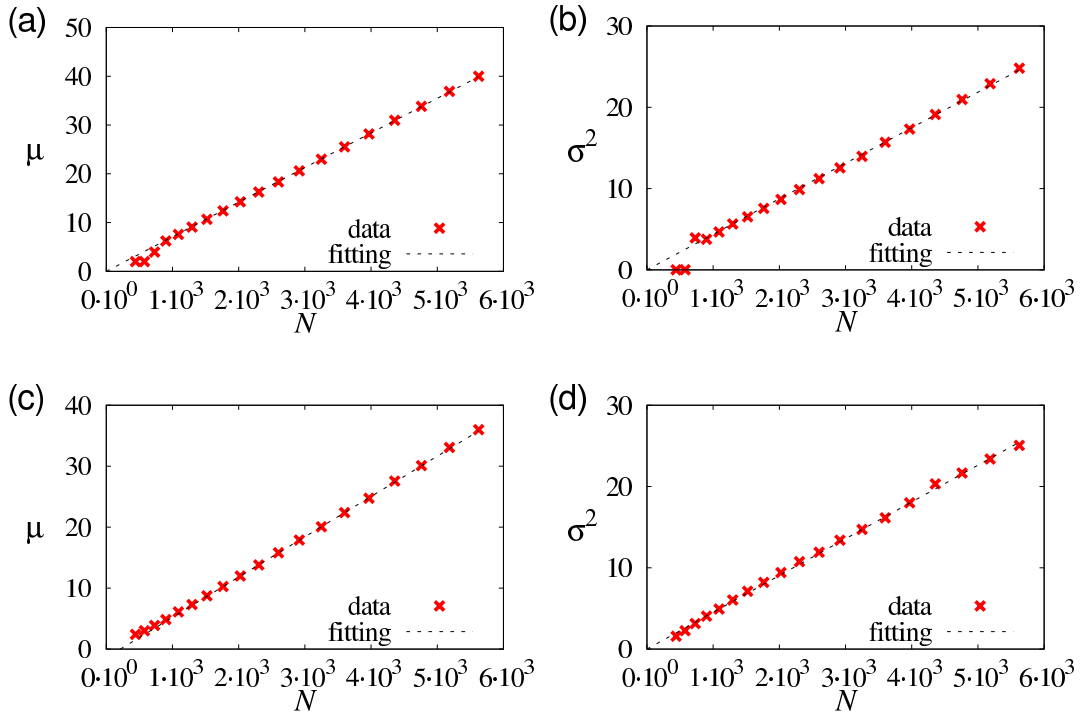

Figure 6.5: Mean μ and variance σ^2 of the number of defects. (a, b) Results for the periodic boundary condition. The fitting lines are $\mu = 0.00709N$ and $\sigma^2 = 0.00437N$. (c, d) Results for the Neumann boundary condition. The fitting lines are $\mu = 0.00660N - 1.3996$ and $\sigma^2 = 0.00452N$. Fitting is performed for data with $N > 2000$.

6.3.4 Correlation length of defects

These results can be rationalized by the following argument. Suppose that the system is virtually divided into n subsystems of size $\tilde{L} \times \tilde{L} = \tilde{N}$. For a periodic boundary condition, all the subsystems should share a certain probability distribution of the number of defects with mean $\tilde{\mu}$ and variance $\tilde{\sigma}^2$. If the linear length $\tilde{L}$ of each subsystem is sufficiently greater than the correlation length of the system, these subsystems are approximately independent.

To estimate the correlation length, we used two methods. First, the density of defects with $C = -1$ and $C = 1$ at (x, y) as a function of the distance

$$\xi = \sqrt{(x - x_0)^2 + (y - y_0)^2}$$

from a certain defect with $C = 1$ at (x_0, y_0) was calculated. As illustrated in Fig. 6.7(a,b), the correlation length is nearly 10. Second, as a calculation of coefficient $r(\xi)$ of the concentration $u(x, y, t)$, Pearson's moment-generating

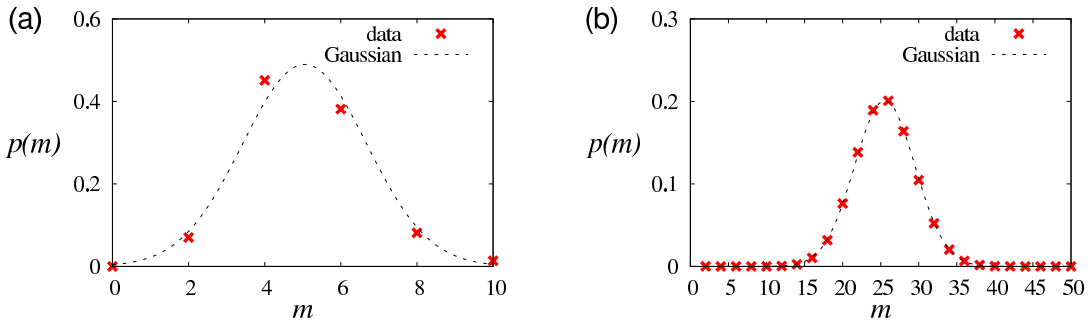

Figure 6.6: Distributions of the number of defects. (a) System size $N = 27^2$, (b) $N = 60^2$. The dashed lines are the Gaussian distributions with average $\mu = \alpha N$ and variance $\sigma^2 = \beta N$ with $\alpha = 0.00709$ and $\beta = 0.00437$.

function was utilized in two-dimensional system $L \times L$ as follows.

$$r(\xi) = \frac{\displaystyle\int_0^T (u^* - \overline{u})(u - \overline{u})dt}{\displaystyle\sqrt{\int_0^T (u^* - \overline{u})^2 dt}\sqrt{\int_0^T (u - \overline{u})^2 dt}} \tag{6.15}$$

where

$$u^* = u\left(\frac{L}{2},\ \frac{L}{2},\ t\right), \quad u = u\left(\frac{L}{2} - \xi,\ \frac{L}{2},\ t\right), \quad \overline{u} = \frac{1}{T}\int_0^T u\left(\frac{L}{2},\ \frac{L}{2},\ t\right) dt. \tag{6.16}$$

When r takes the value ~ 1.0, it implies that the relation between them is a strong correlation; therefore, it can be stated that this is a positive linear correlation. On the other hand, when r takes the value near -1, it can be stated that this is a negative linear correlation. When $r = 0$, there is no correlation, hence we can say that there is no linear correlation.

Similarly to the correlation length of defects, it was found that there is a strong positive correlation in the system up to the distance 3.0. Furthermore, there is almost no correlation for the distance greater than 10. Judging by these results, the correlation length is roughly 10 or smaller (Fig. 6.7).

The number of defects m in the entire system is the sum of defects of independent subsystems. The mean and variance of m are then proportional to the system size. Moreover, as stated by the central limit theorem, m will obey the Gaussian distribution with mean $\mu = n\tilde{\mu}$ and variance $\sigma^2 = n\tilde{\sigma}^2$ where $n \equiv \frac{N}{\tilde{N}}$ when n is sufficiently large. This is also approximately the case for the Neumann boundary condition when L is sufficiently larger than the correlation length.

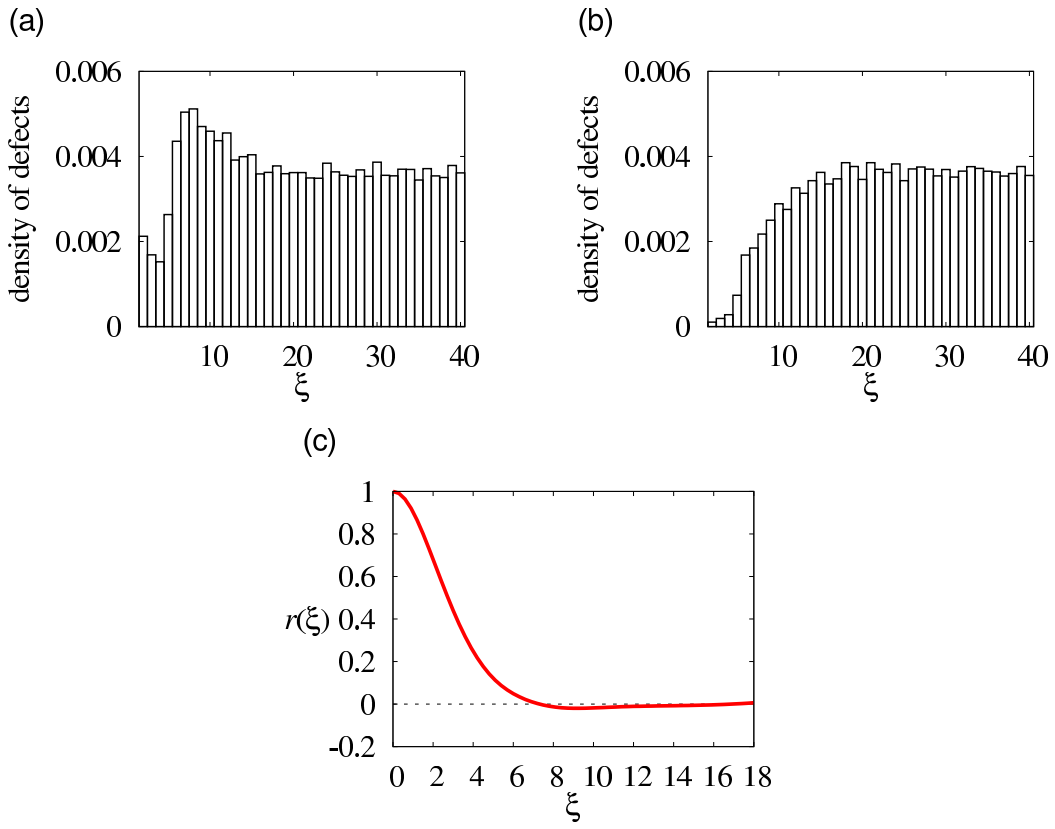

Figure 6.7: Numerical measurement of correlation length. We estimate the correlation length by two methods. (a, b) The density of defects with (a) $C = -1$ and (b) $C = 1$ at (x, y) as a function of distance ξ from a certain defect with $C = 1$ at (x_0, y_0). (c) Pearson product–moment correlation coefficient $r(\xi)$ for variable u. These results indicate that the correlation length is roughly 10 or less.

Because this argument is very general, the Gaussian distribution should be obtained for both the periodic and Neumann boundary conditions and other models showing spiral chaos when N is sufficiently large. In fact, we confirmed this notion for the Bär model and the CGLE with all the parameter sets we chose and both boundary conditions.

6.4 System size dependence of lifetime

As already mentioned, a previous numerical study reported that the lifetime of transient spiral chaos increases exponentially with the system size. We also numerically confirm it in the following manner.

Under any boundary conditions, all the defects must completely vanish before the system settles down into the steady state. Here, it should be noted that there

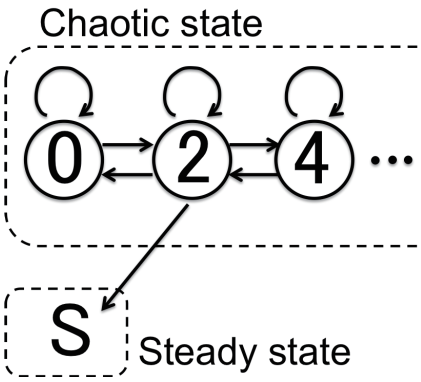

Figure 6.8: The defect generation–annihilation process for periodic boundary condition. The circle with number m denotes the state with m defects. Symbol S denotes the uniform steady state.

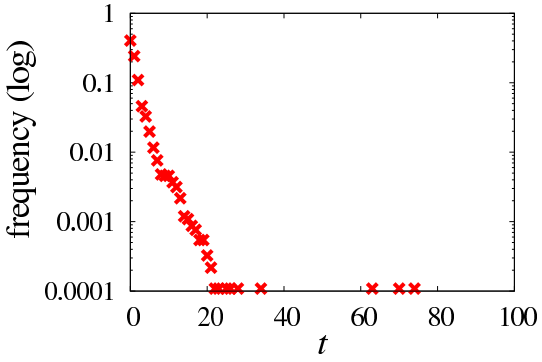

Figure 6.9: A normalized histogram of the duration in which number m of defects continues to be zero until m becomes 2. Here, the value at $t = k \in \mathbb{N}$ denotes the frequency of the duration $k - 1 < t \leq k$. The Bär model with $b = 0.07, \varepsilon = 0.09$. Defects seldom re-emerge for $t > 20$.

is still a chance that a pair of defects is generated even from the state with $m = 0$ because of some remaining complex pattern. Therefore, the transition between the states with different numbers of defects m can be illustrated as in Fig. 6.8, where the periodic boundary condition is assumed for simplicity so that m takes only even numbers, and symbol S denotes the uniform steady state.

To define lifetime, we regard the system state as the steady state when the duration of the state with $m = 0$ continues for 100 simulations, because defects hardly re-emerge if the state with $m = 0$ continues for 20 simulations (Fig. 6.9).

Under such a numerical setup, we analyze the dependence of lifetime on system size N (Fig. 6.10), which is indeed exponential.

The expression for the system size dependence of lifetime $T(N)$ can be obtained as follows. We assume that the process illustrated in Fig. 6.8 is Markovian.

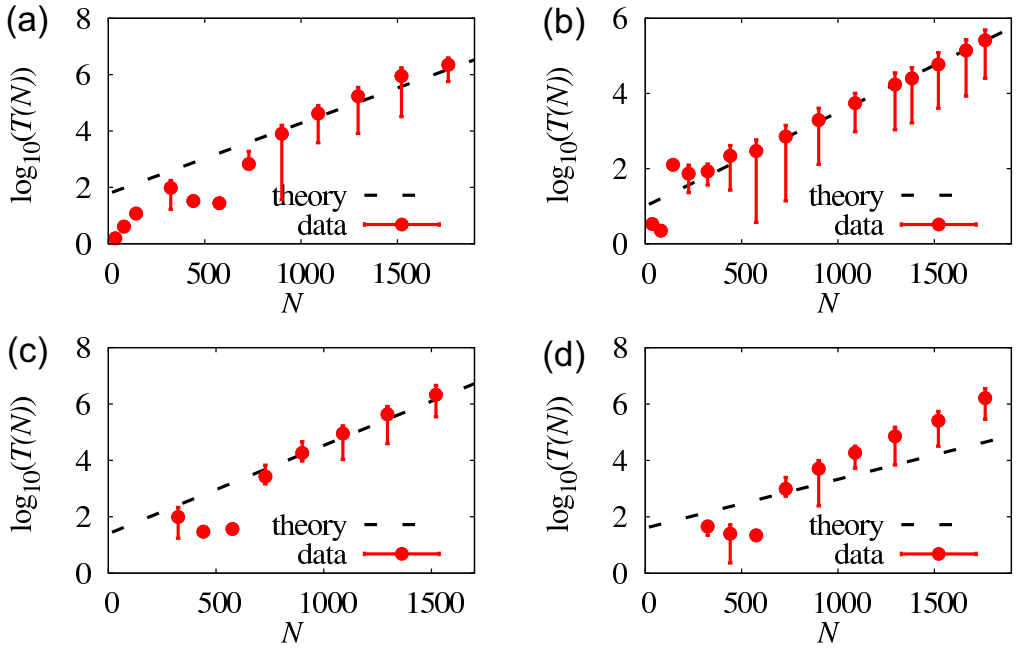

Figure 6.10: Lifetime $T(N)$ (log scale) vs N. The symbol and the error bar correspond to the average and the standard deviation of $T(N)$ for each system size, respectively. (a) Bär model with periodic boundary condition, $b = 0.070$, $\varepsilon = 0.080$. (b) Bär model with Neumann boundary condition, $b = 0.070$, $\varepsilon = 0.080$. (c) Bär model with periodic boundary condition, $b = 0.030$, $\varepsilon = 0.075$. (d) Bär model with periodic boundary condition, $b = 0.070$, $\varepsilon = 0.090$. Note that in the Bär model with periodic boundary condition (a,c), the system size dependence of lifetime is obviously not exponential for small system sizes ($N \leq 24^2$). For such small systems, we find that transient chaotic states occasionally end up with various complex patterns including temporally periodic states with $m \neq 0$.

Starting from some initial number m^* of defects, we have a series of defect numbers at each time point, e.g., $\{m^*, m^* + 2, \cdots, 4, 4, 4, 6, 6, 4, 2, 2, 0, 0, 2, 2, 2, \mathrm{S}\}$, where the symbol "S" denotes the event at which 0 continues for 100 units of time (which we regard as the steady state). The lifetime in each trial is the length of this series. The expected value of lifetime T is the inverse of the probability λ to obtain S. Because S is obtained only when the previous number is 2, $\lambda = Zp(2)$ where $p(2)$ is the probability to obtain 2, and Z is the transition rate from the state with $m = 2$ to the steady state. Therefore, the expected lifetime for a given system size N is

$$T(N) = \frac{1}{Zp(2)}. \tag{6.17}$$

For large N, the probability distribution of the number of defects is well approximated by Eq. (6.14), and mean number $\mu(= \alpha N)$ of defects is large. For $m \ll \mu$,

approximately

$$p(m) \sim \exp\left(-\frac{\alpha^2}{2\beta}N\right) \tag{6.18}$$

Plugging this into $p(2)$ in Eq. (6.17) and next assuming that Z is independent of N, we finally obtain

$$T(N) \sim \exp\left(\frac{\alpha^2}{2\beta}N\right). \tag{6.19}$$

This expression indicates that the lifetime depends exponentially on system size N, and its exponent is associated with density α and magnitude β of the fluctuation of the number of defects. For the Neumann boundary condition, the steady state can be reached not only from the states with $m = 2$ via annihilation but also from the states with $m = 1$ through absorption of a defect by the boundary. Therefore, probability λ to obtain S is $\lambda = Z_1 p(1) + Z_2 p(2)$ with transition rates Z_1 and Z_2. In this case as well, we obtain Eq. (6.19) because both $p(1)$ and $p(2)$ can be well approximated by Eq. (6.18) for large N.

Our expression in Eq. (6.19) is numerically verified (Fig. 6.10). The slope given by Eq. (6.19) (the dashed lines) is in good agreement with that obtained numerically in both the Bär model (Fig. 6.10 (a–d)) and the CGLE (Fig. 7.3(a,b)) for large system sizes. Nonetheless, we find a discrepancy for some parameter sets. In the Bär model, there are considerable deviations for large ε values (e.g., Fig. 6.10(d)). In the CGLE, we also find such cases for some parameter sets, e.g., $c_1 = 0.50$, $c_2 = -1.50$ with periodic boundary condition (result not shown). Overall, we find that the parameter sets for which our theory is valid are typically in the region near the onset of transient chaos [45, 47]. A possible reason why our theory fails when the system is far from the onset of spiral chaos will be discussed in Section 7.4.

6.5 The dependence of lifetime on system shape

In the previous section, we have examined the lifetime for a square system and clarified that lifetime increases exponentially. This system size dependence of lifetime is also observed in a system with different characteristics [12]. In order to examine how the spiral behavior changes when the aspect ratio of the system is different, a detailed numerical calculation was carried out. We set the aspect ratio to $= 1\colon 1,\ 1\colon 2,\ 1\colon 3,\ 1\colon 4$, and the lifetime was calculated by changing the system size while keeping the ratio fixed. Numerical setting is $b = 0.07,\ \varepsilon = 0.08$ for the Bär model. The boundary condition is set to the Neumann boundary.

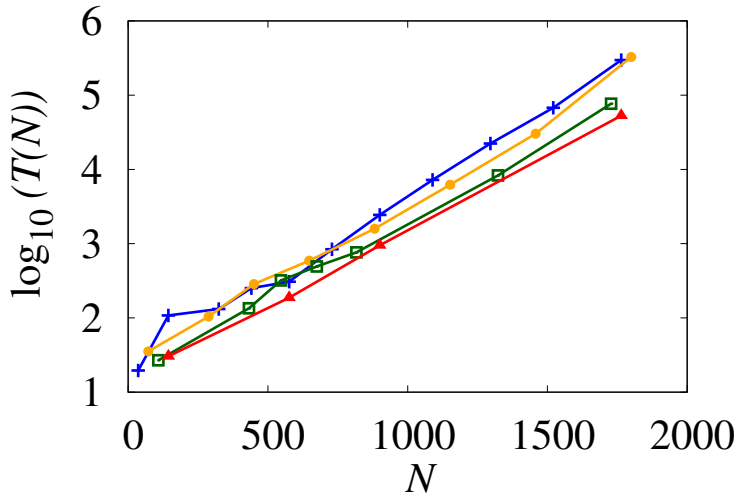

Figure 6.11: The system size and shape dependence of lifetime. The blue, yellow, green and red lines are the lifetime values of a system with 1 by 1, 1 by 2, 1 by 3 and 1 by 4, respectively. Over $N = 1000$, the lifetime of each system shape takes the same value.

The result is given as follows (Fig. 6.11). We found that lifetime increases exponentially at a large system size and the duration of lifetimes is different for each system shape.

In the area where system size is small ($N < 1000$), there is a peak at a certain system size. In such a region, the spirals are pinned and defects keep to rotate in the same place. Therefore, defects cannot meander and it takes a long time for the system to fall into the steady state. Although the system size dependence of lifetime can be seen even in the area of a small system size, the slope of lifetime varies depending on the shape of the system. Here, we investigate in detail a system with a small size. In Fig. 6.12(a), the generated spiral rotates in the system making the waves parallel to the short side of the system and flows in the direction of the shorter side. As we gradually change the aspect ratio of the system to approach a square in Fig. 6.12(b), the flow takes place in the direction of the long side of the system though the generated spirals still tend to flow in the direction of the short side of the system. When the shape of the system is square, the direction of the wave flow is isotropic. In this numerical simulation, we can see that spirals flow toward the short side of the system when the shape of the system is a rectangle, and its waves flowing in a certain direction prevent collision of spirals. Thus, the occurrence of defects decreases, which makes the lifetime short. On the other hand, as the system shape becomes isotropic, the direction of movement of the spiral also becomes isotropic, and spirals move back and forth to collide with each other making the system more chaotic. Therefore,

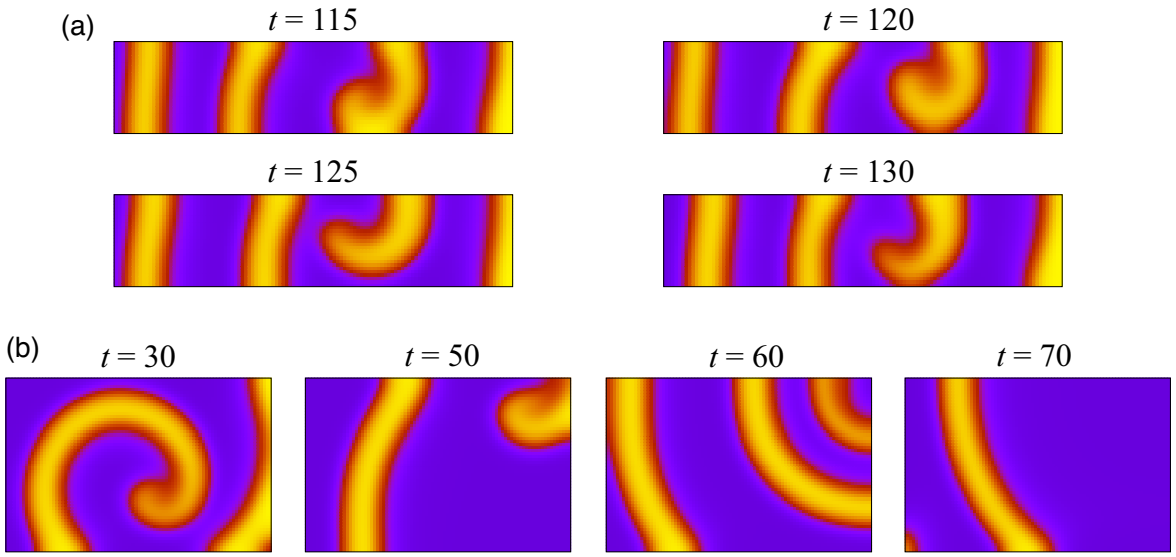

Figure 6.12: The time series of the state of spiral chaos. (a)System size $N = 120 \times 30$. Waves flow in the direction of the short side of the system. (b) $N = 90 \times 60$. Waves flow diagonally.

the number of defects increases, and lifetime becomes longer.

At the region that near $N = 1000$ where the slopes of the lifetime of each system shape take the same value, and the distributions of the numbers of defects approach the Gaussian distribution. Accordingly, systems have the same distribution of formation of the number of defects whose slopes of the average and variance of the number of defects are the same at a large system size. Therefore, comparing the lifetime of a square and rectangular system, the rectangular system has shorter lifetime than that of the square system if the system size is fixed. In addition, it can be seen that lifetime increases exponentially with system size in any aspect ratio when the system is sufficiently large. The slope of the lifetime takes the same value even when the aspect ratio is different.

Chapter 7

Statistical properties of spiral chaos in oscillating media

To check the generality of the argument presented in the previous chapter, we analyze the system behavior of the CGLE in the same way as that of the Bär model. We found that our claim holds true in both models.

7.1 Model and numerical settings

In previous chapters, we dealt with statistical properties of spiral chaos in excitable media. To check the generality of our argument, we also numerically evaluated the oscillatory media described by the CGLE.

The excitable medium shows excitement when it receives an input exceeding a certain threshold and after that, it returns to the steady state. On the other hand, the oscillating medium is known as a system that does not fall into a steady state even after excitation and repeats oscillation spontaneously with periodic rhythm [68].

We use the CGLE for the numerical calculation [32, 47].

$$\frac{\partial W}{\partial t} = W + (1 + \mathrm{i}b)\nabla^2 W - (1 + \mathrm{i}c)|W|^2 W. \tag{7.1}$$

where W is the variable corresponding to u and v of the Bär model. Depending on the parameters b and c, the state of the system changes, then a plane wave or a turbulent state with an amplitude $|W|$ appears. In such a system, we can also generate the state of spiral chaos similar to that in the Bär model. Here, the solution of the CGLE is an oscillating one (Fig. 7.1). Therefore, when the spirals disappear after a long transient time, the concentration of elements of the system oscillate all at once (Fig. 5.1).

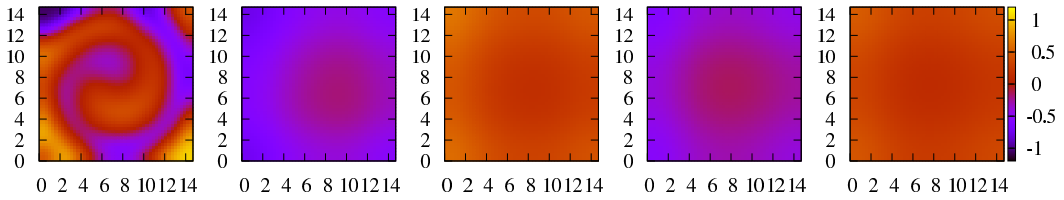

Figure 7.1: A time series of CGLE at $t = 40,\ 120,\ 130,\ 140,\ 150$ with the parameter $b = -0.5,\ c = 2.2$. The boundary condition is periodic. System size is 15×15. The system oscillates.

This oscillating solution is given by

$$W = \exp(-\mathrm{i}ct). \tag{7.2}$$

7.2 Time evolution and probability distribution of the number of defects

7.2.1 Defect counting

As in the Bär model, we calculate the topological charge using the equation

$$C(\boldsymbol{r},\ t) = \frac{1}{2\pi} \oint \nabla\phi(\boldsymbol{r}, t) \cdot d\boldsymbol{l} \tag{7.3}$$

where ($\phi = \arg W$) and detects defects in the system.

The numerical setting is as follows. We use the fourth–order Runge–Kutta method and a central differences method for calculating a Laplacian. The space step is $h = 0.3$, and the time step is $s = 0.01$. Both periodic and Neumann boundary conditions are performed. For the initial conditions, two monotonically increasing gradient planes are made to cross at a right angle. Defects are generated near $W = 0$.

7.2.2 The distribution of the number of defects

Similarly to the Bär model, the distribution of the number of defects at each system size is calculated. Both periodic and the Neumann boundary conditions are used, and the parameter set is $b = -0.5,\ c = 1.5$. The results are as follows (Fig. 7.2). We can found that the distribution approaches the Gaussian distribution when the system size is large. Therefore, we can expect that it also obeys the central limit theorem for the CGLE.

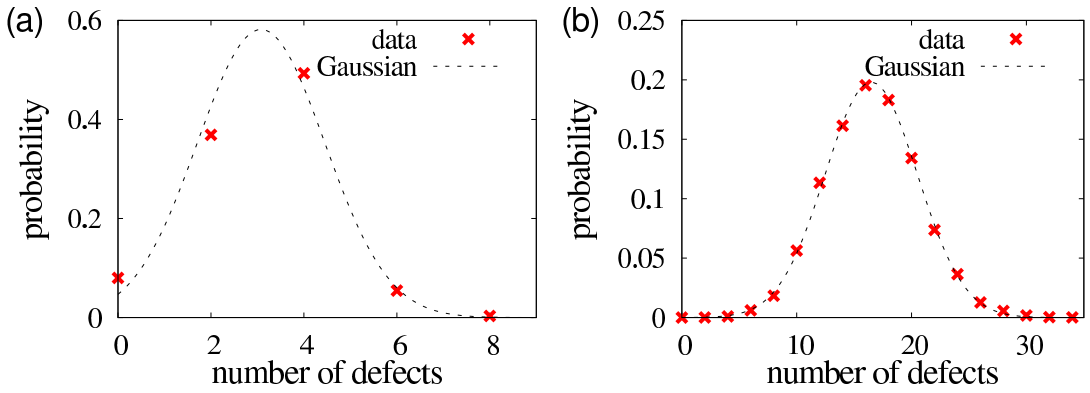

Figure 7.2: The distribution of the number of defects. The parameter set is $b = -0.5,\ c = 1.5$. Periodic boundary condition. (a) System size $N = 24 \times 24$. (b) $N = 60 \times 60$. The red symbols are simulation data. The dashed lines are the Gaussian distributions with average $\mu = \alpha N$ and variance $\sigma^2 = \beta N$ with $\alpha = 3.07844$ (16.4916), $\beta = 1.88106$ (16.2414).

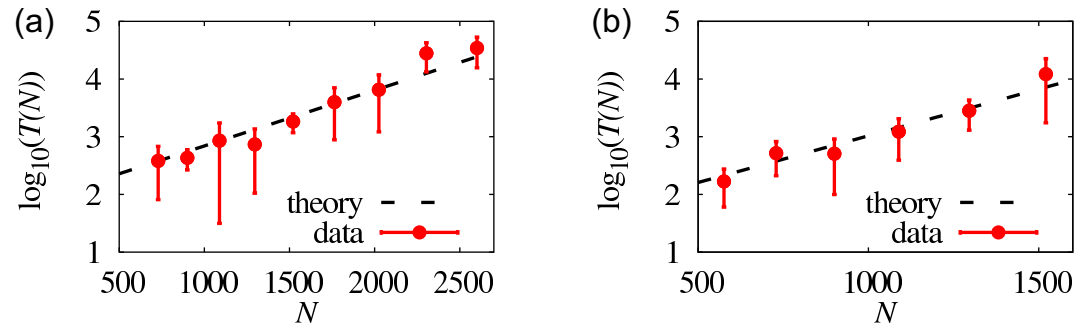

Figure 7.3: Lifetime $T(N)$ (log scale) vs N. The symbol and the error bar correspond to the average and the standard deviation of $T(N)$ for each system size, respectively. (a) CGLE with periodic boundary condition, $c_1 = 0.80,\ c_2 = -1.00$. (b) CGLE with periodic boundary condition, $c_1 = 0.50,\ c_2 = -1.11$.

7.3 System size dependence of lifetime

Now we elucidated that the distribution of the number of defects approaches the Gaussian distribution for the large system of CGLE because the system obeys central limit theory. The average and variance of the number of defects increases monotonically as the system size increases. Consequently, we calculate the lifetime using Eq. (6.19) with α and β that we obtained above. In this case, the lifetime also increases exponentially with system size. Therefore, our argument is general, and this system size dependence of lifetime does not depend on models.

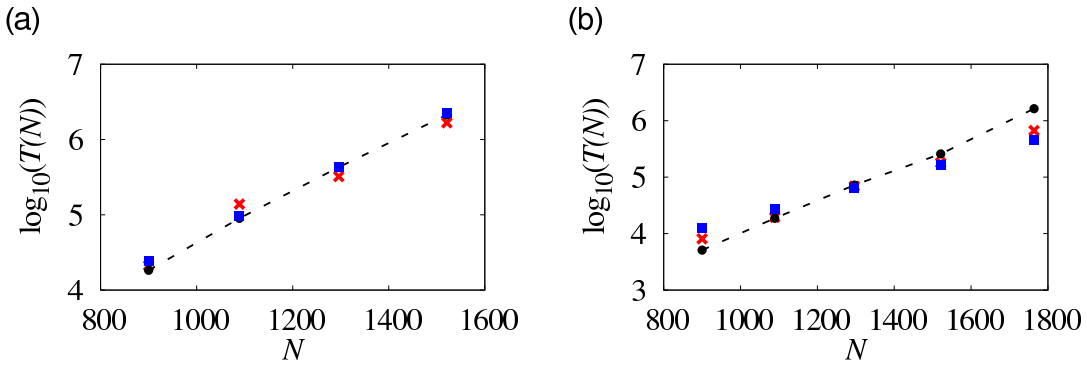

Figure 7.4: System size dependence of numerically obtained T (symbol $\bullet$ with a dashed line), $C_1/p(2)$ with numerically obtained $p(2)$ (symbol $\times$) and $C_2/p(2)$ with $p(2)$ given by Eq. (6.18) (symbol $\square$), where C_1 and C_2 are fitting parameters. Parameter values for (a) and (b) are the same as those for Fig. 6.10(c) and Fig. 6.10(d), respectively.

7.4 Conclusions and discussion for phase ordering

In this thesis, we investigated the system size dependence of the lifetime of spiral chaos. We derived an expression for the lifetime, given as Eq. (6.19) [53], taking advantage of the fact that the probability distribution of the number of defects is Gaussian for large system sizes. We confirmed that Eq. (6.19) well fits numerically obtained $T(N)$ for two different models, the Bär model and the CGLE, with several parameter sets and different boundary conditions.

We emphasize that Eq. (6.19) is useful for the prediction of the lifetime of large systems. We can precisely estimate α and β values by examination of the number of defects in a large system. The observation of a relatively small system for different initial conditions enables us to find the average lifetime $T(N)$. Then, using $T(N) \sim \exp\left(\frac{\alpha^2}{2\beta}N\right)$, we can estimate the average lifetime for large system sizes.

We have also found that Eq. (6.19) fails to predict the system size dependence for the parameter sets far from the onset of chaos. Our theory is based on Eqs. (6.17) and (6.18). We can verify these equations by comparing the system size dependences of T and $1/p(2)$ obtained numerically and these predicted by Eqs. (6.17) and (6.18). As shown in Fig. 7.4, whereas both Eq. (6.17) and Eq. (6.18) are valid near the onset, and the discrepancy between numerically obtained T and $1/p(2)$ is particularly large far from the onset.

Thus, the assumption in Eq. (6.17) seems to be violated. Namely, transition rate Z from the state with $m = 2$ to the steady state seems to depend strongly

on the system size in such a parameter region. The following observation may provide a reasoning for it. Even when defects completely vanish, some wave pattern may persist for a while. Defect reemergence is attributed to such a remaining pattern. The complexity of wave patterns in the absence of defects might be enhanced as the system size increases, making it more difficult for the system to settle down into the steady state. Indeed, for all parameter sets for which our theory fails, the actual lifetime has a stronger dependence on the system size than that expected from our theory given by Eq. (6.19) at constant Z. We also observed that meandering of defects and fluctuation of the the number of defects seem to be stronger. A previous numerical study of the Bär model also indicates that the system becomes more strongly chaotic for such parameter sets [67]. Therefore, it is indeed likely that our system cannot be fully characterized only by the number of spirals when the system is far from the onset of transient chaos.

Chapter 8

Summary

In this thesis, we theoretically investigated the dynamics of ordering phenomena of polarity and phase.

First, to analyze the dynamics of polarity ordering, we derived a phase model. This simple model includes the cell geometric information, and global orientation of polarity depends on the heterogeneity of coupling strengths and the shape of cells. The phenomenon in which the orientation of cell polarity changes due to a change in cell shape has also been observed in the experiments on *Drosophila* wings and mouse embryos, and previous theoretical models have been proposed to describe their dynamics. Some of these theoretical models are artificial in that an energy function drives the orientation of polarity in the direction of cell elongation. Other models are too complicated. In our study, however, we reduced the phenomenological model by means of the phase reduction theory, and derived a very simple model of ODE naturally. In addition, although our model is a simple and tractable one, it is possible to reproduce the results similar to the numerical simulations conducted by Amonlirdviman et al. [5], and to take into account various conditions easily. This is our model's merit. In particular, we show that the axial asymmetry of the system facilitates the formation of globally oriented polarity patterns. Previous experimental results suggest that axial asymmetry of the system may play an important role in the ordering of cell polarity; however, its mechanism is not well understood. In our model, when the coupling strength is isotropic, the polarity is aligned toward a wide adhesion surface of the cell, and when the coupling strength differs depending on the adhesion surface, the cell polarity is oriented toward the region where the coupling strength is high. Therefore, our model provides an understanding of how the axial asymmetry in the system contributes to the formation of globally aligned patterns of cell polarity.

Second, to analyze the dynamics of phase ordering, transient spiral chaos was

studied because the behavior of electric waves in the heart causing arrhythmia is similar to spiral chaos. In the arrhythmia, electrical waves fall into a chaotic state, and it is known that this chaotic state cannot persist when the heart is subdivided by a catheter.

Even in the mathematical model, by setting the parameters of the model to be transient, it is clarified numerically that lifetime, the time it takes for the system to reach a steady state after a long chaotic state, depends on the system size. In order to derive a theoretical prediction of this lifetime, we analyzed the number of defects corresponding to the number of waves. When the system is chaotic, it was found that the defect distribution approaches the Gaussian distribution as the system size increases because of the central limit theorem. Via this distribution of the number of defects, an equation for predicting lifetime was derived. The parameters in this equation are the average and variance of the number of defects in a small region of the system, which can be easily determined numerically. It is also confirmed that the system size dependence of lifetime holds true even if the system geometry is not square. Similarly, lifetime grows exponentially with system size in the case of a rectangular shape instead of a square, but the slopes differ slightly for a small system size. This is because if the system size is small, the generated wave moves isotropically in a square system, but in a rectangular system, waves tend to propagate in the direction along the long axis. As the system size increases, spiral waves propagate almost isotropically even in a square system; thus, the dependence of lifetime on the system size is not affected by the system geometry. This lifetime equation consists at the onset of the transient spiral chaos, and we emphasize that this equation is useful for prediction of the lifetime of large systems. Although this theoretical expression seems valid only at the onset of the transient spiral chaos, we emphasize that this expression is useful for the rough estimation of the lifetime of large systems.

Acknowledgements

First of all, I would like to express gratefully gratitude to Associate Professor Dr. Hiroshi Kori for his fully support. He guided, provided me with great opportunities to study the nonlinear dynamics and encouraged my research all the time since the laboratory has started.

I am also really grateful to Associate Professor Dr. Hiroya Nakao and Senior Scientist Dr. Yoji Kawamura for advising me on mathematical methods. Special thanks go out to Associate Professor Dr. Shuji Ishihara and Assistant Professor Dr. Kaoru Sugimura for providing valuable information on the experiments. I thank Professor Dr. Hiroaki Yoshida, Professor Dr. Hideyuki Majima, Professor Dr. Tetsuya Kawamura, and Associate Professor Dr. Kazue Kudo for the valuable discussions and honest support. Besides, many thanks go to Assistant Professor Dr. Yasuaki Kobayashi, Postdoctoral Fellow Dr. Kyohei Shitara, and Assistant Professor Dr. Yuki Izumida. Their advice and comments have been great help in my research.

I would like to thank Ochanomizu University for their financial support and group members for their kindness.

Finally, I am grateful to my parents for all the devoted quotidian support.

Appendix A

Linear stability method

For periodic boundary condition for Bär model, we use linear stability analysis. Now we determine the stable fixed points and the deviation as $(u^*,\ v^*)$, and $\delta u,\ \delta v$, respectively. And D is the diffusion coefficient. The variables $u,\ v$ are given by

$$u = u^* + \delta u \tag{A.1}$$

$$v = v^* + \delta v. \tag{A.2}$$

Substituting $u,\ v$ for the Bär model in Eq. (6.1), we get

$$\frac{\partial u}{\partial t} = \frac{\partial \delta u}{\partial t} = -\frac{b}{a\varepsilon}\delta u + D\nabla^2 \delta u \tag{A.3}$$

$$\frac{\partial v}{\partial t} = \frac{\partial \delta v}{\partial t} = -\delta v. \tag{A.4}$$

Here, Fourier-transformation is performed with space $x,\ y \in [-L,\ L]$. Thus

$$u_{p,q}(t) = \mathcal{F}[\delta u] = \int_{-L}^{L}\int_{-L}^{L} \delta u(x,\ y,\ t) e^{-i(px+qy)} dxdy \tag{A.5}$$

$$v_{p,q}(t) = \mathcal{F}[\delta v] = \int_{-L}^{L}\int_{-L}^{L} \delta v(x,\ y,\ t) e^{-i(px+qy)} dxdy. \tag{A.6}$$

where p and q are the wavenumber of the direction of x and y axis, respectively.

$$p = \frac{2\pi n_x}{L} \quad (n_x \in \mathbb{N}) \tag{A.7}$$

$$q = \frac{2\pi n_y}{L} \quad (n_y \in \mathbb{N}) \tag{A.8}$$

By the properties of the Fourier transform,

$$\mathcal{F}\Big[\frac{\partial \delta u}{\partial \boldsymbol{r}}\Big] = -i(p+q)u_{p,q} \tag{A.9}$$

$$\mathcal{F}\Big[\frac{\partial^2 \delta u}{\partial \boldsymbol{r}^2}\Big] = -(p+q)^2 u_{p,q} \tag{A.10}$$

which is derived from the periodic condition

$$\delta u(-L,\ y,\ t) = \delta u(L,\ y,\ t) \tag{A.11}$$

$$\delta u(-x,\ -L,\ t) = \delta u(x,\ L,\ t) \tag{A.12}$$

$$\left.\frac{\partial \delta u}{\partial t}\right|_{x=-L} = \left.\frac{\partial \delta u}{\partial t}\right|_{x=L} \tag{A.13}$$

$$\left.\frac{\partial \delta u}{\partial t}\right|_{y=-L} = \left.\frac{\partial \delta u}{\partial t}\right|_{y=L}. \tag{A.14}$$

Please note that this properties can hold other boundary conditions. The same is true of variable v. We apply the above results to Eqs. (A.3) and (A.4), and get

$$\frac{\partial u_{p,q}}{\partial t} = \Big(-\frac{b}{a\varepsilon} - D(p+q)^2\Big)u_{p,q}, \tag{A.15}$$

$$\frac{\partial v_{p,q}}{\partial t} = -v_{p,q}. \tag{A.16}$$

Therefore, the matrix is given by

$$\begin{pmatrix} \dfrac{\partial u_{p,q}}{\partial t} \\ \\ \dfrac{\partial v_{p,q}}{\partial t} \end{pmatrix} = \begin{pmatrix} -\dfrac{b}{a\varepsilon} - D(p+q)^2 & 0 \\ \\ 0 & -1 \end{pmatrix} \begin{pmatrix} u_{p,q} \\ \\ v_{p,q} \end{pmatrix}. \tag{A.17}$$

These eigenvalues are

$$\lambda_1 = -\frac{b}{a\varepsilon} - D(p+q)^2,\ \lambda_2 = -1. \tag{A.18}$$

Hence the stability of the solution depends on the sign of λ_1. Here, it is always $\lambda_1 < 0$ in the parameter region $a,\ b,\ \varepsilon > 0$ where we consider. From this, we can find that the steady state is linear stable.

Bibliography

[1] A. T. Winfree. *The geometry of biological time*. Biomathematics. Springer Verlag, New York, 1980.

[2] M. Cross and P. Hohenberg. Pattern formation outside of equilibrium. *Rev. Mod. Phys.*, Vol. 65, pp. 851–1112, Jul 1993.

[3] H. Meinhardt and A. Gierer. Pattern formation by local self-activation and lateral inhibition. *Bioessays*, Vol. 22, No. 8, pp. 753–760, 2000.

[4] H. Nakao and A. S. Mikhailov. Turing patterns in network-organized activator-inhibitor systems. *Nature Physics*, Vol. 6, No. 7, pp. 544–550, 2010.

[5] K. Amonlirdviman, N. A. Khare, D. RP Tree, W.-S. Chen, J. D. Axelrod, and C. J. Tomlin. Mathematical modeling of planar cell polarity to understand domineering nonautonomy. *Science*, Vol. 307, No. 5708, pp. 423–426, 2005.

[6] B. Aigouy, R. Farhadifar, D. B. Staple, A. Sagner, J.-C. Röper, F. Jülicher, and S. Eaton. Cell flow reorients the axis of planar polarity in the wing epithelium of drosophila. *Cell*, Vol. 142, No. 5, pp. 773–786, 2010.

[7] Y. Kuramoto. *Chemical Oscillations, Waves, and Turbulence*. Springer, New York, 1984.

[8] C. Beta, A. S. Mikhailov, H. H. Rotermund, and G. Ertl. Defect-mediated turbulence in a catalytic surface reaction. *EPL (Europhysics Letters)*, Vol. 75, No. 6, p. 868, 2006.

[9] D. Devenport. The cell biology of planar cell polarity. *The Journal of cell biology*, Vol. 207, No. 2, pp. 171–179, 2014.

[10] Y. Burak and B. I. Shraiman. Order and stochastic dynamics in drosophila planar cell polarity. *PLoS Comput Biol*, Vol. 5, No. 12, p. e1000628, 2009.

[11] B. Guirao, A. Meunier, S. Mortaud, A. Aguilar, J.-M. Corsi, L. Strehl, Y. Hirota, A. Desoeuvre, C. Boutin, Y.-G. Han, et al. Coupling between hydrodynamic forces and planar cell polarity orients mammalian motile cilia. *Nature cell biology*, Vol. 12, No. 4, p. 341, 2010.

[12] Z. Qu. Critical mass hypothesis revisited: role of dynamical wave stability in spontaneous termination of cardiac fibrillation. *American Journal of Physiology-Heart and Circulatory Physiology*, Vol. 290, No. 1, pp. H255–H263, 2006.

[13] M. T. Butler and J. B. Wallingford. Planar cell polarity in development and disease. *Nature reviews molecular cell biology*, Vol. 18, No. 6, p. 375, 2017.

[14] T. Ayukawa, M. Akiyama, J. L. Mummery-Widmer, T. Stoeger, J. Sasaki, J. A. Knoblich, H. Senoo, T. Sasaki, and M. Yamazaki. Dachsous-dependent asymmetric localization of spiny-legs determines planar cell polarity orientation in drosophila. *Cell reports*, Vol. 8, No. 2, pp. 610–621, 2014.

[15] W. Y. Aw and D. Devenport. Planar cell polarity: global inputs establishing cellular asymmetry. *Current opinion in cell biology*, Vol. 44, pp. 110–116, 2017.

[16] J. M. Kosterlitz and D. J. Thouless. Ordering, metastability and phase transitions in two-dimensional systems. *Journal of Physics C: Solid State Physics*, Vol. 6, No. 7, p. 1181, 1973.

[17] J. M. Kosterlitz. The critical properties of the two-dimensional xy model. *Journal of Physics C: Solid State Physics*, Vol. 7, No. 6, p. 1046, 1974.

[18] A. T. Winfree. Biological rhythms and the behavior of populations of coupled oscillators. *Journal of Theoretical Biology*, Vol. 16, pp. 15–42, 1967.

[19] A. Pikovsky, M. Rosenblum, and J. Kurths. *Synchronization: A Universal Concept in Nonlinear Sciences*. Cambridge Univ. Press, 2001.

[20] A. M. Turing. The chemical basis of morphogenesis. *Bulletin of mathematical biology*, Vol. 52, No. 1-2, pp. 153–197, 1990.

[21] A. J. Koch and H. Meinhardt. Biological pattern formation: from basic mechanisms to complex structures. *Reviews of Modern Physics*, Vol. 66, No. 4, p. 1481, 1994.

[22] J. Schnakenberg. Simple chemical reaction systems with limit cycle behaviour. *Journal of theoretical biology*, Vol. 81, No. 3, pp. 389–400, 1979.

[23] Y. Kawamura and H. Nakao. Phase description of oscillatory convection with a spatially translational mode. *Physica D: Nonlinear Phenomena*, Vol. 295, pp. 11–29, 2015.

[24] J. Davidsen, A. S. Mikhailov, and R. Kapral. Front explosion in a periodically forced surface reaction. *Physical Review E*, Vol. 72, No. 4, p. 046214, 2005.

[25] T. Usui, Y. Shima, Y. Shimada, S. Hirano, R. W. Burgess, T. L. Schwarz, M. Takeichi, and T. Uemura. Flamingo, a seven-pass transmembrane cadherin, regulates planar cell polarity under the control of frizzled. *Cell*, Vol. 98, No. 5, pp. 585–595, 1999.

[26] S.M.T.W. Maung and A. Jenny. Planar cell polarity in drosophila. *Organogenesis*, Vol. 7, No. 3, pp. 165–179, 2011.

[27] W. Y. Aw, B. W. Heck, B. Joyce, and D. Devenport. Transient tissue-scale deformation coordinates alignment of planar cell polarity junctions in the mammalian skin. *Current Biology*, Vol. 26, No. 16, pp. 2090–2100, 2016.

[28] H. Matakatsu and S. S. Blair. Interactions between fat and dachsous and the regulation of planar cell polarity in the drosophila wing. *Development*, Vol. 131, No. 15, pp. 3785–3794, 2004.

[29] A. T. Winfree. *The Geometry of Biological Time*. Springer, New York, 2nd edition, 2001.

[30] K. Sugimura and H. Kori. A reduced cell-based phase model for tissue polarity alignment through global anisotropic cues. *Scientific reports*, Vol. 7, No. 1, p. 17466, 2017.

[31] Y. Shimada, S. Yonemura, H. Ohkura, D. Strutt, and T. Uemura. Polarized transport of frizzled along the planar microtubule arrays in drosophila wing epithelium. *Developmental cell*, Vol. 10, No. 2, pp. 209–222, 2006.

[32] I. S. Aranson and L. Kramer. The world of the complex ginzburg-landau equation. *Rev. Mod. Phys.*, Vol. 74, No. 1, p. 99, 2002.

[33] H. Nakao, T. Yanagita, and Y. Kawamura. Phase-reduction approach to synchronization of spatiotemporal rhythms in reaction-diffusion systems. *Physical Review X*, Vol. 4, No. 2, p. 021032, 2014.

[34] F. C. Hoppensteadt and E. M. Izhikevich. *Weakly connected neural networks*, Vol. 126. Springer Science & Business Media, 2012.

[35] L. S. Tuckerman and D. Barkley. Bifurcation analysis of the eckhaus instability. *Physica D: Nonlinear Phenomena*, Vol. 46, No. 1, pp. 57–86, 1990.

[36] S. Cortès, N. Glade, I. Chartier, and J. Tabony. Microtubule self-organisation by reaction–diffusion processes in miniature cell-sized containers and phospholipid vesicles. *Biophysical chemistry*, Vol. 120, No. 3, pp. 168–177, 2006.

[37] R. R. Daga and P. Nurse. Interphase microtubule bundles use global cell shape to guide spindle alignment in fission yeast. *Journal of cell science*, Vol. 121, No. 12, pp. 1973–1980, 2008.

[38] S. B. Haase and D. J. Lew. Microtubule organization: cell shape is destiny. *Current Biology*, Vol. 17, No. 7, pp. R249–R251, 2007.

[39] B. Strauss, R. J. Adams, and N. Papalopulu. A default mechanism of spindle orientation based on cell shape is sufficient to generate cell fate diversity in polarised xenopus blastomeres. *Development*, Vol. 133, No. 19, pp. 3883–3893, 2006.

[40] D. Ma, K. Amonlirdviman, R. L. Raffard, A. Abate, C. J. Tomlin, and J. D. Axelrod. Cell packing influences planar cell polarity signaling. *Proceedings of the National Academy of Sciences*, Vol. 105, No. 48, pp. 18800–18805, 2008.

[41] A. S. Mikhailov and R. Kapral. Hydrodynamic collective effects of active protein machines in solution and lipid bilayers. *Proceedings of the National Academy of Sciences*, Vol. 112, No. 28, pp. E3639–E3644, 2015.

[42] Y. Saito. A demonstration with magnetic compasses and the spontaneous breakdown of symmetry:in japanese(「方位磁石集団による磁区演示と「自発的対称性の破れ」」). *Physics Education*, Vol. 53, No. 2.

[43] T. Nishimatsu, U. V. Waghmare, Y. Kawazoe, B. Burton, K. Nagao, and Y. Saito. A numerical simulation of a classical dipolar spin system and a demonstration with magnetic compasses. *Osaka Science Museum Reports*, Vol. 17, No. 1.

[44] J. P. James Keener and J. Sneyd. *Mathematical Physiology I:Cellular Physiology*. Springer, 2nd edition, 2009.

[45] M. Bär and M. Eiswirth. Turbulence due to spiral breakup in a continuous excitable medium. *Phys. Rev. E*, Vol. 48, pp. R1635–R1637, Sep 1993.

[46] D. Krefting and C. Beta. Theoretical analysis of defect-mediated turbulence in a catalytic surface reaction. *Physical Review E*, Vol. 81, No. 3, p. 036209, 2010.

[47] H. Chaté and P. Manneville. Phase diagram of the two-dimensional complex ginzburg-landau equation. *Physica A: Statistical Mechanics and its Applications*, Vol. 224, No. 12, pp. 348 – 368, 1996. Dynamics of Complex Systems.

[48] I. Berenstein and C. Beta. Flow-induced control of chemical turbulence. *The Journal of chemical physics*, Vol. 135, No. 16, p. 164901, 2011.

[49] R. Wackerbauer and K. Showalter. Collapse of spatiotemporal chaos. *Physical review letters*, Vol. 91, No. 17, p. 174103, 2003.

[50] T. Tél and Y.-C. Lai. Chaotic transients in spatially extended systems. *Physics Reports*, Vol. 460, No. 6, pp. 245–275, 2008.

[51] A. Wacker, S. Bose, and E. Schöll. Transient spatio-temporal chaos in a reaction-diffusion model. *EPL*, Vol. 31, No. 5-6, p. 257, 1995.

[52] J. P. Crutchfield and K. Kaneko. Are attractors relevant to turbulence? *Phys. Rev. Lett.*, Vol. 60, No. 26, pp. 2715–2718, 1988.

[53] K. Sugimura and H. Kori. Exponential system-size dependence of the lifetime of transient spiral chaos in excitable and oscillatory media. *Physical Review E*, Vol. 92, No. 6, p. 062915, 2015.

[54] L. Gil, J. Lega, and J. Meunier. Statistical properties of defect-mediated turbulence. *Phys. Rev. A*, Vol. 41, pp. 1138–1141, Jan 1990.

[55] H. Ebata and M. Sano. Self-replicating holes in a vertically vibrated dense suspension. *Phys. Rev. Lett.*, Vol. 107, p. 088301, Aug 2011.

[56] C. Qiao, H. Wang, and Q. Ouyang. Defect-mediated turbulence in the belousov-zhabotinsky reaction. *Phys. Rev. E*, Vol. 79, p. 016212, Jan 2009.

[57] J. Davidsen and R. Kapral. Defect-mediated turbulence in systems with local deterministic chaos. *Phys. Rev. Lett.*, Vol. 91, p. 058303, Jul 2003.

[58] M. Falcke, M. Bär, J. D. Lechleiter, and J. L. Hudson. Spiral breakup and defect dynamics in a model for intracellular ca 2+ dynamics. *Physica D: Nonlinear Phenomena*, Vol. 129, No. 3, pp. 236–252, 1999.

[59] J. Kalifa, K. Tanaka, A. V. Zaitsev, M. Warren, R. Vaidyanathan, D. Auerbach, S. Pandit, K. L. Vikstrom, R. Ploutz-Snyder, A. Talkachou, et al. Mechanisms of wave fractionation at boundaries of high-frequency excitation in the posterior left atrium of the isolated sheep heart during atrial fibrillation. *Circulation*, Vol. 113, No. 5, pp. 626–633, 2006.

[60] T. Yamashita. Electrophysiology of Cardiac Myocytes:From ion channels to electrocardiography and arrhythmias: in Japanese(「心筋細胞の電気生理学–イオンチャネルから、心電図、不整脈へ–」). Medical Sciences International, 2011.

[61] P.-S. Chen, T.-J. Wu, C.-T. Ting, H. S. Karagueuzian, A. Garfinkel, S.-F. Lin, and J. N. Weiss. A tale of two fibrillations. *Circulation*, Vol. 108, No. 19, pp. 2298–2303, 2003.

[62] T. Yamane. Catheter ablation of atrial fibrillation: in Japanese(「心房細動アブレーションを究める」). Medical View CO., 2009.

[63] M. Haissaguerre, P. Sanders, M. Hocini, Y. Takahashi, M. Rotter, F. Sacher, T. Rostock, L.-F. HSU, P. Bordachar, S. Reuter, et al. Catheter ablation of long-lasting persistent atrial fibrillation: critical structures for termination. *Journal of cardiovascular electrophysiology*, Vol. 16, No. 11, pp. 1125–1137, 2005.

[64] A. T. Winfree. Electrical turbulence in three-dimensional heart muscle. *Science*, Vol. 266, No. 5187, pp. 1003–1006, 1994.

[65] S. Toda, T. Ashihara, J. Watanabe, K. Shirato, T. Ikeda, and K. Nakazawa. Theoretical analysis of the critical mass hypothesis as the maintenance mechanism of ventricular fibrillation. *JPN. J. Electrocardiology*, Vol. 28, No. 4, pp. 263–272, 2008.

[66] H. Mori and Y. Kuramoto. Dissipative structure and Chaos: in Japanese(「散逸構造とカオス」). Iwanami Shoten, 1994.

[67] M. C. Strain and H. S. Greenside. Size-dependent transition to high-dimensional chaotic dynamics in a two-dimensional excitable medium. *Phys. Rev. Lett.*, Vol. 80, No. 11, p. 2306, 1998.

[68] Y. Kuramoto and S. Koga. Turbulized rotating chemical waves. *Progress of theoretical physics*, Vol. 66, No. 3, pp. 1081–1085, 1981.